APPLICATIONS OF OPTOGENETIC TANDEM-CELL UNITS FOR IN VITRO STUDY OF CARDIAC ELECTROPHYSIOLOGY

by

Geran Kostecki

A dissertation submitted to Johns Hopkins University in conformity with the requirements for the degree of Doctor of Philosophy

Baltimore, Maryland

July 2019

Abstract

Optogenetics and tandem-cell units are an important tool for studying cardiac electrophysiology, and this work explores a few of the exciting avenues of study they enable. In Chapters 2 and 3, myofibroblasts and fibroblasts are transduced with Channelrhodopsin-2 and co-cultured with cardiomyocytes to acutely demonstrate that both are electrically connected enough to cardiomyocytes to produce changes in cardiomyocyte electrophysiology, which has implications for treating conduction slowing after cardiac injury. In Chapter 4, a simple, scalable method to use tandem-cell units to point-pace cells in culture to mature them is developed, which has the potential to make them more useful for *in vitro* study, drug testing, and tissue engineering. Finally, in Chapter 5, an engineered tissue from decellularized extracellular matrix is developed that represents the next step for the applications in the previous chapters by providing important physiological cues, which should improve their relevance and accuracy.

Primary reader and advisor: Dr. Leslie Tung, PhD

Secondary reader: Dr. Gordon Tomaselli, MD

Thesis Committee

Dr. Leslie Tung, PhD
Professor of Biomedical Engineering
Johns Hopkins University

Dr. Gordon Tomaselli, MD
Executive Vice President and Chief Academic Officer, Montefiore Medicine
The Marilyn and Stanley M. Katz Dean
Professor of Cardiology
Albert Einstein College of Medicine

Dr. Daniel Reich, PhD
Professor of Physics and Astronomy
Johns Hopkins University

Dr. Emilia Entcheva, PhD
Professor of Biomedical Engineering
George Washington University

Acknowledgements

First, I'd like to thank my P.I., Dr. Leslie Tung, for sticking with me through this long and challenging journey. Coming from a programming background, I didn't realize that a PhD, particularly in such a cell-culture heavy lab would be such a humbling experience that would test my organization, attention to detail, and patience, none of which were particular strengths for me. Of course, based on the 27(!) drafts of our first paper, I'm sure this tested your patience too, but I appreciate the fact that you took the time to help me through the process, when at times it probably would have been easier to do yourself. This was true for every aspect of my PhD, and I'm a much better scientist and writer as a result. I'd also like to thank Dr. Tomaselli, who has always been incredibly supportive and positive, which was especially important during my early years here. It's also been great getting to work with Dr. Reich and Dr. Entcheva, and I want to thank both of them for all of their help. My work was supported by an AHA pre-doctoral fellowship, as well as NIH grant R01 HL127087, Maryland Stem Cell Research Fund grant 2013-MSCRF-II-0045, and NIH grant S10 RR025544.

I'd like to thank the long-time members of my lab, David Hunter, Adriana Blazeski, and Renjun Zhu, who have been on this journey with me since I started it (and I'm thankful have stuck around despite having graduated long before me). I couldn't have done this without their support. From working together to solve problems, to bouncing ideas off of each other, to encouraging each other, to getting into overly long, sometimes ridiculous discussions, I couldn't ask for better labmates and friends. That goes for Justin and Rob too.

I'd like to thank my non-lab friends also – Kyle Rupp, Tashrik Ahmed, Jaymin Patel, Sohail Zahid, Melanie Zile, and everyone else who made my time out here a great way to spend my 20's on a personal level. I'd also like to thank my parents, Stan and Jana, and my sister, Lauren, who have supported me and put up with me being away all these years, and hardly ever let on how much I know they missed me.

Finally, I'd like to thank my wife Anne. I literally couldn't have done this without her, because whenever I've needed to work late, she's taken care of things at home, which has meant a lot more since we had our daughter, Clara. But on another level, her industriousness, dedication, and love of her work have truly inspired me to cultivate those qualities in my own work. Of course, spending time with her has also been a great way to spend my 20s, and I look forward to many more happy years to come back in St. Louis, or wherever our lives take us.

Table of Contents

List of tables

List of figures

List of Abbreviations

ChR2	Channelrhodopsin-2
CM	Cardiomyocyte
CFB	Cardiac fibroblast
ECM	Extracellular matrix
MFB	Cardiac myofibroblast
TGF-β1	Transforming growth factor β1
α-SMA	Smooth muscle actin
RP	Resting potential
AP	Action potential
CV	Conduction velocity
APD	Action potential duration
EHT	Engineered heart tissue
hiPSC-CM	Human induced pluripotent stem cell-derived cardiomyocyte
NRVM	Neonatal rat ventricular myocyte
FBS	Fetal bovine serum
SHG	Second harmonic generation
EHS	Engineered heart slice
EtD	Ethidium homodimer-1
IBI	Inter-beat interval
COV	Coefficient of variance

Chapter 1: Introduction

Cardiac optogenetics and tandem-cell units

While the existence of proteins that could alter transmembrane ion flow in response to light has been known since at least bacteriorhodopsin was demonstrated to alter intracellular pH in response to light in 1973 [1], and the utility of such proteins in the spatio-temporal control of biological systems was well recognized, it was long assumed that such channels would be too slow, weak, or even toxic when exogenously expressed in mammalian systems (for review and discussion, see [2]). However, Channelrhodopsin-2 (ChR2), an opsin from the algae C. reinhardtii, was found to be functional in cells from a number of species, including human embryonic kidney cells, and have many properties ideal for light-based control of cells [3]. It is a light-gated cation channel, with insignificant proton pump activity [4], unlike like many other opsins, which means that using it to alter transmembrane voltage does not cause large corresponding changes in pH. Additionally, as an ion channel, it has a faster response time (τ=~1 ms [5]) and a larger single-channel flux than proton pumps. Finally, it has very little dark current, and only partially inactivates upon continued exposure to light with τ=~21 ms [5] (See [6] for further review of ChR2 biophysics). ChR2 was shown to be consistent and effective in generating spatiotemporally controlled neuron spiking in a seminal paper in 2005 [7]. Since then, many mutants have been developed to alter the kinetics, spectral sensitivity, and ion selectivity, including the H134R mutant used in this work, which was developed to yield reduced inactivation and a higher steady state current [5]. .

Application of ChR2 to cardiac cells began in 2010, when Breugmann, et al. transduced cardiac embryonic stem cells and used light flashes to point pace, as well as continuous application of light to increase spontaneous beating rate and intracellular calcium [8]. They also were able to generate a ChR2 mouse line and optically pace *in vivo* by opening the chest cavity to apply light. In 2011 Jia et al. developed a line of ChR2-transduced HEK cells, which they later called spark cells, and showed they could electrically couple with co-cultured cardiomyocytes (CMs) to form a tandem-cell unit, allowing for optical pacing without needing to transduce cardiac cells [9]. Nussinovitch, et. al. expanded on this work by transducing 3T3 fibroblasts with ChR2 and Archaerhodopsin-T, a hyperpolarizing proton pump, to pace CMs or block their conduction [10]. Yu, et. al. developed a method for transducing primary fibroblasts for formation of tandem-cell units and optical pacing [11]. Applications of optogenetics in cardiac tissue include basic science problems, as well as translational applications such as high-throughput drug screening, His bundle pacing, painless defibrillation, and temporary block to test ablation sites (See [12–14] for review). In this work we use tandem-cell units with different donor cells to work on a variety of problems in cardiac electrophysiology, including studying fibroblast-cardiomyocyte coupling and chronically pacing cardiomyocytes *in vitro*.

Fibroblasts, cardiac injury, and myofibroblasts

Cardiac fibroblasts (CFBs) are mesenchymal cells primarily responsible for maintenance of cardiac extracellular matrix (ECM) [15], and release of paracrine factors [16, 17]. After cardiac injury, they are exposed to a number of signals that cause them to differentiate into myofibroblasts (MFBs), most prominently transforming growth factor

β (TGF-β1) and mechanical stress/substrate stiffness, but also angiotensin II and endothelin in the context of heart failure (See [18–24] for review). MFBs express smooth muscle actin (α-SMA), allowing them to contract the injured area, and produce large amounts of ECM, allowing them to mechanically stabilize the injury [20, 25]. They also produce TGF-β1 through their contraction, which releases and activates latent TGF-β1 in the ECM [26]. While MFBs are essential to wound healing, in some cases they persist long after scar is formed [19, 27], and even induce MFB differentiation in healthy areas through their release of TGF-β1 and ECM (termed reactive fibrosis [28–30]), possibly due in part to continued elevated circulating angiotensin II as well as local release by stressed CMs in the context of heart failure [31],. Once fully differentiated, MFBs no longer proliferate and will not dedifferentiate into CFBs, even in the absence of MFB-promoting signals [32]. MFBs and CFBs are best thought of as two ends of a spectrum, with at least one proto-MFB state in between [20, 23, 33, 34]. Exacerbating this difficulty in studying them, neither CFBs nor MFBs have specific markers [22, 31, 33, 34].

Cardiac fibroblast and myofibroblast electrophysiology

CFB and MFB electrophysiology is much less well understood than that of CMs. Part of the reason is that for many years, their electrophysiology was overlooked since they are unexcitable [17], and their main function is the production of paracrine factors and ECM [20]. Because CFBs spontaneously differentiate into MFBs in culture, with at least one intermediate, proto-MFB state between them, there can be a mixed population with very different electrophysiology without treatment to keep them in one state or another [32, 35]. This can result in inconsistent gene and protein expression [35]. Obtaining functional data via patch clamp presents even more challenges. Because

CFBs in culture are so flat, they are much more difficult to patch than CMs. MFBs have significantly higher resting potential (RP) than CMs [36, 37], and recent data has conclusively shown that CFB RP is between that of MFBs and CMs [35]. MFBs also have lower membrane resistance and increased size and capacitance than CFBs *in vitro* [35]. CFBs cycle calcium with a period of 30-130 s, and MFBs cycle slightly faster [38], so electrophysiology depends significantly on when during this cycle it is measured. Furthermore, CFBs and MFBs are highly mechanosensitive, with large depolarizations in RP during stretch [39], which has been proposed to be a mechanism of pressure-induced increases in beating rate [40].

While initially it was assumed CFBs had no relevant currents and simply acted to block conduction between CMs, with the discovery by Gaudesius that CFBs (likely MFBs) could conduct APs [41], computational models began to include CFB-CM conductance and passive membrane properties of CFBs, consisting of simply a capacitance, a net resting potential, and a total sarcolemmal conductance [42–45]. In the first example of this, Kohl, et. al. found that CFBs could increase spontaneous rate in the sinoatrial node, and further increase it during stretch, which they modelled as an increase in conductance of the CFB [46].

MacCannell, et. al. first created a model including active membrane currents [47]. They included a delayed rectifier potassium channel, based on patch clamp and western blot data from their lab [48], the inward rectifier channel I_{K1} based on strong expression of Kir2.1 [49], an assumed Na/K pump to maintain a cellular potassium gradient, as well as an assumed sodium leak to replace the sodium pumped out of the cell.

More recently, further rtPCR, RNAseq, and patch clamping have enabled the identification of a wide range of ion channels in CFBs and MFBs, including connexins [35], the delayed rectifiers Kcna6 (Kv1.6) [35, 48, 50] and Kcnh2 (Kv11.1, I_{Kr}) [35], inward rectifier Kcnj2 (Kir2.1, I_{K1}) [35, 48, 50], a sodium leak channel, Nalcn [35], as well as the subunits for Na/K/ATPase [35], as suggested by the MacCannell model. In addition, Cacna1c ($Ca_V1.2$, I_{CaL}) [35], BK_{Ca} (KCa1.1) [50], many TRP channels [35, 51, 52], a number of sodium channels, including the cardiac NaV1.5 [35], the sarcolemmal calcium pump, Atp2b1 [35], Kcnj8 with SUR2 (Kir6.1, K_{ATP}) [35, 48], and Kcnd3 channels (Kv4.3, I_{to}) [35, 50] have been found.

Modeling has shown that MFB electrical coupling can explain the increase followed by decrease in conduction velocity (CV) as a function of MFB density [53, 54] found experimentally [55]. It has also shown that elevation of CM RP is the likely reason for this slowing [36, 56], with MFBs acting as a current sink during depolarization as an additional reason for CV reduction [43, 54, 57].

Despite these advances, and the ability to study wide ranges of parameters and systems, modeling of CFB electrophysiology remains hampered by the lack of consistent measurements in experiments. This is likely because whether cells are CFBs or MFBs or in between is often not well characterized in experimental studies. Indeed, Salvarani, et. al. treated CFB with either TGF-β1 to produce a MFB phenotype, or the TGF-β receptor I blocker SB431542 to maintain them in a CFB state, as defined by the presence or absence of α-SMA, respectively, and found significant and complex differences in levels of channel expression between CFBs and MFBs, demonstrating the importance of controlling the phenotype of cells *in vitro* [35].

Mechanisms of myofibroblast arrhythmogenesis

Reentrant arrhythmia depends on two general factors – first, a substrate capable of supporting a reentrant circuit, and second, a trigger, in the form of unidirectional block, often caused by an ectopic beat [58]. After cardiac injury, including infarction, MFBs invade and secrete ECM, and arrhythmia risk is greatly increased [59, 60]. One mechanism by which this could occur is that MFB invasion and ECM production disrupts CM-CM connections, forcing conduction to move around the ECM and MFBs [36]. This increases the path length a wave can travel without running into repolarizing tissue. Since there is a minimum path length $\lambda = \theta \quad \mathrm{ERP}$ (path length = CV*effective refractory period) necessary to sustain reentry [58], this increases the arrhythmogenicity of the substrate. Furthermore, disruption of CM-CM connections creates variability in the path width, resulting in source-sink mismatches for the propagating wave [58]. This mismatch slows conduction, increasing arrhythmia risk by the formula above, and also increases the possibility of unidirectional block, a prerequisite for reentrant arrhythmia [58].

Studies have shown conduction slowing [35, 55, 61–66], increased spontaneous beating [55, 63, 64, 67], and increased propensity for arrhythmia [61, 64, 68] for CMs co-cultured with MFBs *in vitro*, suggesting MFBs contribute to arrhythmogenicity in ways other than CM-CM disruption. In addition to secreting ECM, MFBs may electrically connect to CMs, as they have been shown to do *in vitro* [56, 69, 70]. This electrical connection results in depolarization of the CM, since MFBs are more depolarized than CMs [35]. The raised RP inactivates sodium channels, reducing inward current during the action potential (AP) upstroke, which then reduces CV, contributing to arrhythmia [36]. Furthermore, inward current from the relatively depolarized MFBs can cause

diastolic depolarization of the CMs to the point of initiating an ectopic beat, providing a trigger for arrhythmia [36]. If calcium concentration is higher in the MFB, calcium influx into the CM may also initiate spontaneous beating by increasing CM intracellular calcium, resulting in calcium sparks and spontaneous beating via the calcium clock [71]. During depolarization, once the potential of the CM becomes more positive than that of the MFB, the outward currents in the MFB provide a current sink for the depolarizing sodium current in the CM, shunting current away from depolarizing downstream cells and slowing conduction [43, 54, 57]. Additionally, Pedrotty, et al. found that even when MFBs were not in contact with CMs, they could cause a significant (60%) reduction in CV through paracrine effects alone [72], presumably by remodeling CM ion channels, similar in magnitude to the reported slowing caused by MFBs in contact with CMs. Vasquez, et. al. also found statistically significant slowing by MFB-cultured media, although to a much lesser degree (11%). Thompson et. al. found MFB-induced conduction slowing could be reversed by application of mechanosensitive channel blockers, suggesting that MFB contraction may open CM mechanosensitive channels to generate deleterious inward and outward currents with the same downstream effects as those that could be produced by electrical coupling [61]. These putative mechanisms are summarized in Figure 1.

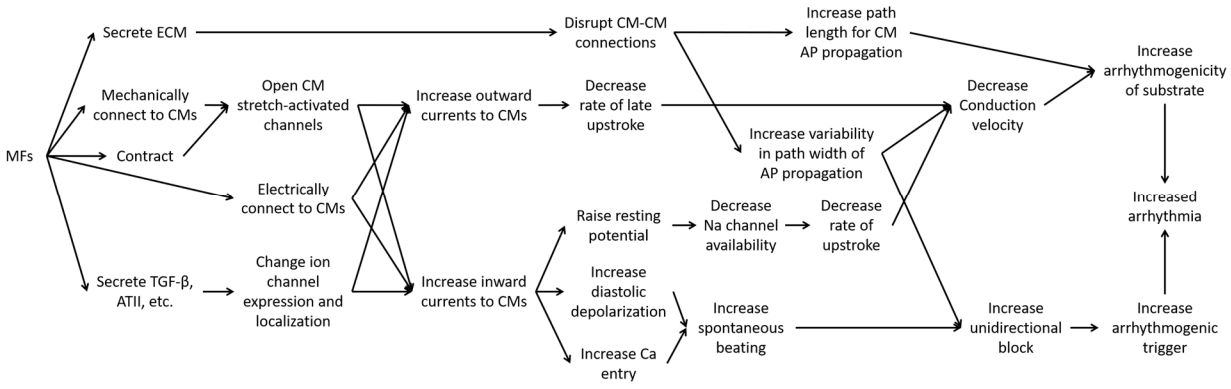

Figure 1. Putative mechanisms of myofibroblast arrhythmogenicity.

Teasing apart the relative importance of the various mechanisms by which MFBs slow CM conduction presents a difficult challenge. *In vitro* studies have plated MFBs on top of CMs, which should prevent MFBs or ECM from disrupting CM-CM connections, yet still find decreased CV and increased arrhythmia suggesting other mechanisms are also important [61, 63]. While MFBs produce many growth factors and other paracrine signals [73–75], the conflicting magnitudes of their effects on CMs when not in contact with them [62, 72] leaves significant contribution of paracrine signaling to MFB effects on CM in doubt.

The first thing to examine in considering the plausibility of electrical coupling being an important factor in MFB-induced arrhythmia is the evidence MFBs are functionally electrically coupled. This was first demonstrated in dual-cell patch clamp by Rook, et al. in 1992 [76]. Since then, other groups have used dye-transfer studies to suggest electrical coupling in syncytia [62, 64, 77–79]. However, one study found that MFB could induce slowing in CMs within 30 minutes of being added [80], significantly faster than half life of turnover of Cx43 (1.3-2 h) [81], casting doubt on necessity of an electrical mechanism for slowing.

Further evidence for an electrical mechanism is that in most studies, knockdown of Cx43 at least partially ameliorated MFB-induced conduction slowing [64, 68, 82], although one conflicting study found Cx43-knockdown MFBs slowed conduction just as much as control MFBs [61]. Furthermore, decreasing Cx43 expression inhibits TGF-β signaling [83] and CFB differentiation to MFB [83, 84], so Cx43 knockdown alone could reduce the number of MFBs present, increasing CV independent of a decrease in CM-MFB electrical connection. Another study found application of the K_{ATP} channel opener pinacidil improved CV in MFB-CM co-cultures, but had no effect on CM cultures, which presumably was because K_{ATP} channels were more abundant in MFB, and that opening them with pinacidil made their RP more similar to that of CMs [65]. This electrical mechanism is also bolstered by the fact that most, but not all, studies agree MFBs have more gap junction expression and function (See Table 10), as well as lower sarcolemmal resistance than CFBs [35], allowing these factors to explain why MFBs are arrhythmogenic and CFBs are not.

Evidence for mechanical coupling starts with the observations that MFBs are mechanically connected to CMs, contract, and can pull on CMs [61, 80], and that MFBs express more α-SMA than CFBs [20]. Furthermore, a seminal study by Thompson, et. al. found that the excitation-contraction uncoupler blebbistatin, or the mechanosensitive channel blockers Gd^{3+} and streptomycin, could ameliorate MFB-induced conduction slowing [61]. Later Grand, et. al. confirmed that Gd^{3+} and streptomycin could ameliorate conduction block [66]. However, they found no effect of blebbistatin or thrombin (expected to stretch the cells), and concluded that MFBs electrically depolarize CMs, and that mechanosensitive channels in CMs and/or MFBs are constitutively active and

can be blocked by mechanosensitive channel blockers, but that MFB contraction does not contribute to their opening [66]. Furthermore, other studies found stretch caused slowing in healthy heart, presumably without MFBs, and that it was not ameliorated by application of Gd^{3+} [85, 86]. Thompson et. al. bolstered the argument for a mechanical mechanism by showing knockdown of N-Cadherin could also ameliorate MFB-induced conduction slowing [80]. However, knockdown of N-cadherin concomitantly knocks down Cx43 [87], making it difficult to tease out which is more important. They also showed MFB transduced with dominant-negative RhoA reduced conduction slowing, and Rosker, et. al. showed application of cytochalasin-C and jasplakinolide, which prevent actin polymerization, could also reduce MFB-induced conduction slowing. However, RhoA and actin polymerization are part of the MRTF-SRF signaling pathway, which can also cause MFB differentiation [88], so these interventions may have simply prevented CFB differentiation into MFBs or dedifferentiated proto-MFBs.

In conclusion, while the weight of evidence remains in favor of electrical coupling between MFBs and CMs being the predominant mechanism of slowing, there is still conflicting data. Obviously, all of these mechanisms may work in parallel, and possibly even in tandem. For example, MFBs may stretch mechanosensitive channels in other MFBs, depolarizing them along with CMs to which they are electrically connected. This may be amplified by the nonlinearity of CV changes with respect to RP, as suggested by Grand, et. al. [66]. To address this, in Chapters 2 and 3, we develop a novel technique to use optogenetics to acutely evaluate the electrical mechanism, and determine if CFBs are connected enough to CMs to also cause slowing, provided enough inward current. Arguments for and against electrical and mechanical

mechanisms of slowing are summarized in Table 1. For additional reviews see [36, 45, 67, 89].

Question	Electrical Argument	Mechanical Argument
Why is MFB-induced CV slowing worse than CFB slowing?	• Cx43 expression/ conductance increase by MFBs or after myocardial injury [62, 79, 90] • N-Cadherin is decreased in MFBs [91]	• SMA expression increased in MFBs [20, 25] • N-Cadherin, shown to worsen slowing [80], slightly increased in MFBs [79]
Are CMs and MFBs electrically connected?	• Yes, as shown by dual patch clamp [35, 76] • Yes, as shown by dye transfer [62, 64, 77–79] • Yes, as shown by AP propagation through MFB [41, 76]	• Dye transfer between MFBs and CMs is much slower than MFB-induced CV slowing (5 h vs. 0.5 h) [80] • Cx43 turnover much slower than MFB-induced CV slowing [81]
Does Cx43 knockdown abrogate MFB-induced CV slowing?	• Yes, knockdown of Cx43 at least partly ablates MF-induced CV slowing [64, 68, 82]	• No, knockdown of Cx43 does not ablate MFB-induced CV slowing [61] • Knockdown of Cx43 decreases α-SMA expression [84], meaning any recovery may be due to decreased contraction
Does cadherin knockdown abrogate MFB-induced CV slowing?	• Knockdown of N-cadherin decreases gap junction expression and conductance [87]	• Yes, knockdown of N-cadherin (found to express at heterocellular junctions) abrogates MFB-induced CV slowing [80]
Is it reasonable each mechanism causes slowing?	• Yes, even HEK cells transduced with Cx43 slow conduction [78]	• Yes, external stretch exacerbates MFB-induced CV slowing [66]
Do appropriate ion channel drugs abrogate MFB-induced CV slowing?	• Yes, K_{ATP} channel openers hyperpolarize MFs and partially ablate MF-induced CV slowing [65] • No, mechanosensitive channel blockers Gd3+ [86] and Gs-Mtx-4 do not prevent stretch-induced decrease in CV, and Gs-Mtx-4 causes an increase in CV at baseline (while Gd3+ decreases CV at baseline) [85]	• Yes, mechanosensitive channel blockers Gd3+ and streptomycin at least partially ablate MFB-induced CV slowing [61, 66]

Does changing contraction/ stretch change MFB-induced CV slowing?	• Neither the contraction uncoupler blebbistatin nor contraction activator thrombin affects MFB-induced CV slowing [66] • RhoA and SMA polymerization are important for MFB differentiation [88], meaning any changes may be due to MFB dedifferentiation	• Yes, the contraction uncoupler blebbistatin ablates MFB-induced CV slowing [61] • Yes, dominant-negative RhoA ablates MFB-induced CV slowing [80] • Yes, α-SMA-affecting drugs Cytochalasin D, latrunculin B and Jasplakinolide at least partially abrogate MFB-induced CV slowing [63]

Table 1. Evidence for electrical versus mechanical mechanisms of conduction slowing caused by myofibroblasts.
Green shows arguments for the mechanism, red shows arguments against the alternative mechanism.

Maturation of cultured cardiac cells by electromechanical stimulation

Many studies have used electrical pacing and mechanical stimulation to attempt to mature cardiac cells [92, 93]. While early studies found differences between paced and unpaced tissues [94–98], the finding by Sathaye, et. al. that excitation-contraction uncoupling prevents pacing-related maintenance of longer APD in culture illustrated the importance of mechanical deformation [94]. More recently, important strides have been made by seeding cells on deformable substrates to allow them to contract during excitation. Radisic, et. al. found seeding neonatal rat CMs onto collagen sponges then stimulating at 1 Hz could increase maximum capture rate and sarcomere content, as well as produce intercalated discs that were almost absent in unstimulated constructs [99]. Lasher, et. al. found in fibrin-based engineered heart tissues (EHTs) that 1 Hz pacing increased the CM volume fraction and length/width ratio, as well as Cx43 expression at the cell membrane, effectively matching the properties of an age-matched native phenotype [100]. Hirt, et. al. expanded these results in EHTs to human induced

pluripotent stem cell-derived CMs (hiPSC-CMs), finding similar results, as well as increased contractility per cross-sectional area [101]. Nunes et. al. seeded hiPSC-CMs into a collagen gel in an elongated mold around a suture, to create a removable "biowire" [102]. These biowires were electrically paced at 6 Hz and had improved calcium handling as well as faster conduction than unpaced biowires [102]. Godier-Funemont, et. al. developed a method to allow for auxotonic contraction in neonatal rat ventricular myocyte (NRVM) EHTs, and found electrical pacing at 2-4 Hz upregulated RyR and SERCA, improving calcium handling, and increased t-tubule formation [103]. These alterations resulted in a positive force-frequency relationship, a first for engineered cardiac tissue [103]. Ronaldson-Bouchard, et. al. ramped up electrical stimulation of auxotonically contracting EHTs to 6 Hz, finding more adult-like gene expression, mitochondria density, metabolism and calcium handling [104]. These results demonstrate the importance of electrical pacing for CM maturation. Therefore, in Chapter 4, we use spark cells in tandem cell units to chronically pace CMs.

Cardiac extracellular matrix and decellularization

A significant goal in cell culture is to provide cells with the same structural, mechanical, and chemical signals *in vitro* that they receive *in vivo*, so that they behave similarly. For cardiac cells, substrate patterning is used to recreate the anisotropic structure of the heart [105], while gels are used to recapitulate the compliance of the heart, as well as its three-dimensionality [106], and culture media, supplemented with various growth factors, as well as other proteins and macromolecules, are used to provide the same chemical cues cells receive *in vivo* [107]. While 3-D bioprinting holds

promise for recapitulating many of these signals simultaneously, it remains a challenge [108].

In the body, ECM, a network of proteins and other macromolecules, surround cells and provide these cues[109, 110]. Since the seminal work by Ott et al. demonstrating the decellularization and subsequent repopulation of a rat heart [111], the use of decellularized native tissues as natural scaffolds for engineered cardiac tissues has become widely investigated [112]. A common method to decellularize cardiac tissue is perfusion of the whole organ with detergents and/or enzymes, and has been successfully applied to rat [111, 113–115], pig [116], and mouse [117] hearts. However, recellularization of the decellularized heart, either through the coronary circulation or by direct injection, has not succeeded in repopulating the tissue evenly.

The ability to provide cues from ECM in vitro would be beneficial for our other projects, since substrate stiffness [118–120] and composition [121, 122] affect CFB differentiation into MFB, and as noted in the previous section, a deformable substrate may be important in further maturing cells using our optical pacing system. In Chapter 5, we develop such a substrate using decellularized matrix from pig hearts.

Chapter 2: Inward current in myofibroblasts can cause electrophysiological changes in cardiomyocytes

Introduction

After myocardial injury, CFBs are activated by mechanical stiffness and paracrine factors, most prominently TGF-β1 [20]. These activated CFBs migrate to the injury and differentiate into MFBs, which contract in order to stabilize and shrink the injured area, and manufacture and secrete ECM to fill in areas where cells died [18, 20]. Although there is no clear boundary between CFBs and MFBs [123], a hallmark of fully differentiated MFBs is organized α-SMA fibers [20, 32].

Arrhythmia risk is significantly increased after cardiac injury [36, 67]. There are many contributing factors to this, such as interruption of CM coupling by scar, resulting in zigzag propagation or electrical block, and electrical remodeling [36, 67]. However, an additional factor may be the effects of MFBs themselves on cardiac electrophysiology. In simplified *in vitro* systems, addition of MFBs to CMs has been shown to slow CM CV and increase spontaneous beating rate [35, 36, 61, 63, 67, 68, 70, 124, 125], which can produce both a substrate and trigger for arrhythmia. Indeed, *in vitro* studies have shown spiral wave formation is more common in MFB/CM co-cultures than in CM cultures alone [61, 63, 68, 125]. While most groups argue that electrical coupling between CMs and relatively depolarized and unexcitable MFBs is the major factor in conduction slowing [35, 55, 62–64, 66], alternative hypotheses include paracrine [72] and mechanical mechanisms [61, 80].

As outlined in Chapter 1, because of the possibility of paracrine signaling effects, as well as the extensive cross-talk between Cx43 expression and MFB differentiation [84], verifying the proposed electrical mechanism of MFB-induced conduction slowing remains challenging. Some studies have used FRAP as evidence of diffusional (and therefore presumably electrical) coupling between CMs and MFBs [62], but these cannot be translated to a value of electrical conductance [126] or show that the connection is strong enough to cause significant slowing in CMs. Dual-cell patch clamp has been used to quantify the electrical connection between CM and MFB pairs [35, 76], but not in a syncytium, which can have differences in electrophysiology because of the difference in cell density [127], and allows for measurement of macroscopic CV.

In this *in vitro* and *in silico* study, we transduced MFBs with the optogenetic protein ChR2, a relatively non-selective cation channel that opens in response to light [6], to acutely modulate their currents. In so doing, we were able to demonstrate acute changes in CM electrophysiology in response to changes in MFB currents, demonstrating MFBs are electrically coupled to CMs, and that this coupling can in fact acutely cause slowing and spontaneous beating in CM syncytia.

Methods

Cardiomyocyte isolation and culture

All animal procedures were performed in compliance with guidelines set by the Johns Hopkins Committee on Animal Care and Use and all federal and state laws and regulations. Cell culture media consisted of Medium 199 (Gibco) supplemented with 1% HEPES buffer solution (Gibco), 1% MEM non-essential amino acids (Gibco), 20 μM

glucose (Millipore-Sigma), 2 mM L-glutamine (Life Technologies), 4 μg/mL vitamin B-12 (Millipore-Sigma), 1% penicillin (Millipore-Sigma) and 10% fetal bovine serum (FBS, Millipore-Sigma). The hearts of 2-day-old Sprague-Dawley rats (Harlan, Indianapolis, IN) were excised, cut into 4-6 pieces, rinsed twice in HBSS, placed in 40 mL 0.25 mg/mL filtered trypsin (Millipore-Sigma) in HBSS solution in a sealed glass container, and rotated at 110 rpm at 4°C overnight (13-16 h). The next day as much trypsin solution as possible (without removing cells) was pipetted out, and the remainder quenched by adding 25 mL 10% FBS media. The tissue was rotated at 150 rpm in a warm water bath for 3 min. Then, excess media was removed, and 9 mL of 1 mg/mL collagenase (Worthington, Lakewood, NJ) in HBSS was added before sealing the glass container holding the tissue and placing it back in the warm water bath for 3 min. After this, excess solution was removed and discarded and another 9 mL of collagenase solution was added, the glass container was sealed and rotated in the warm water bath again for 3 min, the cells were pipetted up and down three times, and the excess solution was removed and placed in a 15 mL centrifuge tube with 4 mL cold HBSS, which was placed in ice to quench the collagenase activity. This was done 3 more times. The tubes were centrifuged at 3,000 rpm for 8 min, excess solution was aspirated, and the cells were pipetted out into 10 mL of cold HBSS. They were then triturated by pipetting before being passed through a 40 μm nylon cell strainer (BD Falcon, Franklin Lakes, NJ). The cells were then centrifuged again for 5 min at 1,000 rpm and 1 min at 3,000 rpm, HBSS was removed by aspiration, cells were resuspended in 15 mL 10% FBS media, and preplated for one hour in a 175 cm^2 flask (Sarstedt, Newton, NC) to isolate CFBs. They were then preplated again in 25 mL 10% FBS

media in a 175 cm^2 flask (Sarstedt) for one hour. The supernatant, consisting of purified CMs, was removed and cells were counted using a hemocytometer (Thermo Fisher Scientific, Hampton, NH). NRVMs were plated onto coverslips coated with 25 μg/mL fibronectin at 1 million per well for a 12-well plate or 500,000 per well for a 24-well plate.

Myofibroblast transduction and culture

MFBs used in experiments were produced by passaging cells from the first preplate twice (on day 4-5 and 11-12) and transducing them with ChR2-YFP fused adenovirus (plasmid pcDNA3.1/hChR2(H134R)-EYFP from Addgene (Cambridge, MA), pBR322 backbone adenovirus, CMV promoter) from the Entcheva group at approximately 2000 MOI as described previously [11] during the second passage, with media changed 4-6 hours later to remove virus. They were then were treated with 5 ng/mL TGF-β1 (R+D Systems) four days after transduction to fully differentiate them into MFBs. These procedures were followed for pilot experiments except that MFBs were plated onto 0.1% gelatin-coated 24-well #0 glass-bottom plates (Cellvis) at 200,000/well, and 0, 1000, 2000, or 5000 MOI of virus was added to some of the wells. Eight days after plating cells were fixed and stained for YFP (Invitrogen GFP Ab), α-SMA (Sigma), and DAPI using standard protocols. Cells were then imaged using a confocal microscope (LSM 710NLO-Meta, Zeiss).

Optical stimulation and recording

To optically stimulate and record voltage, a custom setup was created. Red (λ=655 nm) and blue (λ=448 nm) LED modules (Luxeon SinkPAD-II Rebel 7 LED Round Modules) were arranged perpendicularly, with a dichroic mirror (λ= 475 nm) between them at a 45° angle (Figure 2). The red LED was connected to a 15 V

regulator and powered at 18 V by a variable power supply (Tekpower TP3005). The blue LED was connected directly to the power supply. In early iterations a green LED (530 nm) was used instead of the red LED, or a 690/60 nm filter (Omega Optical) was placed in front of the red LED. The spectra of the LEDs were measured using a spectrometer (Ocean Optics, USB4000). For the green LED, a coverslip coated in PSCRed (Brewer Science, Rolla, Mo) was used as the base of the experimental chamber, as an emission filter. For the red LED, initially 715 nm or 760 nm long pass filters (Newport, catalog no. 20CGA-715 or 20CGA-760) made up the base of the experimental chamber, as emission filters, before being replaced with two 717 nm Wratten filters (Kodak, 717FWP7575) affixed to a 1 mm glass slide using clear packing tape (Scotch Heavy Duty) in the final iteration. In every iteration, the distance between the voltage-sensitive dye excitation LED and the fiber optics that led to the photodiode sensors was varied to give an optical signal just below saturation of the photodiodes to maximize signal-to-noise.

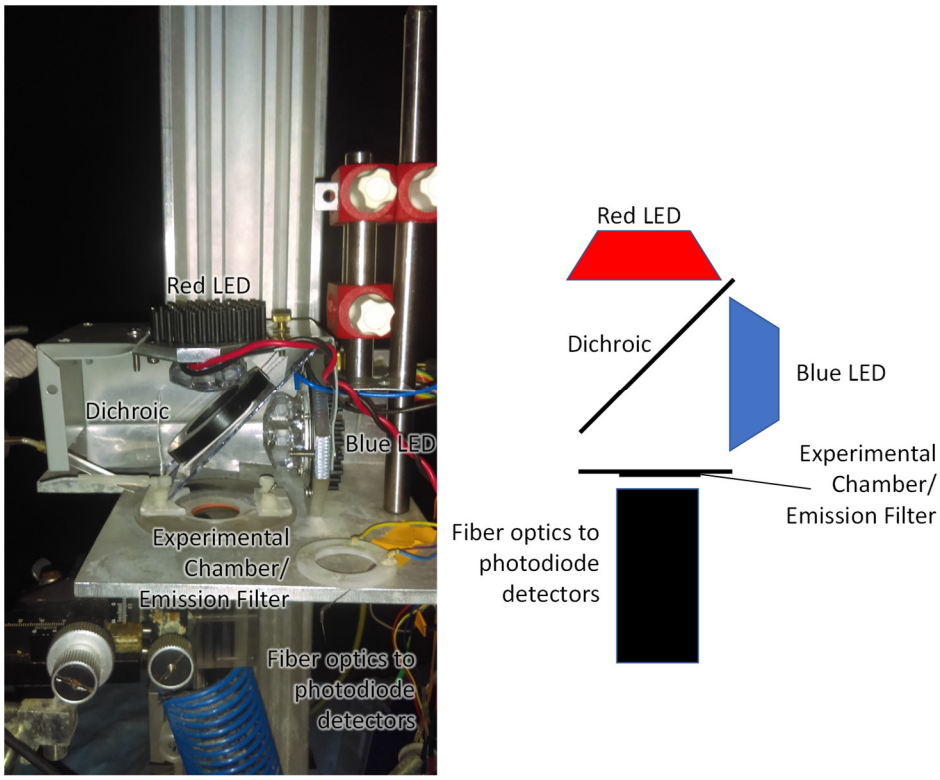

Figure 2. Optical stimulation and recording setup.

Testing voltage-sensitive dye

di-4-ANBDQBS was dissolved at 17.5 mM in ethanol, before being diluted 1:500 in Tyrode's to achieve a final concentration of 35 μM before being added to CMs as done previously [128]. CMs were then imaged using confocal microscopy. Bleed-through of red light through emission filters was determined by placing a spectrometer (Ocean Optics) under the two initial emission filters. Changes in exposure time were used to compensate for the limited dynamic range of the sensor. The fluorescence properties of the dye was compared to that of di-4-ANEPPS by dissolving both stocks (di-4-ANEPPS stock is 4mM in DMSO) in PBS at concentrations ranging from ¼ the recommended dose (1:500 dilution for di-4-ANBDQBS, 1:1000 dilution for di-4-ANEPPS), up to 512x the recommended dose, increasing by factors of two (the

highest dose for di-4-ANBDQBS was actually 500x, the undiluted stock solution), and measuring fluorescence at different excitation frequencies in a plate reader. Some samples had only PBS for background subtraction.

Co-culture, imaging, and optical mapping

ChR2-transduced MFBs (ChR2-MFBs) or untransduced MFBs were added to 4-5-day-old CM monolayers at 400,000/well in a 12-well plate or 200,000/well in a 24-well plate (approximately 100,000/cm^2), giving an MFB:CM cell ratio of 0.4. On days 5-8, co-cultures were imaged under phase contrast and fluorescence (Eclipse TE2000U, Nikon) to examine their morphology and continued expression of ChR2, then placed in a custom optical mapping system [129] and stained for 5 minutes with 35 μM of the voltage-sensitive dye di-4-ANBDQBS (from Dr. Leslie Loew, University of Connecticut). Tyrode's solution (1.8 mM $CaCl_2$, 5 mM glucose, 5 mM HEPES, 1 mM $MgCl_2$, 5.4 mM KCl, 135 mM NaCl, and 0.33 mM NaH_2PO_4 in ddH_2O pHed to 7.37 with NaOH, all chemicals from Sigma-Aldrich) at 35°C was then continuously flowed over the cells. The pacing threshold with 10 ms pulse width was determined to within 1 V, and the cells were point paced at 1.1x threshold for 5 min at 2 Hz to reach steady-state. A baseline optical recording was taken, then continuous blue light to open ChR2 channels was applied across the entire monolayer for about 2 seconds before and then during a 2 second recording, after which the light was switched off, and a post-ChR2 activation recording was collected as soon as possible (within seconds). This allowed for recording at a steady state of ChR2 current, since the activation, inactivation and closing kinetics all have time constants <25 ms [5]. This was done for increasing light intensities. After optical mapping, monolayers were fixed and stained for α-actinin

(Sigma), α-SMA (DAKO), Cx43 (Sigma), YFP (Invitrogen GFP Ab), and/or DAPI before imaging (LSM 710NLO-Meta, Zeiss).

Acute myofibroblast strain energy measurements

MFBs were produced as described above, except after the second passage, 10,000 cells were plated in a 35-mm dish onto force-sensing micropost arrays produced as described previously [130]. Cells were imaged 20 h after seeding via bright field using an inverted microscope (Nikon TE-2000), 60 s before application of 30 s high intensity (1.2 mW/mm^2) blue light, as well as 60 s after. Micropost images were analyzed using Igor Pro (Wavemetrics) by a centroid-fitting method to track their positions $\vec{x}$ (Crocker et al 1996). Microposts' undeflected positions $\vec{x}_{undeflected}$ were calculated by fitting to a hexagonal grid. Total strain energy, calculated as $E = \sum \frac{1}{2} k \mid \vec{x} - \vec{x}_{undeflected} \mid^2$, was used as the scalar metric to measure cellular static force, since vector sum of cellular force will be zero. These experiments were conducted by Yu Shi.

Mathematical model

Experimental data was modeled in MATLAB (The MathWorks, Natick, MA) using a modified version of the Korhonen model for NRVMs [131]. Currents for MFBs were modeled by a hyperbolic least squares fit of $I_{MFB} = (a \tanh(V_{MFB} + b) + c)(V_{MFB} + b) + d$ to the I/V curve measured by Salvarani for TGF-β1-treated CFBs [35], then simplified to $I_{MFB} = \frac{\tanh\left(\frac{V_{MFB}+20}{10}\right)+2}{50}(V_{MFB} + 20)$

(Figure 3). In addition to those endogenous currents, the Williams model for ChR2 current (I_{ChR2}) [132] was added to the MFB (Figure 4).

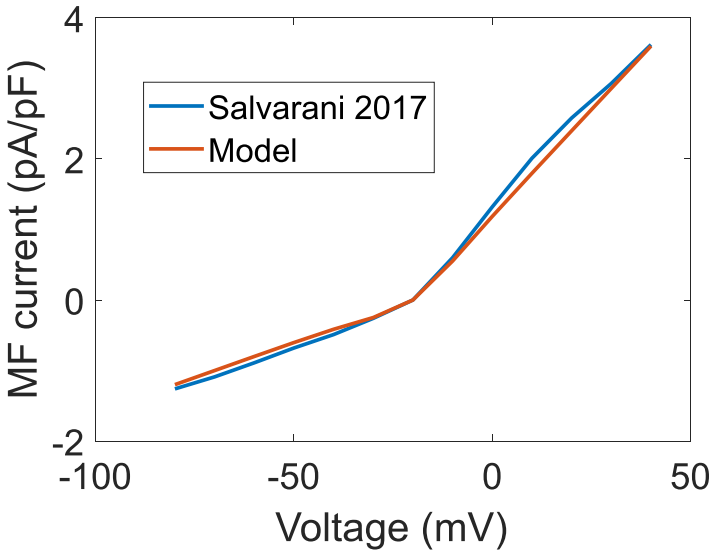

Figure 3. Myofibroblast current-voltage fit to experimental data.
Hyperbola was fit to data from TGF-β1-treated cells in [35].

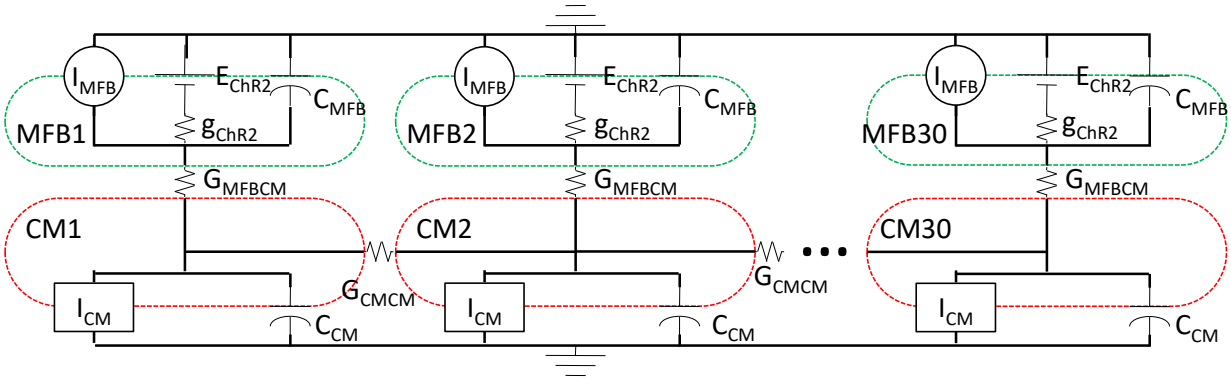

Figure 4. Model schematic.
ChR2 channel (G_{ops}, E_{ops}) from Williams [132] was added to MFB model based on Salvarani data [35]. MFBs were electrically connected to CMs (G_{MFBCM}), which were connected to each other (G_{CMCM}) to form a 30 cell, 1.5 mm 1-D cable. The dashed lines show the outer boundaries of the CMs (red) and MFBs (green). Values and formulas for variable are listed in Table 2 and Table 3.

Each CM was connected via a lumped gap junction to a MFB (Figure 4). MFBs were assumed to have approximately the same capacitance as CMs on a cellular basis,

as done previously [133]. Although the MFB:CM ratio was 0.4, to simplify modeling, we modeled one MFB connected to each CM, and simply multiplied its capacitance by 0.4. This was possible because on a scale on the order of tens of cells, the total membrane area of each cell type is the main determinant of CV, so a small number of large MFBs can be changed to a large number of smaller MFBs (See [133], which found only ~5% decrease in CV across a wide range of MFB densities when decreasing MFB size by a factor of 4 but keeping total MFB membrane area constant.) Each CM was 50 μm long, 50 μm wide, and 5 μm thick, based on previous measurements [133], resulting in a CM capacitance of 60 pF, given C_m=1 μF/cm^2 (Table 2). Cell dimensions for calcium handling equations were not changed from the original model, since the calcium handling is highly dependent on them, and the original model was calibrated based on those specific dimensions. A 30-cell-long 1-D strand of ChR2-MFB/CM cell pairs was modeled (Figure 4). Neighboring CMs were connected by lumped gap junctions with a conductance G_{CMCM} of 50 μm*7.74 nS/μm=385 nS, based on the measurements by Salvarani [35] (Figure 4 and Table 2-Table 4). Neighboring MFBs were not connected to each other to prevent them from having “double-sided” effects on CM [134], by creating an alternate current path. We investigated a wide range of G_{MFBCM}, since this value is unknown in a syncytium, as well as a range of light intensities that includes those applied experimentally, to examine the effects on spontaneous beating and CV.

$$C = C_m(2lw + 2l \quad + 2w \quad) = 1 \quad (2 \quad 0.005 \quad 0.005 + 2 \quad 0.005 \quad 0.0005 + 2 \quad 0.005 \quad 0.0005)$$

$$= 0.00006$$

$$\frac{dV_{CM}}{dt} = \quad \left(I_{CM} + \frac{I_{MFBCM} + I_{CMCM}}{C}\right)$$

$$I_{CM} = I_{CaL} + I_{CaT} + I_{NCX} + I_{Cab} + I_{Nab} + I_{NaK} + I_{Na} + I_f + I_{K1} + I_{to} + I_{Ks} + I_{Kr} + I_{stim}$$

$$\frac{dV_{MFB}}{dt} = \quad \left(I_{MFB} + I_{ChR2} \quad \frac{I_{MFBCM}}{Cr_{MFBCM}}\right)$$

$$I_{MFB} = \frac{\tanh\left(\frac{V_{MFB} + 20}{10}\right) + 2}{50} \quad (V_{MFB} + 20)$$

$$I_{ChR2} = g_{ChR2}G(O_1 + \gamma O_2)(V_{MFB} \quad E_{ChR2})$$

$$I_{MFBCM} = G_{MFBCM}(V_{CM} \quad V_{MF})$$

$$G_{CMCM} = w\gamma_{CMCM} = 0.005 \quad 0.0774 = 0.000385$$

$$I^i_{CMCM} = G_{CMCM}\left(2V^i_{CM} \quad V^{i-1}_{CM} \quad V^{i+1}_{CM}\right)$$

Table 2. Model equations for myofibroblasts and linking cells into a strand.
Units are ms, mV, nA, μF, cm, mS. Sarcolemmal currents are normalized to cell capacitance, intercellular currents are not. Superscript i denotes which cell (i.e. 1-30) the variable refers to. While all variables may have a different value for each cell, the equations for each cell are the same, so the superscript is omitted for simplicity, except for in the equation for I^i_{CMCM}, in which neighboring CMs in the strand interact.

Parameter	Description	Value	Reference
l	Cell length (cm)	0.005	[133]
w	Cell width (cm)	0.005	[133]
h	Cell height (cm)	0.0005	[133]
r_{MFBCM}	Ratio of MFB number to CM number	0.4	Plated ratio in experiments
g_{ChR2}	ChR2 conductance per area (mS/uF)	0.4	[132]
γ	Conductance ratio of ChR2 high (O_1) and low (O_2) conductance open-states	0.1	[132]
E_{ChR2}	ChR2 reversal potential (mV)	0	[132]
G_{MFBCM}	MFB-CM conductance (μS)	Varied from $10^{-4.5}$ to 10^{-1}	
γ_{CMCM}	CM-CM conductance per interfacial length (nS/μm)	77.4	[35]

Table 3. Myofibroblast, ChR2, and 1-D strand model parameters from Table 2.

Variable	Description
V_{MFB}	MFB transmembrane voltage (mV)
I_{MFB}	MFB endogenous transmembrane current (pA/pF)
I_{ChR2}	ChR2 current (pA/pF)
I_{MFBCM}	MFB-CM intercellular current (nA)
$C = C_{CM} = C_{MFB}$	CM and MF capacitance (μF)
G	voltage-dependent rectification function
O_1	ChR2 high conductance open-state probability
O_2	ChR2 low conductance open-state probability
E_{ChR2}	ChR2 reversal potential (mV)
V_{CM}	CM transmembrane voltage (mV)
C_m	Membrane capacitance per area (μF/cm^2)
I_{CaL}	L-type calcium current (pA/pF)
I_{CaT}	T-type Ca current (pA/pF)
I_{NCX}	Sodium/Calcium exchanger current (pA/pF)
I_{Cab}	Background calcium current (pA/pF)
I_{Nab}	Background sodium current (pA/pF)
I_{NaK}	Sodium/Potassium ATPase current (pA/pF)
I_{Na}	Fast sodium current (pA/pF)
I_f	Hyperpolarization activated (funny) current (pA/pF)
I_{K1}	Time-independent potassium current (pA/pF)
I_{to}	Transient outward potassium current (pA/pF)
I_{Ks}	Slow delayed rectifier potassium current (pA/pF)
I_{Kr}	Rapid delayed rectifier potassium current (pA/pF)
I_{stim}	External stimulus current (pA/pF)
G_{CMCM}	CM-CM conductance (μS)
I_{CMCM}	CM-CM intercellular current (nA)
I_{CMCM}^{i}	CM-CM intercellular current for cell i in the strand (nA)
V_{CM}^{i}	CM transmembrane voltage for cell i in the strand (mV)

Table 4. Model variable definitions from Table 2.

Changes were made to make the model better match prior experimental data, and to enable the presence of spontaneous beating, which occurs at rates of up to 6 Hz in our experiments, but never exceeds 0.6 Hz in the baseline model. First, to speed simulations, sodium and potassium concentrations were fixed at initial levels (Table 5). L-type calcium channel calcium gates (α_{fCa}) were allowed to recover at voltages more depolarized than -60 mV (Table 5, see [131] for full model). This prevents a step change in recovery rate which isn't justified physiologically. While this rule has almost no effect on control cells during normal pacing, in the original model, it almost completely prevents L-type calcium channel recovery when depolarized by MFBs. Also, the I_{Ks} α_n and β_n were multiplied by a factor of 18 so the maximum rates matched those found in guinea pig ventricle [135], and the I_{Ks} time constant was changed to the standard form $\tau_{nKs} = \frac{1}{\alpha_n + \beta_n}$ instead of being set to a constant (Table 5 and Figure 5, see [131] for full model).

Original	Modified
Intracellular sodium concentration	
$\frac{d[Na^+]_i}{dt} = \left(I_{fNa} + I_{Nab} + I_{Na} + 3I_{NCX} + 3I_{NaK}\right)\frac{A_{cap}C_m}{FV_{cyto}\ \ 10^{-6}}$	$\frac{d[Na^+]_i}{dt} = 0$
Intracellular potassium concentration	
$\frac{d[K^+]_i}{dt} = \left(I_{fK} + I_{to} + I_{K1} + I_{Ks} + I_{Kr}\ \ 2I_{NaK} + I_{stim}\right)\frac{A_{cap}C_m}{FV_{cyto}\ \ 10^{-6}}$	$\frac{d[K^+]_i}{dt} = 0$
L-type calcium current	
$I_{CaL} = G_{CaL}df f_{Ca}4\frac{VF^2}{RT}\frac{[Ca^{2+}]_{subSL}e^{\frac{2VF}{RT}}\ \ 0.341[Ca^{2+}]_o}{e^{\frac{2VF}{RT}}\ \ 1}$	Same
$\frac{df_{Ca}}{dt} = \begin{cases} 0 & \mid f_{Ca\infty} > f_{Ca}\ \&\ V > \ \ 60 \\ \frac{f_{Ca\infty}\ \ f_{Ca}}{\tau_{f_{Ca}}} & ot\ \ erwise \end{cases}$	$\frac{df_{Ca}}{dt} = \frac{f_{Ca\infty}\ \ f_{Ca}}{\tau_{f_{Ca}}}$
$f_{Ca\infty} = \frac{\alpha_{fCa} + \beta_{fCa} + \gamma_{fCa}}{1.46}$	Same
$\alpha_{fCa} = \left[1 + \left(\frac{[Ca^{2+}]_{subSL}}{0.4875}\right)^8\right]^{-1}$	$\alpha_{fCa} = \left[1 + \left(\frac{[Ca^{2+}]_{subSL}}{0.718}\right)^8\right]^{-1}$
Slow delayed rectifier potassium current	
$I_{Ks} = G_{Ks}{n_{Ks}}^2(V\ \ E_K)$	Same
$\frac{dn_{Ks}}{dt} = \frac{n_{Ks\infty}\ \ n_{Ks}}{\tau_{n_{Ks}}}$	Same
$n_{Ks\infty} = \frac{\alpha_n}{\alpha_n + \beta_n}$	Same
$\alpha_n = \frac{0.00000481333(V + 26.5)}{1\ \ e^{-0.128(V+26.5)}}$	$\alpha_n = \frac{0.00008663994(V + 26.5)}{1\ \ e^{-0.128(V+26.5)}}$
$\beta_n = 0{:}0000953333e^{-0.038(V+26.5)}$	$\beta_n = 0.0017159994e^{-0.038(V+26.5)}$
$\tau_{n_{Ks}} = 750$	$\tau_{n_{Ks}} = \frac{1}{\alpha_n + \beta_n}$

Table 5. Original and modified ion channel equations from Korhonen model.
For simplicity, V=V_{CM} in this table. Units are ms, mV, nA, μF, cm, and mS.

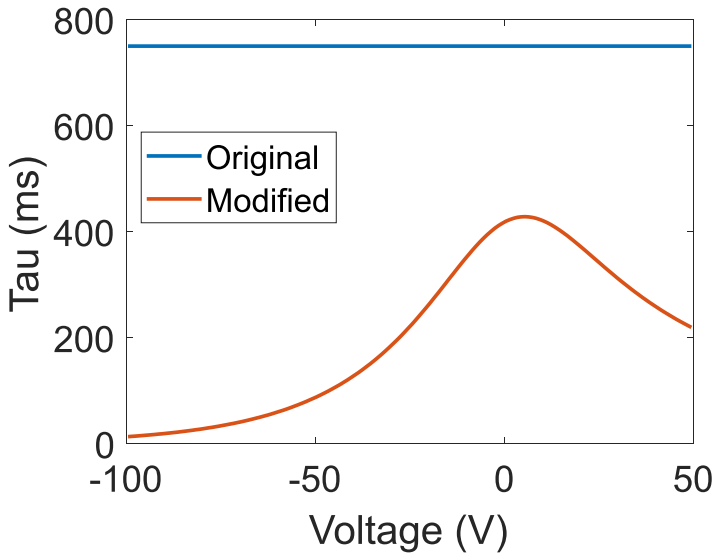

Figure 5. Original and modified $\tau_{n_{Ks}}$ as a function of V.

To optimize the model to increase spontaneous beating in the presence of inward currents, without significantly altering the parameters in the model or the functional outputs, a minimization function was run, wherein the maximimal conductances of all the sarcolemmal CM channels, as well as the calcium gating sensitivity of the L-type calcium channel (α_{fCa}, see Table 5) and the calcium diffusion time constant between the uptake and release compartments of the SR (τ_{tr}, see Table 6) were varied and tested in the model, to minimize the function $S = S_{RP_S^O} + S_{f_S^O} + S_{APA_P^O} + S_{RP_P^O} + S_{ADA_P^O} + S_{APD_P^O} + S_{APA_S^M} + S_{f_S^M} + S_{fr} + S_{\Delta x}$ representing parametric and functional differences from the original model.

Parameter	Definition	Original Value	Modified Value
τ_{tr}	Time constant for transfer from the uptake region of sarcoplasmic reticulum to release region (ms)	200	92
G_{Ks}	Maximum I_{Ks} conductance (mS/μF)	0.05	0.11
G_{Kr}	Maximum I_{Kr} conductance (mS/μF)	0.06	0.03
G_{Na}	Maximum I_{Kr} conductance (mS/μF)	35	150

Table 6. Original and modified parameters from the Korhonen cardiomyocyte model.

Next the model of a single MFB-CM cell pair (i.e. MFB1 and CM1 only) was run under three different conditions (Figure 4). The first was CM only (i.e. $G_{MFBCM} = 0$, denoted by superscript O) and unpaced (denoted by subscript S for spontaneous) to determine the resting potential (RP_S^O) and spontaneous beating rate (f_S^O, see Table 7 for these and the other scoring equations). The squared difference between RP_S^O and the original RP (-67 mV) divided by 15 mV (the chosen maximum acceptable difference) gave the RP component of the score ($S_{RP_S^O}$). Similarly, the score for spontaneous rate ($S_{f_S^O}$) was calculated such that any rate between 0, the spontaneous rate of the model, and 0.7 Hz, the spontaneous rate we observed experimentally (0.7 Hz, See Figure 37A in Chapter 4), would yield a score of 0, and above that the score would be the squared difference between the spontaneous rate and 0.7 divided by 2 Hz, the maximal acceptable spontaneous rate that would allow us to overdrive pace at 2 Hz. For the second set of conditions, we paced (denoted by subscript P) the CMs to determine action potential amplitude (APA_P^O), APD_{80} (APD_P^O), maximum diastolic potential (RP_P^O), and afterdepolarization amplitude (ADA_P^O). As before, AP amplitude score $S_{APA_P^O}$ was the squared difference of APA_P^O and that of the original model (85 mV) divided by 20 mV,

the chosen maximum acceptable difference. Similarly, maximum diastolic potential score ($S_{RP_P^O}$) was the squared difference in RP_P^O between the modified and original model (-65 mV), divided by the maximum acceptable difference, 15 mV, and afterdepolarization amplitude score ($S_{ADA_P^O}$) was the squared difference in ADA_P^O between the modified and original model (0 mV), divided by 10 mV. Finally, APD_{80} score ($S_{APD_P^O}$) was calculated such that the range between 180 ms and 220 ms would result in a score of 0, since the APD of the original model (214 ms) and we found 184 ms APD experimentally. We used 50 ms as the maximum acceptable difference in the denominator. For the final condition, the model was run with ChR2-MFBs attached and strong (1 mW/mm^2) light (denoted by M superscript). Spontaneous beating amplitude (APA_S^M) and rate (f_S^M) were calculated under these conditions. The spontaneous beating amplitude formula assigned any amplitude above 50 mV a score ($S_{APA_S^M}$) of 0, while using the usual squared difference between APA_S^M and 50 mV divided by 50 mV. The spontaneous rate score ($S_{f_S^M}$) incorporated two elements. The first was to match the experimental maximum capture rate (6 Hz). The second was to account for the fact that the spontaneous rate needed to be greater than 2 Hz to be detected, since that was the external pacing rate. Therefore, at rates below 2.65 Hz a linear equation with a constant slope of 1.6 was used. Next, the ratio of spontaneous beating rate with ChR2-MFBs, f_S^M, divided by that without, f_S^O, was scored (S_{fr}) such that a ratio above 2 scored 0, while a ratio below 2 was scored as the squared difference between the ratio and 2. Finally, the changes to the model parameters were scored by the formula $S_{\Delta x} = \sum_i \left(\omega_i \left(\max\left(x_i, \frac{1}{x_i}\right) \quad 1 \right) \right)^2$, where x_i is the factor by which each parameter was

multiplied. $\omega_i = 1$ if the parameter is defined based on experimental data, which was the case for the expression level of I_{CaL}, I_{CaT}, I_f, I_{K1}, and I_{to}, [131], and $\omega_i = 0.1$ if it was defined empirically in the original model, which was the case for all the other variables. See Table 7 for all formulas.

Model Conditions	Score component	Score formula
CM only Unpaced	Resting potential (mV)	$S_{RP_S^O} = \left(\frac{RP_S^O \quad (\quad 67)}{15}\right)^2$
	Spontaneous beating rate (Hz)	$S_{f_S^O} = \left(\frac{\max(0,\ f_S^O \quad 0.7)}{2}\right)^2$
CM only Paced	Action potential amplitude (mV)	$S_{APA_P^O} = \left(\frac{APA_P^O \quad 85}{20}\right)^2$
	Maximum diastolic potential (mV)	$S_{RP_P^O} = \left(\frac{RP_P^O \quad (\quad 65)}{15}\right)^2$
	Afterdepolarization amplitude (mV)	$S_{ADA_P^O} = \left(\frac{ADA_P^O}{10}\right)^2$
	Action potential duration (ms)	$S_{APD_P^O} = \left(\frac{\max(abs(APD_P^O \quad 200) \quad 20}{50}\right)^2$
ChR2-MF and light Unpaced	Spontaneous action potential amplitude (mV)	$S_{APA_S^M} = \left(max\left(\frac{50 \quad APA_S^M}{50}, 0\right)\right)^2$
	Spontaneous beating rate (Hz)	$S_{f_S^M} = \begin{cases} \left(\frac{f_S^M \quad 6}{6}\right)^2 & \mid f_S^M > 2.65 \\ 4.6 \quad 1.6 f_S^M & \mid f_S^M < 2.65 \end{cases}$
Other	Ratio of spontaneous rate with ChR2-MF and light vs. without	$S_{fr} = \left(\max\left(0,\ 2 \quad \frac{f_S^M}{f_S^O}\right)\right)^2$
	Change in parameters	$S_{\Delta x} = \sum_i \left(\omega_i \left(\max\left(x_i, \frac{1}{x_i}\right) \quad 1\right)\right)^2$

Table 7. Formulas for components of scores for optimization.

Data processing and statistics

Mapping data was processed by custom MATLAB software. Data was linearly detrended and low-pass filtered with a cutoff frequency of 32 Hz. A Fourier transform for

each channel was calculated and used to exclude channels which had a different dominant frequency than the pacing frequency, since in a captured, non-noisy channel, the dominant signal frequency should be the paced frequency (after blanking out frequencies < 0.5 Hz, since these can be large due to artifacts from the finite signal duration). A 5-point derivative was calculated, and channels with more than 6 signal direction changes (i.e. derivative zero-crossings) per pace were excluded, since an ideal signal will only have 2 per pace (at the peak and trough of the paced wave), and a noisy signal will have more. In some cases, these filters were supplemented by manual removal of channels with poor signal. Activation maps were constructed using the time of maximum upstroke rate (derivative) of the AP. Monolayers with initial CV below 10 cm/s were excluded from analysis.

ChR2 spectral efficiency (E) was calculated as the mean of the ChR2 current response (ε) from [3] weighted by the spectral power (I) of each LED module, measured over all wavelengths (λ): $E = \frac{\sum_\lambda I\varepsilon}{\sum_\lambda I}$. Confocal images were processed by FIJI [136] and Zen Black (Zeiss) software. Strain energy was processed using Igor Pro (Wavemetrics). All data are presented as mean±SD. Unpaired t-tests with unequal variances were used to determine statistical differences. Differences were considered statistically significant at $p<0.05$.

Results

Myofibroblast transduction

More than 50% of MFBs were transduced at all the tested MOI (Figure 6A). By using a plate reader to quantitatively measure fluorescence, we found a statistically

significant increase in fluorescence between 1000 and 2000 MOI (28%, p=0.02), while we were unable to detect a significant increase between 2000 and 5000 MOI (Figure 6B). Hence, we chose to use 2000 MOI in our experiments.

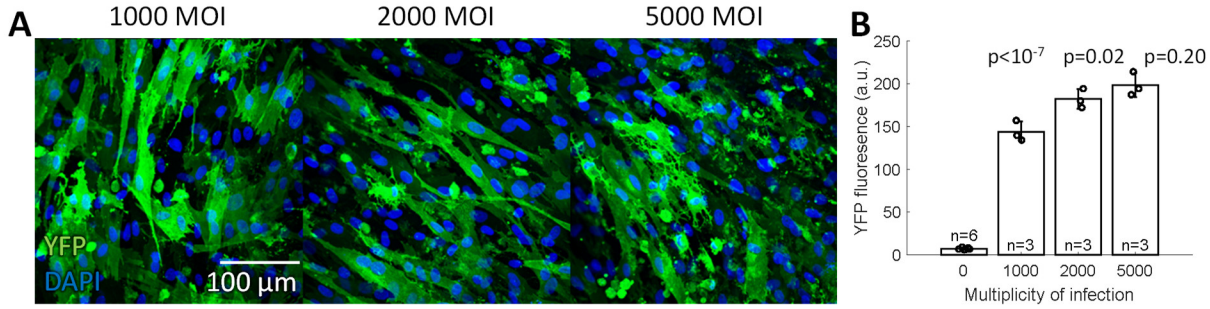

Figure 6. Transduction of myofibroblasts with ChR2.
A. Confocal images of MFBs transduced with varying multiplicity of infection (MOI) of ChR2 adenovirus. Green shows YFP, which marks cells transduced with ChR2, and blue shows DAPI, showing cell nuclei. Higher doses of virus were associated with some cell death (rounded cells). All images were taken at the same scale and settings. **B.** YFP fluorescence increased in a dose-dependent manner following transduction.

Co-culture of cardiomyocytes and ChR2-transduced myofibroblasts

Next, we co-cultured our MFBs with CMs. Because we wanted to limit direct TGF-β1 effects on CMs, we chose to not add TGF-β1 during co-culture. Confocal imaging of MFBs with CMs demonstrated continued expression of α-SMA by MFBs 2 days after plating on CMs and concomitant cessation of TGF-β1 treatment (Figure 7A-C). By imaging a wide field (~2 mm) of the co-culture, we found that the plated ChR2-MFBs formed a homogeneous, dense network over a wide area of CMs (Figure 7D). We also found continued expression of ChR2, as shown by fluorescence imaging of the YFP reporter (Figure 7E). Confocal imaging showed confluent CMs (Figure 7F) with ChR2-MFBs resting on top of them (Figure 7G and H). We found Cx43 puncta in the MFB cell layer, suggesting expression of Cx43 by MFBs (Figure 7G).

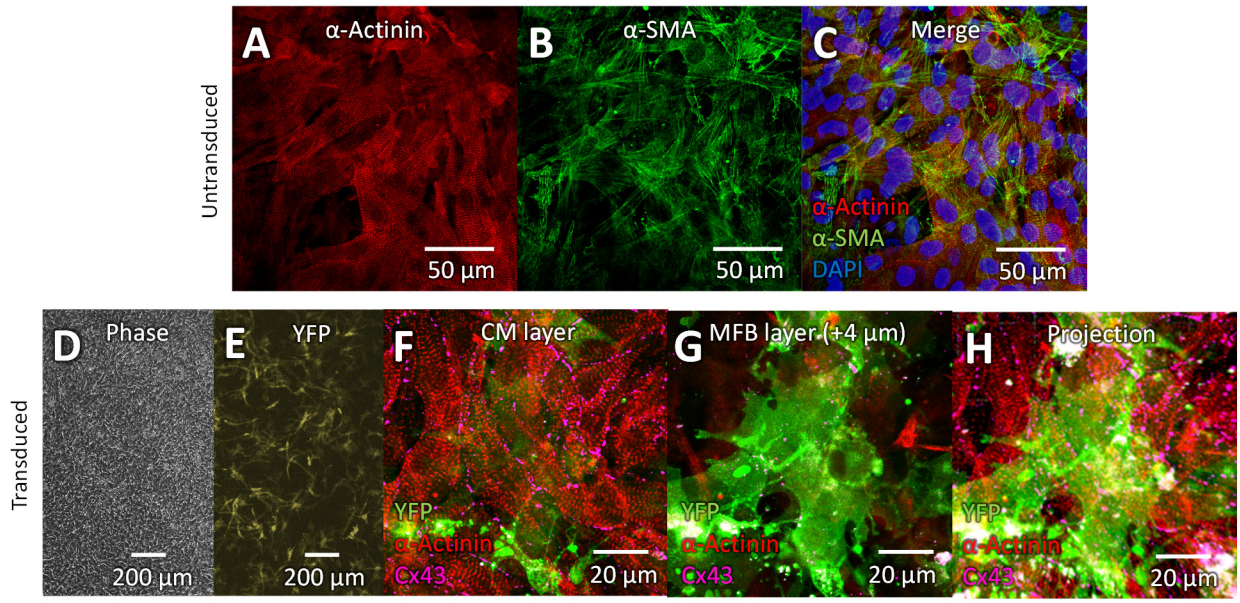

Figure 7. Co-culture of cardiomyocytes and ChR2-transduced myofibroblasts.
A-C. Confocal image of co-cultures of MFBs and CMs. Alpha-actinin (**A**, red) marks CMs, and smooth muscle actin (**B**, green) marks MFBs. **C.** Merge of **A** and **B** with DAPI (blue) to stain nuclei. **D.** Phase contrast image of CM co-cultured with ChR2-transduced MFB. **E.** Fluorescence image of same sample as D, with YFP marking transduced MFBs. **F-H.** Confocal image of transduced MFBs and CMs. YFP (green) marks transduced MFBs, alpha-actinin (red) marks CMs, and violet shows Cx43. **F.** CM layer of Z-stack showing gap junctions between CMs. **G.** Image from 4 µm above **F** showing MFB on top of CMs, as well as Cx43 puncta, apparently between CMs and MFBs. **H.** Maximum intensity projection of entire 18 µm-thick z-stack sampled every 2 µm.

Simultaneous optical mapping and voltage recording

Because our lab has significant experience using green LEDs in tandem with di-4-ANEPPS to measure optical signals, we wanted to see if this would be possible without significantly exciting ChR2. To do so, we measured both the power and the spectra of our stimulation LEDs, to determine the amount of effective light cells would receive from the LED used to excite the dye (Figure 8). Based on the computational model for ChR2 [132], we wanted the effective brightness to be below 0.003 mW/mm^2, to limit the ChR2 current due to the dye excitation light to less than 0.1 pA/pF (Figure 9), since that would be only ~10% of the baseline MF current at rest (Figure 3) and

modelling showed that level of brightness had basically no effect on CM electrophysiology (Figure 20). We found significant overlap between the green LED and ChR2 response that resulted in an effective brightness of 0.018 mW/mm^2 (Figure 8, Table 8), making it clear we would need to use a different dye for these experiments to prevent optical cross-talk. We chose di-4-ANBDQBS, based off the published redshifted excitation [137] (Figure 10), and tested the spectral efficiency of red light off-target excitation of ChR2 (Figure 8). We found very little overlap, and an effective brightness of 0.0021 mW/mm^2, which could be improved to $6.1x10^{-4}$ mW/mm^2 when we added a bandpass filter to it (Table 8). Because the light met our design specifications without the filter, we did not use the filter in our final iteration. Finally, we tested the blue LED to ensure it could efficiently stimulate ChR2 (Figure 8), which it could with 74% efficiency (Table 8).

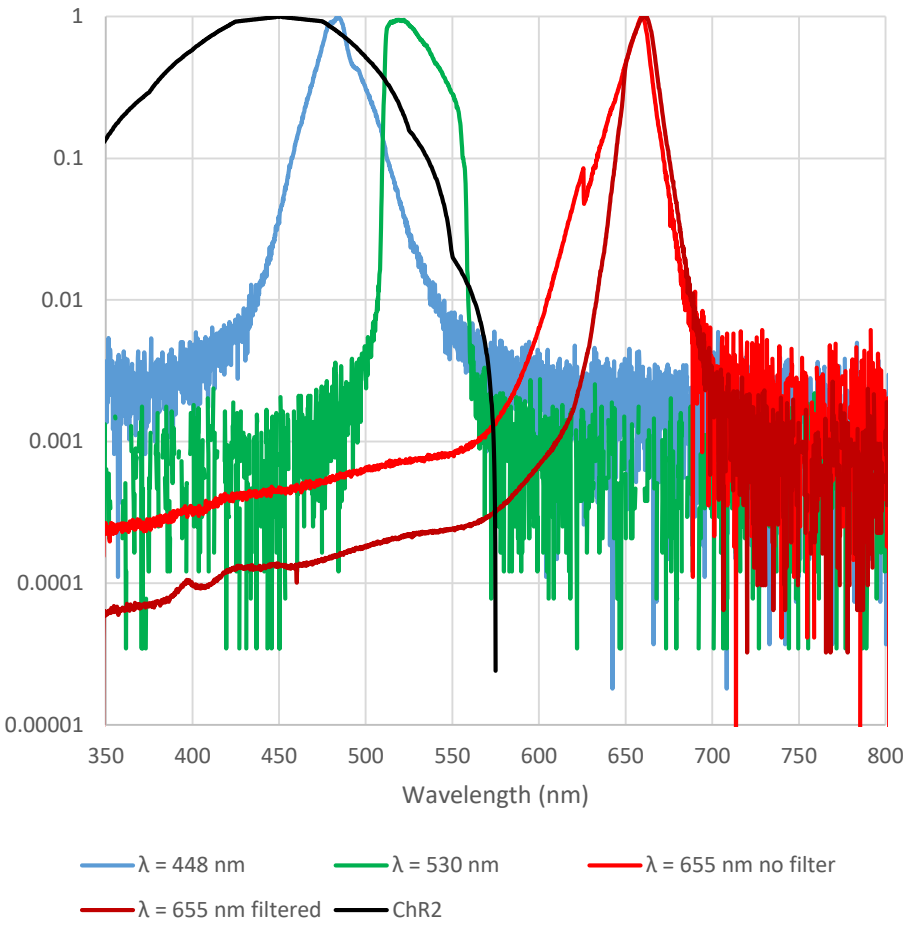

Figure 8. LED spectra versus ChR-2 responsiveness.
ChR2 is relative current for a given wavelength, other lines are spectral intensity for LEDs of different wavelengths.

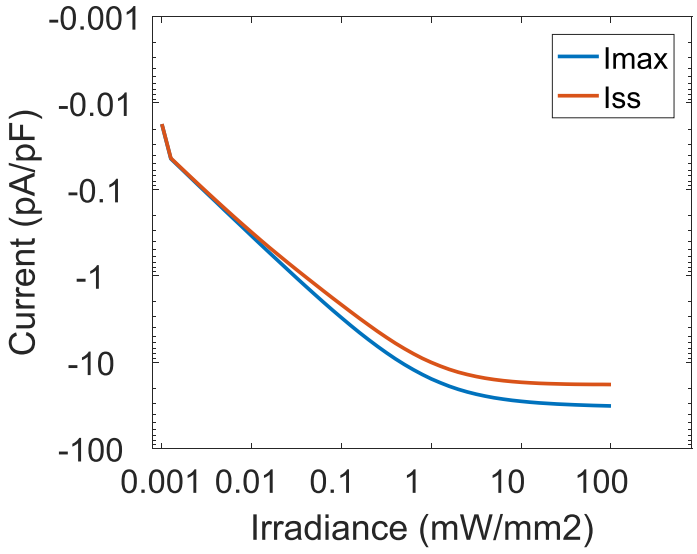

Figure 9. Current vs. brightness for modelled ChR2.
Holding potential of -80 mV. Imax is peak current (blue), and Iss is steady-state current (orange).

Color (wavelength)	Brightness (mW/mm^2)	Efficiency	Effective brightness (mW/mm^2)
Blue (448 nm)	0.001-0.1	0.74	0.00074-0.074
Green (530 nm)	0.07	0.26	0.018
Red with filter (655 nm)	0.8	0.00077	0.00061
Red no filter (655 nm)	0.8	.0026	0.0021

Table 8. Effective ChR2 stimulation by different wavelength LEDs.
Blue light brightness could be varied across a wide range to generate varying amounts of ChR2 current. Red and green LED brightness were set so that they delivered maximal light intensity without saturating the recording photodiodes, then intensity was measured in the sample chamber. Efficiency was calculated as described in the methods.

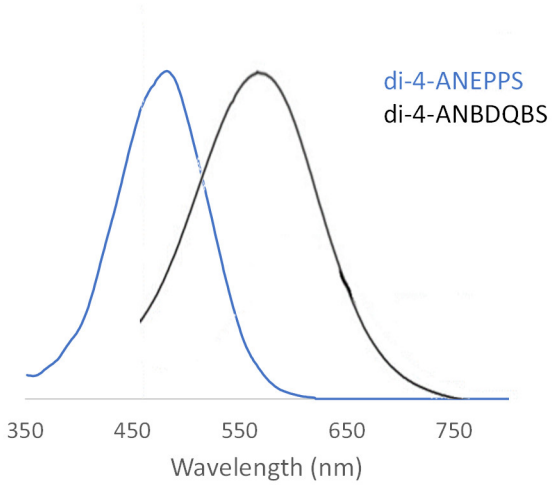

Figure 10. Excitation spectra of di-4-ANEPPS and di-4-ANBDQBS.
Based off data from [138] and [137], respectively.

Having found and characterized the proper LEDs for our study, we moved on to testing the di-4-ANBDQBS on cardiac monolayers. Initially, no voltage-dependent signal could be detected, despite proper dye fluorescence visible in confocal microscopic images (Figure 11). To determine why this occurred, we first tested the spectral filtering of our emission filter. To this we measured the intensity of the red LED with and without two different emission filters. We found that while the 715 nm filter allowed 1/5,000 of the light through, the 760 nm filter only allowed about 1/50,000 of the light through (Figure 12). In both cases, about half of the bleed-through was due to insufficient block where the LED was brightest (655 nm), and about half was due to some of the LED light having a wavelength long enough to be in the pass band.

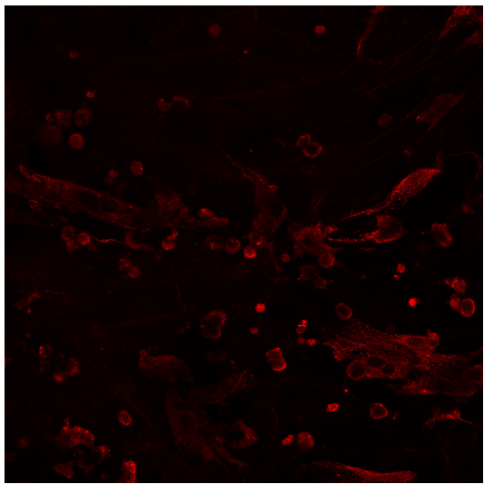

Figure 11. Confocal imaging of cardiomyocytes stained with di-4-ANBDQBS.

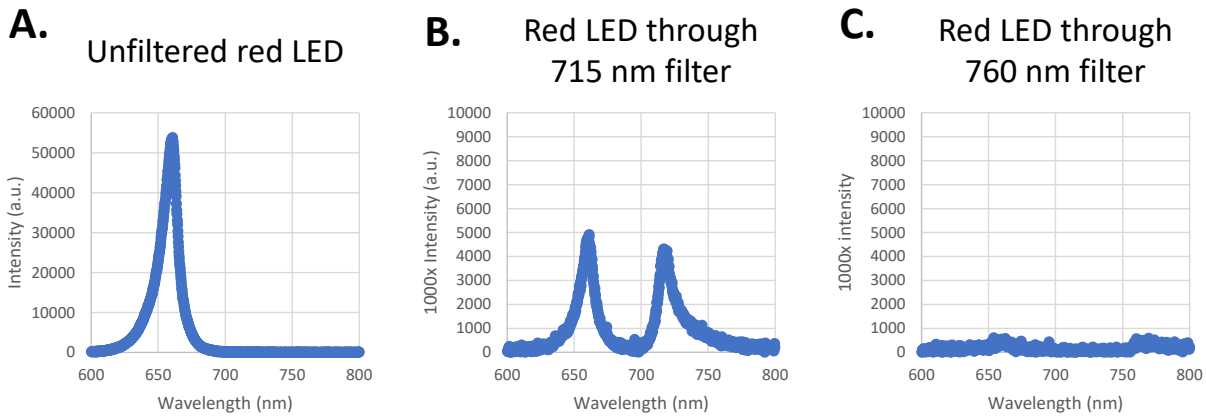

Figure 12. Quantifying optical bleedthrough.
Optical bleedthrough was tested by measuring the unfiltered light intensity and spectrum of the red excitation LED (**A**), then measuring the spectrum after placing a 715 nm (**B**) or 760 nm (**C**) filter between the LED and spectrometer. The exposure time for the filtered spectra had to be increased by a factor of 1000 to gather enough light to make a precise measurement.

Despite the high optical density of the 760 nm filter, we were still unable to record any voltage-sensitive signal. Therefore we compared the quantum yield of di-4-ANBDQBS to that of di-4-ANEPPS, which we knew could produce signal in our system. At the typical dye concentrations used for optical mapping, the plate reader we used could not detect the fluorescence of either dye, but we were able to detect it by

increasing the concentrations. When exciting at 582 nm, the previously found peak excitation wavelength for di-4-ANBDQBS ([137], Figure 10), we found that di-4-ANBDQBS fluorescence peaked near 800 nm as expected, but that its fluorescence intensity was almost a factor of 10 lower than that of di-4-ANEPPS under the same conditions (Figure 13), despite the excitation wavelength being 100 nm longer than the peak wavelength to excite di-4-ANEPPS (470 nm, [139]), resulting in less than 5% of di-4-ANEPPS maximal fluorescence (Figure 10). At 655 nm, the wavelength we were using to maximally excite the voltage response of di-4-ANBDQBS, the fluorescence decreased by over half again, relative to that at 582 nm. The low quantum yield of di-4-ANBDQBS suggested that the reason we could not record voltage signals was because of insufficient emission filtering, despite our already powerful filters (See p.58 for discussion). Therefore, in our final iteration we used two stacked 717 nm long-pass Wratten absorptive filters (see p.58 for discussion).

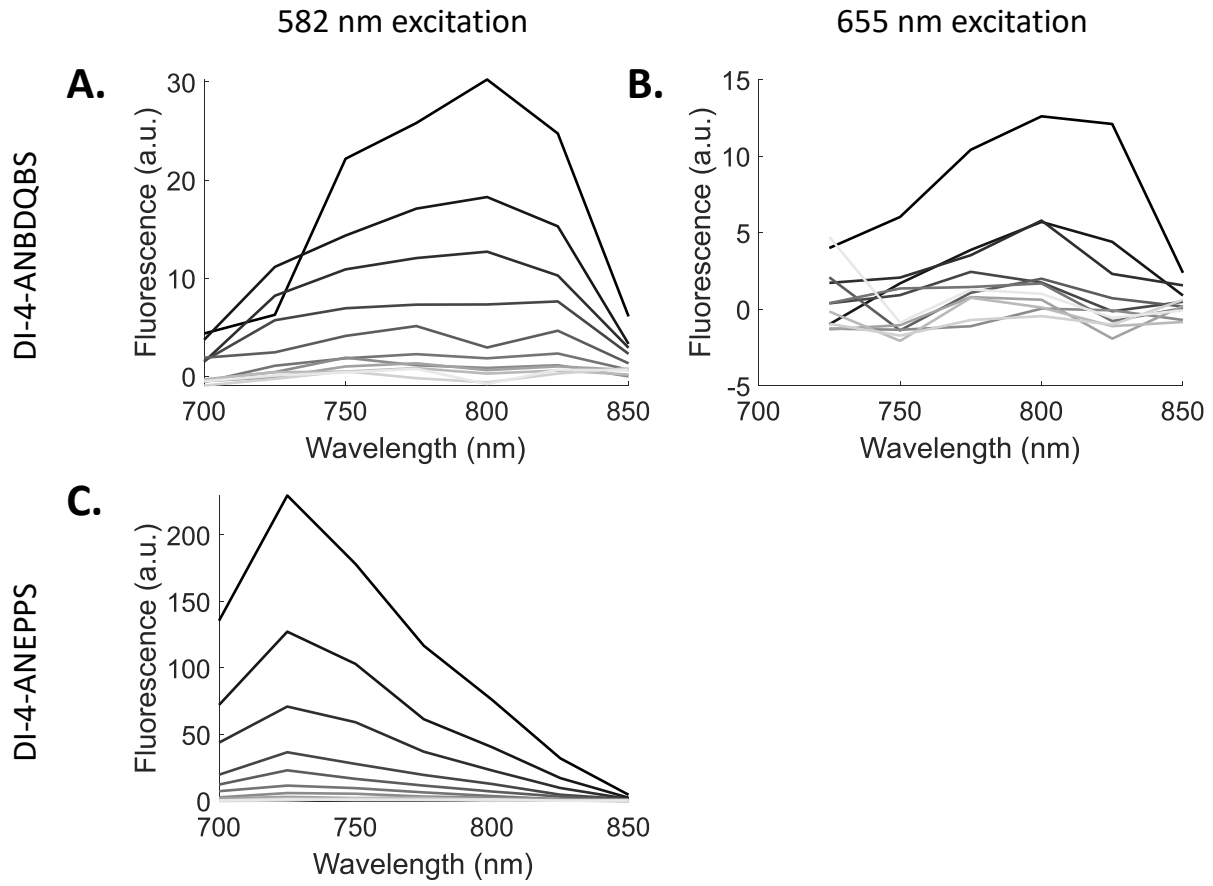

Figure 13. Fluorescence intensity of voltage-sensitive dyes.
Fluorescence intensity of di-4-ANBDQBS (**A,B**), was compared to that of di-4-ANEPPS (**C**) at different wavelengths and concentrations, from 8.75 μM to 17.5 mM for di-4-ANBDQBS, and from 1μM to 2 mM for di-4-ANBDQBS. Lighter lines show lower concentrations of dye, heavier show higher, by factors of 2. Fluorescence monotonically increased with dye concentration. di-4-ANBDQBS was tested at its peak excitation wavelength of 582 nm (**A**), as well as at its most voltage-sensitive wavelength of 655 nm (**B**). di-4-ANEPPS was tested at 582 nm, about 100 nm longer than its peak excitation wavelength of 470 nm, for comparison (**C**).

Myofibroblast currents can cause electrophysiological changes in cardiomyocytes

To assess whether inward current in MFBs can affect CM electrophysiology, we recorded CM optical voltage signals in the absence or presence of blue light. We found that in ChR2-MFB/CM co-cultures paced at 2 Hz (Figure 14Ai), application of continuous blue light to open ChR2 channels (Figure 14Aii) could immediately induce ectopic beating at a rate higher than the 2 Hz paced rate. Cessation of light (and

therefore ChR2 current) caused ectopic beating to immediately stop (within seconds, Figure 14Aiii). Data across multiple monolayers showed that the ectopic cycle length decreased as the ChR2 current increased (Figure 14B). This dose-dependent ectopic beating occurred in almost all ChR2-MFB/CM co-cultures, but in none of the MFB/CM co-cultures (Figure 14B). The cycle length (CL) of ChR2-MFB/CM co-cultures under 0.057 mW/mm^2 light was significantly less than that without light, which was always at the paced 500 ms CL (338±99 vs. 500±1 ms, n=7, $p<10^{-4}$, Figure 14B).

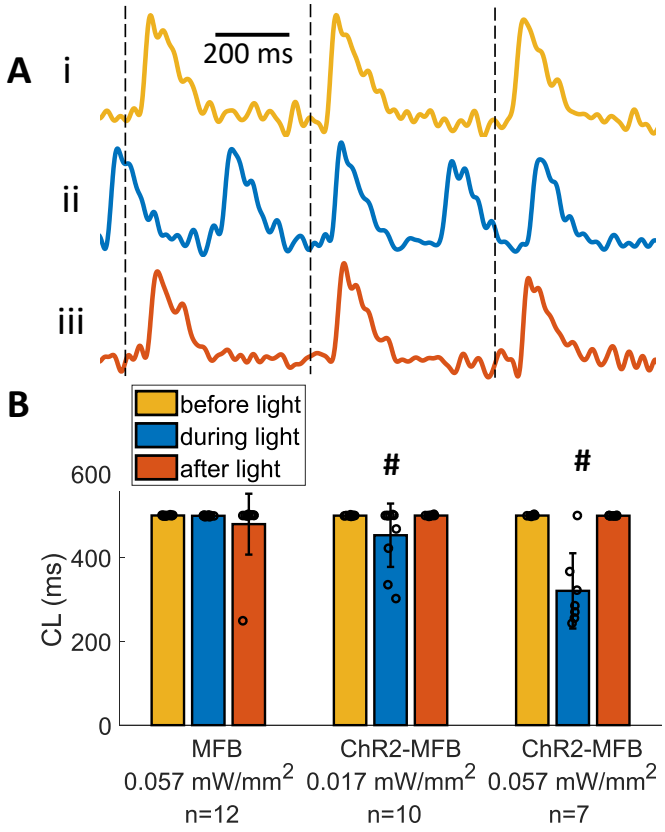

Figure 14. Inward currents in myofibroblasts cause spontaneous beating in co-cultured cardiomyocyte syncytia.
A. Voltage traces of a co-culture of ChR2-transduced MFB with CMs before (I, gold), during (ii, blue), and after (iii, orange) application of 0.017 mW/mm^2 blue light to activate ChR2 current in MFB. Dashed lines show time of pacing. **B.** Cycle length before, during, and after application of light at different power during 2 Hz pacing, for co-cultures of CM with MFB or ChR2-transduced MFB. # shows $p<0.005$ before vs. during light application.

We also found that during 2 Hz pacing (Figure 15Ai), at light intensities less than those needed to cause ectopic beating, application of light immediately slowed CV of ChR2-MFB/CM co-cultures (Figure 15Aii). This slowing was immediately reversed when the light was turned off (Figure 15Aiii). CV decreased further as light intensity was increased, until the onset of spontaneous beating prevented further comparison of CV (since spontaneous beating will increase the beating rate, which on its own will slow CV) (Figure 15B). While the light intensity necessary to cause both detectable slowing and spontaneous beating varied somewhat between samples, slowing occurred specifically in ChR2-MFB/CM co-cultures in a dose-dependent manner across multiple samples (Figure 15B). There was significant slowing in ChR2-MFB/CM co-cultures at light levels as low as 0.006 mW/mm^2 ($p=0.03$), and slowing was even more significant at 0.017 mW/mm^2 (-3.7±1.8 cm/s, $p=0.005$, Figure 15B). The maximum slowing before induction of spontaneous beating was 6.6 cm/s.

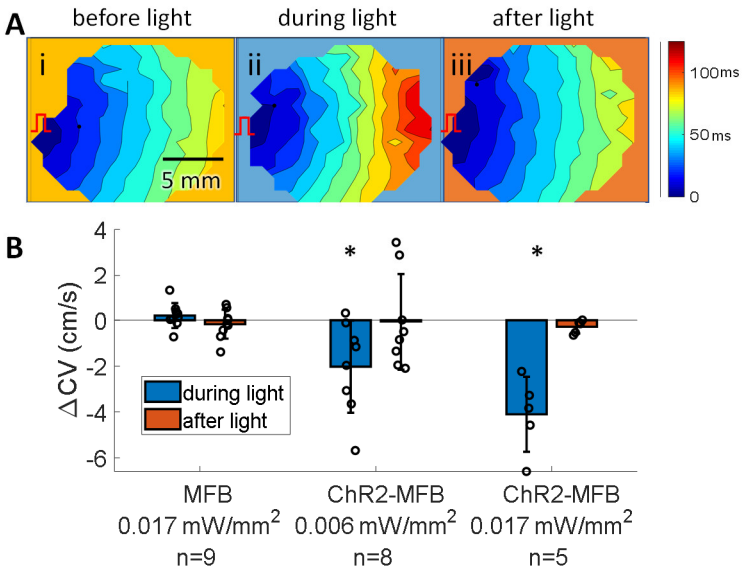

Figure 15. Inward currents in myofibroblasts cause slowing in co-cultured cardiomyocyte syncytia.
A. Activation maps of a co-culture of ChR2-transduced MFB with CMs before (I, gold background), during (ii, blue background), and after (iii, orange background) application of 0.017 mW/mm^2 blue light to activate ChR2 current in MFB. Color bar at right shows activation time scale. Isochrones are 10 ms apart. Red pacing marker illustrates location of pacing. **B.** Change in CV (vs. before light application) during and after application of light at different power during 2 Hz pacing, for co-cultures of CM with MFB or with ChR2-transduced MFB. * shows $p<0.05$ difference in before vs. during light application.

Finally, we found that light-induced inward current decreased APD_{80}, which also immediately reversed upon removal of light (Figure 16A). Looking over multiple monolayers, we found a dose-dependent response with a statistically significant decrease in APD_{80} at a light intensity of 0.017 mW/mm^2 in ChR2-MFB/CM co-cultures (-23±14 ms, p=0.02, Figure 16B). P-values for these parameters calculated using other methods are provided in Table 9.

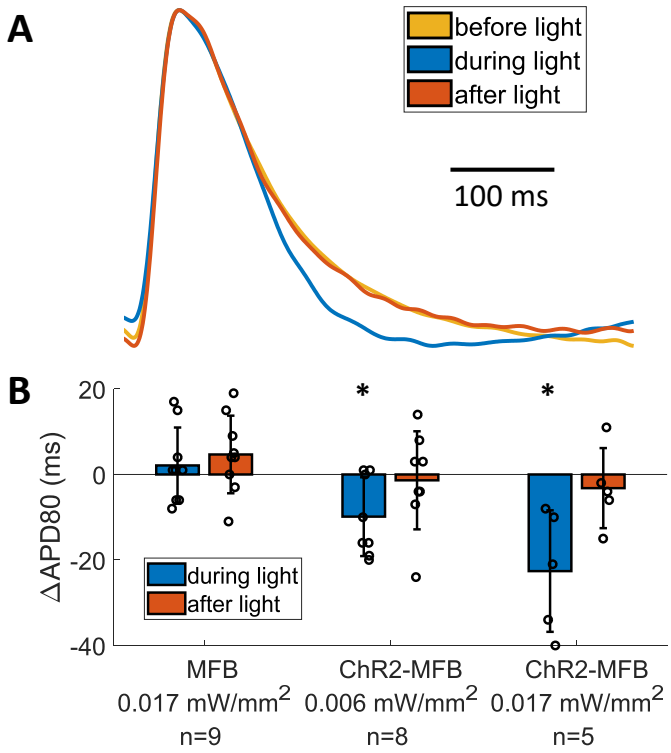

Figure 16. Inward currents in myofibroblasts change action potential morphology in co-cultured cardiomyocyte syncytia.
A. AP traces averaged over 2 s recording over the entire monolayer before (gold), during (blue), and after (orange) application of 0.017 mW/mm^2 blue light to activate ChR2 current in MFB. **B.** Change in APD_{80} (vs. before light application) during and after application of light at different power during 2 Hz pacing, for co-cultures of CM with MFB or ChR2-transduced MFB. * shows $p<0.05$ difference in before vs. during light application.

		Paired P ($\Delta_{light\ on}$)		Paired P ($\Delta_{light\ off}$)		$\Delta_{light\ on}$ P(ChR2 vs. no ChR2)		95% CI of during light (CL) or after light-before light			
		Low	High	Low	High	Low	High	Low		High	
MF	CL	$<10^{-7}$	$<10^{-4}$	$<10^{-21}$	$<10^{-18}$	0.079	0.002	499	501	499	500
	CV	0.025	0.005	0.013	0.009	0.017	0.003	-1.8	1.7	-0.6	0.07
	APD80	0.019	0.024	0.078	0.007	0.895	0.013	-11	8	-15	8
CF	CL	$<10^{-5}$	$<10^{-3}$	$<10^{-24}$	0.171	0.004	$<10^{-3}$	500	500	149	635
	CV	0.036	N/A	0.123	N/A	0.055	N/A	-0.9	-0.2	N/A	N/A
	APD80	0.013	N/A	0.124	N/A	0.764	N/A	-11	12	N/A	N/A

Table 9. Additional p-values and confidence intervals.
For measured parameters for low (0.017 mW/mm^2 for CL, and 0.006 mW/mm^2 for others) and high (0.057 mW/mm^2 for CL and 0.017 mW/mm^2 for others) light levels for CFB and MFB. $p<0.05$ shaded.

Acute force measurements exclude acute mechanical effects

To exclude the possibility that inward currents in MFBs caused them to contract and potentially influence CMs by activating mechanosensitive channels, we seeded ChR2-MFBs on micropost arrays and were unable to detect changes in strain energy during application of light (Figure 17).

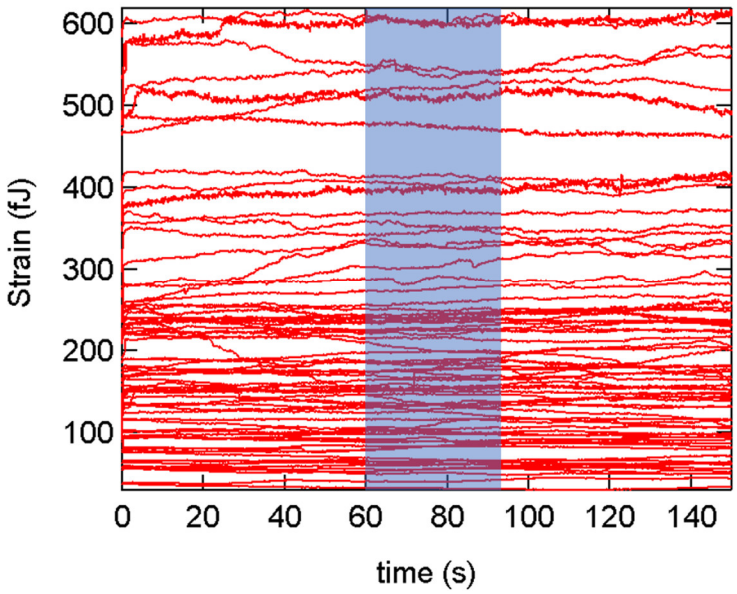

Figure 17. Acute strain energy response to light in ChR2-transduced myofibroblasts. Recordings of ChR2-MFB strain energy before, during (blue box), and after excitation. Near-saturating 1.1 mW/mm^2 blue light shows that opening of ChR2 channels does not acutely affect contractile strain energy. Each trace shows a different MFB. Data from Yu Shi.

Mathematical model optimization

Our optimization resulted in a more optimized waveform (Figure 18A) that could spontaneously beat at a higher rate (Figure 18B). To reduce the number of parameters that needed to be changed, a sensitivity analysis was performed, showing the improved score was the result of changing only 6 variables (Figure 18C). The remaining variables were reset, and the model was again run, using the optimal parameters of the first run as a starting point. By continuing to iterate in this fashion, the final model was developed, which only required changing 4 variables in order to produce more spontaneous beating, all of which were empirically defined in the original model: L-type calcium channel calcium gating was changed to $\alpha_{fCa} = \left[1 + \left(\frac{[Ca^{2+}]_{subSL}}{0.718}\right)^{8}\right]^{-1}$ (See Table 5), the calcium diffusion time constant between the uptake and release compartments of

the SR was decreased to 92 ms, and the I_{Ks} and I_{Kr} conductances, determined in the Korhonen model based on their effect on APD, were changed to 0.11 mS/μF and 0.03 mS/μF, respectively, to facilitate spontaneous beating (See Table 6). While I_{Ks} and I_{Kr} conductances are difficult to measure [131], the ratio between them of ~3.7 is more similar to the ratio of ~2.5 found previously in cultured neonatal rat CMs [140] than the ~0.8 in the original model.

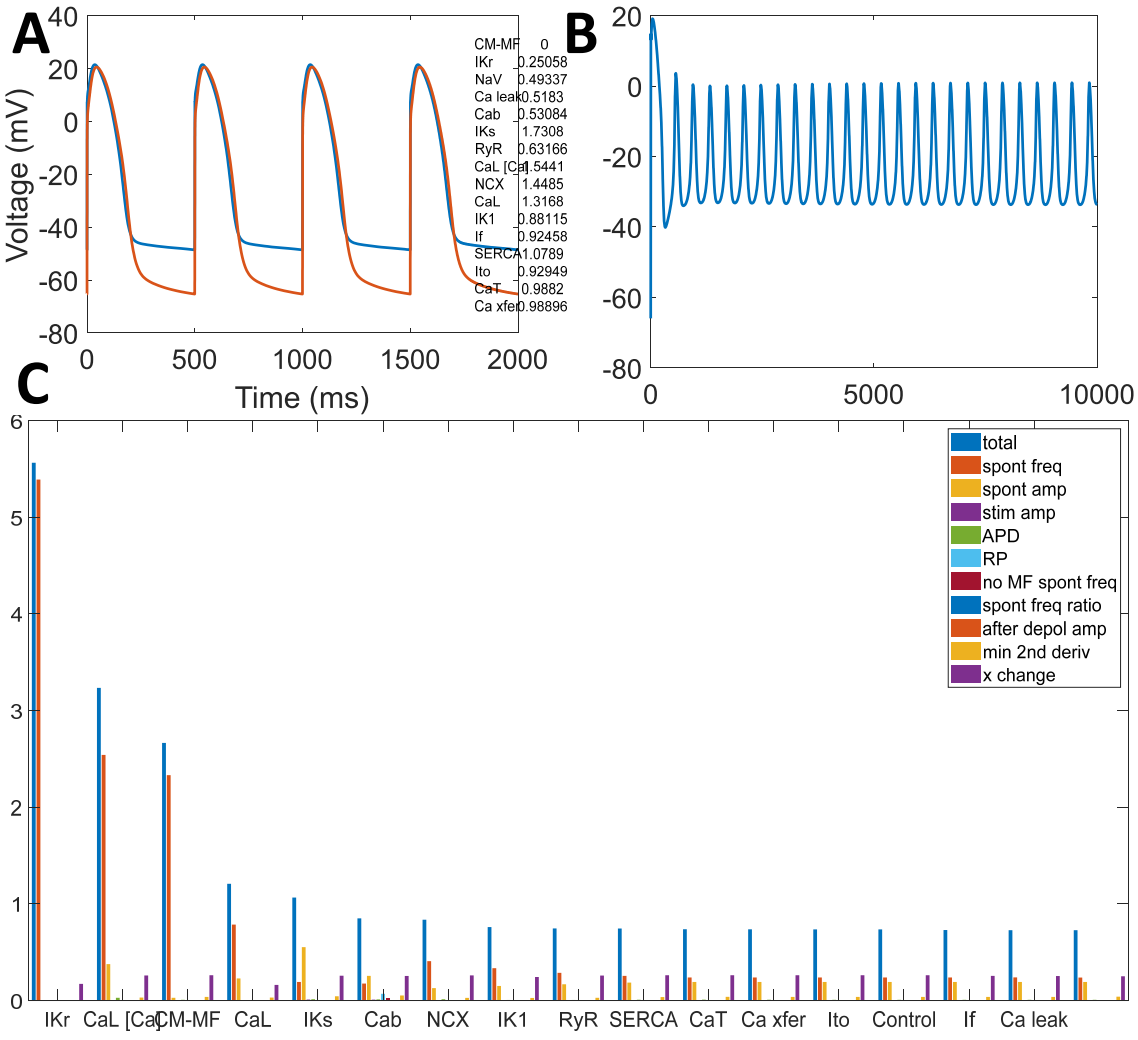

Figure 18. Initial model optimization and sensitivity analysis.
A. Waveform of wave optimized for spontaneous beating. Orange trace is original model, blue trace is optimized model. Numbers on right are ratios of how much each parameter was changed, sorted from most to least changed. **B.** Trace of optimized model in ChR2-MFB co-culture with 1 mW/mm^2 light shows spontaneous beating. **C.** Sensitivity analysis showing the effect of individually resetting each changed parameter to its initial value on each component of the score.

In addition to these changes, I_{Na} conductance was increased to 150 mS/µF to match the CV found in control monolayers (18±7 cm/s, see Table 6). In the original model, it was chosen to result in the correct AP amplitude, but changes to I_{Na} conductance within a wide range had little effect on AP amplitude, and the final model

had an amplitude at 2 Hz pacing of 86.7 mV compared to 85.9 mV in the original (Figure 19A). Furthermore, APD_{80} at 2 Hz pacing was only slightly affected in the final model, decreasing from 214 ms to 184 ms (Figure 19A), which better matches our experimentally measured APD_{80} of 187±39 ms in control monolayers. These changes resulted in a maximum spontaneous beating rate of 2.8 Hz, instead of 0.6 Hz (G_{MFBCM}=1 μS, light intensity=1 mW/mm^2, see Figure 19B), and also increased the maximum capture rate from 2.5 Hz to 3.5 Hz (I_{stim}=-80 pA/pF, 0.5 ms), both of which are closer to values found experimentally (6 Hz and ~7 Hz).

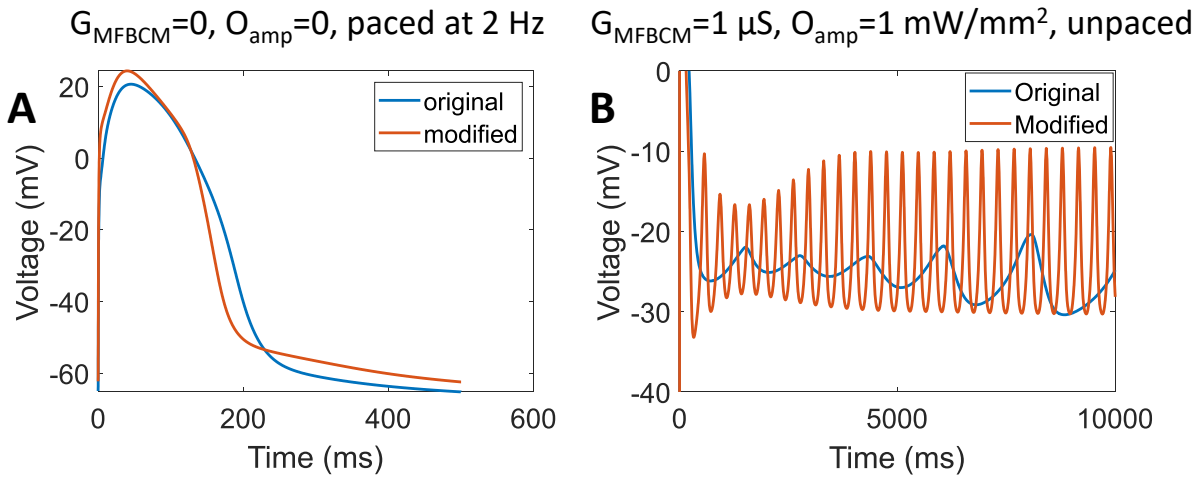

Figure 19. Computational model.
A. Voltage traces from original (blue) and modified (orange) Korhonen model [131] paced at 2 Hz. **B.** Voltage traces from spontaneous beating of original (blue) and modified (orange) CMs connected to ChR2-MFBs and high light intensity (G_{MFBCM}=1 μS, light intensity=1 mW/mm^2).

Mathematical modeling results

Our linear cable model of ChR2-MFBs electrically coupled to CMs (Figure 4) demonstrated similar behavior to our experiments, with increasing spontaneous beating in response to increased increasing light with sufficient G_{MFBCM}, surpassing our 2 Hz paced rate at high light levels and high G_{MFBCM}, as well as reduced CV in response to

light over a range of G_{MFBCM} (Figure 20). Analysis of CV across a wide range of G_{MFBCM} and light intensities showed that if $G_{MFBCM}$is low, inward currents from light application have very little effect on CMs, since this current cannot pass to CMs. Conversely, if it is too high, it does not cause much additional slowing (Figure 20B).

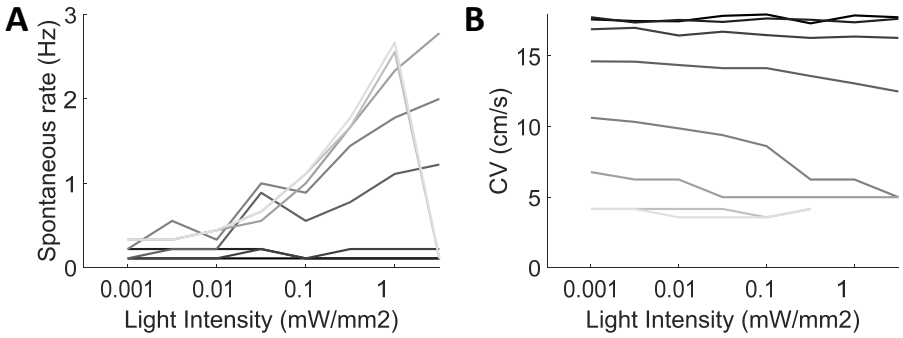

Figure 20. Modeling verifies experimental findings.
MFB-CM coupling varies by half-log10 increments from $10^{-4.5}$ µS (dark) to 10^{-1} µS (light).) **A.** Spontaneous beating rate for CMs at different MFB-CM coupling and light intensities. **B.** CV for CMs at different amounts of MFB-CM coupling and light intensities.

The model also showed that increased MFB-CM conductivity or light intensity shortened normalized APs and decreased APD_{80} as found experimentally (Figure 21A). This occurs because although the maximal repolarization rate is decreased, the AP amplitude is decreased more (Figure 21B), resulting in a decreased APD_{80}, as can be seen in the normalized traces (Figure 21C), which is how experimental data is analyzed.

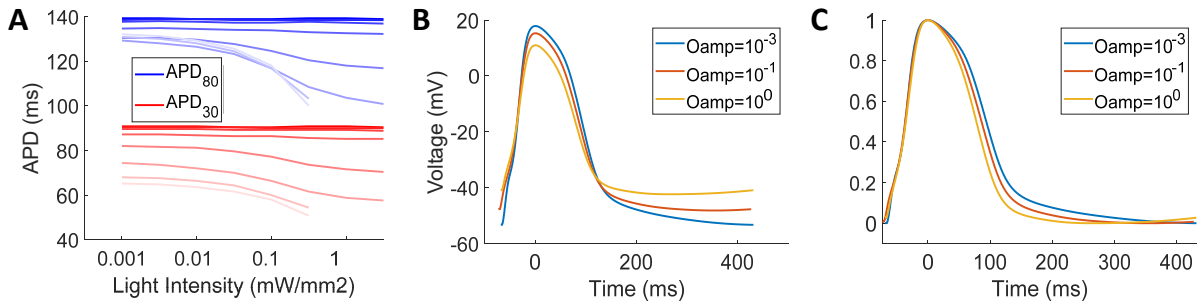

Figure 21. Modeling explains why light-induced current reduces action potential duration. **A.** Effect of cell coupling and light intensity on APD_{80} (blue) and APD_{30} (red). **B.** AP traces for selected light intensities (Oamp), in mW/mm^2, with $G_{MFBCM} = 0.01\ \mu S/CM$ **C.** Normalized AP traces for selected parameters, as would be seen during optical mapping.

Discussion

Comparison with previous work

Since the initial findings of Miragoli that addition of MFB to CM cultures causes RP elevation, conduction slowing, and spontaneous beating [55], a number of studies have attributed MFB-induced conduction slowing to electrical coupling between CMs and MFBs [35, 55, 62–64, 66]. Dual-cell patch clamp has been used to quantify the electrical connection between CM and MFB pairs [35, 76], but the conductance values provided by patch clamp studies are normalized to the length of the cell interface [35], and it is unlikely this can be simply be multiplied by the interface height to be translated to interfacial area for use in 3-D tissues. To more closely mimic a 3-D environment, in which there can be large areas of interaction between MFB and CMs without the MFBs physically blocking CM propagation, we seeded MFBs on top of our CM monolayers rather than seeding them simultaneously as a mixed population prior to monolayer formation.

Interventional experiments have knocked down Cx43 in MFBs [64, 68], and found that doing so increased CV in co-cultures, compared to CMs co-cultured with MFBs alone, suggesting an electrical mechanism for slowing by MFBs. However, a different study reported that MFBs with knocked-down Cx43 slowed CM conduction just as much as control MFBs [61]. Different results from this approach may stem from two potentially offsetting side effects. The first is that decreasing Cx43 expression inhibits TGF-β signaling [83] and CFB differentiation to MFB [83, 84], so that Cx43 knockdown alone could reduce the number of MFBs present, increasing CV independent of CM-CFB/MFB electrical connections. The second is that the interfering RNA used in these studies to knock down Cx43 can be transferred between cells [141], so that CV could slow due to off-target knockdown of Cx43 between CMs, increasing CV independent of CM-CFB/MFB electrical connections. The second is that the interfering RNA used in these studies to knock down Cx43 can be transferred between cells [141], so that CV could slow due to off-target knockdown of Cx43 between CMs.

Studies that acutely change MFB electrophysiology and monitor the subsequent changes in CM electrophysiology circumvent these limitations. A few previous studies have used this strategy. One seeded clusters of 3T3 fibroblasts transduced with Kv1.3, a potassium channel not found in cardiac cells, onto NRVMs, and then showed that a blocker specific to that channel reduced conduction block [142]. Another transduced 3T3 fibroblasts with Kv1.3 and found that they decreased spontaneous beating rate of NRVMs with which they were co-cultured, and decreased the refractory period of rat and pig hearts to which they were grafted; and that these effects could be reversed by blocking Kv1.3 [143]. Finally, Nussinovitch, et. al. used ChR2-transduced 3T3

fibroblasts to pace NRVMs in culture [10]. However, 3T3 fibroblasts are an immortal cell line with many chromosomal abnormalities [144], and not a good model of either fibroblasts or myofibroblasts, let alone CFBs or MFBs. Another study used sphingosine-1-phosphate to acutely modulate MFB RP, and found that it suppressed CM excitability in co-cultures with MFBs, but not CMs alone [77]. In our study, we applied light to produce an inward current in ChR2-MFBs and found that MFBs and CMs are sufficiently well connected electrically for this connection to produce ectopic beating (Figure 14) and conduction slowing (Figure 15) within seconds. The rapid time scale in which CV changes were observed (within seconds) eliminates the possibility that changes in cardiac ion channel expression in response to the presence of MFBs underlie the slowing effects. Additionally, the absence of changes in force generation with application of light to ChR2-MFBs (Figure 17) makes it unlikely that CV slowing occurs secondary to acute MFB contraction. The fact that light effects were quickly reversible within seconds (Figure 14E and Figure 15E) and had no effect on control MFB/CM co-cultures (Figure 14F-G and Figure 15F-G) also support the notion that the effects were due to light-induced ChR2 currents and not to off-target effects such as heating or photochemical reactions, or changes in gene expression.

Quinn et al. [145] argued for electrical connections between MFBs and CMs *in vivo* by creating genetically engineered mice that expressed an optogenetic voltage sensor specifically in non-myocytes, and found APs present specifically near cryoinjury, suggesting that non-myocytes can electrically connect to CMs in areas of injury. However, whether the promoter they used is truly selective for non-myocytes is unclear [146]. Furthermore, lower currents in non-myocytes could allow for even marginal

electrical connectivity to be recorded, since nonmyocytes have high sarcolemmal resistance, and are excellent voltage followers, as discussed in [126]. Furthermore, optogenetic sensing cannot demonstrate whether non-myocytes are sufficiently coupled to CMs for their currents to cause conductance slowing or spontaneous beating. While the lack of a confirmed promoter active in MFBs, but not in CMs remains a challenge, the current study suggests that using a similar design with an optogenetic actuator could verify whether MFBs are sufficiently connected to CMs to cause conduction slowing and spontaneous beating *in vivo* under conditions of activated, inward MFB current.

Because our study allowed us to specifically modulate inward currents of the MFB, it showed experimentally that inward currents from MFBs are a sufficient mechanism to cause slowing in electrically coupled CM-MFBs. Whether other proposed mechanisms, such as the MFB being a current sink during CM depolarization due to MFB outward currents and capacitance, remains to be explored. Additionally, paracrine and mechanical effects of MFB may also contribute to slowing.

Simultaneous optical mapping and voltage recording design

Despite di-4-ANBDQBS having better voltage sensitivity than di-4-ANEPPS [137], we found that it has a significantly lower quantum yield (Figure 13). Low quantum yield isn't a problem for most optical mapping systems because they use epi-illumination, in which very little of the excitation light is reflected directly back to the fluorescence detector, and what little is reflected is further reduced by the dichroic mirror. However, our system uses transillumination, in which the excitation light shines directly onto the fluorescence detector, which means there can be significant bleed-

through of the excitation light without excellent filtering. The signal (μ) of an optical mapping system at a given wavelength and voltage change can be written mathematically as $\mu = \mu_{ex} Q d_{em} \Delta Q_v$, where μ_{ex} is excitation light intensity, Q is quantum yield of the dye, d_{em} is the fraction of emission light directed to the detector, and ΔQ_v is the relative change in quantum yield for a given change in voltage. Total noise (σ) is the root-mean-square of all the noise sources, $\sigma = \sqrt{\sum N}$. For voltage mapping systems, the detected noise due to excitation light noise (N_{ex}) is $N_{ex} = d_{ex} m \sigma_{ex}$, where d_{ex} is the fraction of excitation light that is directed to the detector, m is the fraction of excitation light that passes through the emission filter (and dichroic if present), and σ_{ex} is the fractional temporal noise in the excitation light. The detected noise due to emission light (N_{em}) is $N_{em} = Q d_{em} \sigma_{ex}$. Finally N_o is a lumped term for other sources of noise not considered in this discussion. Therefore, total noise is

$\sigma = \sqrt{(d_{ex} m \sigma_{ex})^2 + (Q d_{em} \sigma_{ex})^2 + {N_o}^2}$, and signal-to-noise ratio is

$\frac{\mu}{\sigma} = \frac{\mu_{ex} Q d_{em} \Delta Q_v}{\sqrt{(d_{ex} m \sigma_{ex})^2 + (Q d_{em} \sigma_{ex})^2 + {N_o}^2}}$. Rearranging the equation for σ, if

$Q \gg \sqrt{\frac{(d_{ex} m \sigma_{ex})^2 + {N_o}^2}{(d_{em} \sigma_{ex})^2}} = \sqrt{\left(\frac{d_{ex}}{d_{em}} m\right)^2 + \left(\frac{N_o}{d_{em} \sigma_{ex}}\right)^2}$, the other terms of the denominator may be ignored. In epi-illumination, since $m < 1$, and the excitation light is pointed directly away from the detector and must pass through a dichroic mirror to reach it, making $d_{em} \gg d_{ex}$, the first term may be ignored and this equation simplifies to $Q \gg \frac{N_o}{I d_{em} N_{ex}}$. This is almost always the case, allowing us to neglect the other terms of the denominator, simplifying the equation to $\frac{\mu}{\sigma} = \frac{Q d_{em} \Delta Q_v}{Q d_{em} \sigma_{ex}}$, which further simplifies to $\frac{\mu}{\sigma} = \frac{\Delta Q_v}{\sigma_{ex}}$, illustrating why voltage sensitivity in these systems is so important to getting good

signal, while quantum yield is not. However, in transillumination, usually $d_{ex} \gg d_{em}$ since almost all the excitation light is directed towards the sensor, while the emission light is directed equally in all directions. Therefore, the first term in the denominator cannot be neglected and creates an additional source of noise, making both high Q and high ΔQ_v important to maintaining high signal-to-noise, as well as low noise in the excitation intensity, and excellent emission filtering. Based on our measured data (Figure 13), as well as the published excitation spectrum of di-4-ANEPPS (Figure 10), we can calculate the ratio of quantum yield between di-4-ANEPPS and di-4-ANBDQBS to be $\frac{Q_{di-4-ANEPPS}\,|\,peak}{Q_{di-4-ANBDQBS}\,|peak} = \frac{I_{di-4-ANEPPS}|\,582\,nm}{I_{di-4-ANBDQBS}\,|\,peak} \quad \frac{I_{di-4-ANEPPS}|\,peak}{I_{di-4-ANEPPS}|\,582\,nm} = \frac{230}{30} \quad \frac{1}{0.04} = 192$. The fact that Q is important in signal to noise, combined with this result showing di-4-ANEPPS had much higher Q than di-4-ANBDQBS (Figure 13), explains why our transillumination setup could have much better signal-to-noise when using di-4-ANEPPS, even with lower quality filters, as well as a tenth of the excitation light intensity (Figure 12). Furthermore, these equations explain why other systems that use epi-illumination have an increase in signal quality from using di-4-ANBDQBS (due to the higher ΔQ_v being an important determinant of signal-to-noise), while we saw a drastic decrease (due to the much lower Q being the main determinant of signal-to-noise).

Having chosen the dye, we set about minimizing the other contributors to noise. To decrease noise in the excitation light intensity, we placed a voltage regulator between our LED and the power supply. Improving our emission filter was more difficult, because the sample had to be in close apposition with the fiber optics since the emission light is not focused, meaning the emission filter needed to be thin (~1 mm). Such powerful yet thin interferential filters are rare and expensive, but we developed a

solution by stacking absorptive filters, which are more fragile due to being water-soluble, do not have as sharp a transition between transmission and blocking, and have lower optical density, but may be stacked to effectively add their optical densities. Since we didn't need a sharp transition, just good blocking in the stop-band, in our final iteration we stacked two 100 μm-thick 717 nm Wratten filters on a 1 mm-thick slide and covered them in 68 μm thick clear tape to protect them from the moisture in the chamber, and were able to successfully record APs, with a total distance between the sample and fiber optics of 1.27 mm.

Mathematical modeling insights

While previous models have suggested inward currents in MFBs can cause CM conduction slowing, most of them have focused on extrapolating *in vitro* data to *in vivo*, using models for guinea pig [53], canine [147], or human [43, 47, 148, 149] CMs, not modeling what is occurring *in vitro*. Only one previous work modelled MFBs co-cultured with CMs using a neonatal rat CM model [150], despite the vast majority of experiments to investigate effects of MFBs on CMs being conducted on neonatal rat CMs. That work simultaneously co-cultured CMs and MFBs, allowing the MFBs to interrupt CM-CM connections, and focused on how the resulting structural heterogeneity could produce wavebreaks and reentrant arrhythmia [150]. In this work we used a neonatal rat CM model as well as an MFB model parameterized directly from recent data from cultured MFBs [35] to model how MFs may affect cardiac tissue electrophysiology without disrupting CM-CM connections.

Although MFB-CM conductance has been calculated previously using dual-cell patch experiments [35], in such experiments the cells are isolated from surrounding

cells, and interact along a small lateral boundary, with a height of <5 μm [133]. Because in our experimental model cells are densely seeded, with MFBs on top of CMs, the interface between MFB and CM occurs over a large area, and therefore we investigated a wide range of potential CM-MFB conductance values. Our model exhibits all the phenomena seen in our experiments, including conduction slowing and spontaneous beating at increasing light levels, although the light levels at which spontaneous beating occurs is much higher in the model than what is seen experimentally (~0.5 mW/mm^2 vs. ~0.05 mW/mm^2, Figure 20A vs. Figure 14B). Our model suggests that appreciable slowing at baseline and by light-induced current occurs at MFB-CM coupling levels >10 nS/CM (Figure 20B). Additionally, the model explained why, despite the fact that ChR2 has a positive reversal potential near 10 mV, and therefore would be expected to slow repolarization and prolong APD, application of light decreased APD_{80} (Figure 21A). This occurred because it made RP more positive (Figure 21B), while reducing the maximum depolarization (Figure 21B) by suppressing sodium currents (**Error! Reference source not found.**B), decreasing AP amplitude. In this case, it decreased the amplitude more than it decreased the repolarization rate, resulting in a shorter APD. These offsetting effects can explain the mixed effects that inward currents from MFBs have been found to have on APD [61, 62, 64, 78].

Conclusion

This study used MFBs in tandem with optogenetic actuation of ionic current to directly show *in vitro* and *in silico* that inward currents in MFBs can acutely cause ectopic beating and conduction slowing in CM syncytia.

Acknowledgements

This study was conducted in the laboratory of Dr. Leslie Tung, with Yu Shi in the laboratory of Dr. Daniel H. Reich, Shoshana Das in the laboratory of Christopher S. Chen, as well as input and materials from Dr. Emilia Entcheva. It was supported by NIH grant R01 HL127087. Confocal imaging was supported by NIH grant S10 RR024550 (Scot Kuo). This work has appeared in abstract form [151], as well as a platform presentation at the 2019 Biophysical Society Annual Meeting.

Chapter 3: cardiac fibroblasts are sufficiently electrically connected to cardiomyocytes to cause electrophysiological changes in cardiomyocytes

Introduction

CFBs make up about 10% of the cells in the healthy mammalian heart [152]. While early work used dual-cell patch clamp to show CFBs were electrically connected to CMs near the sinoatrial node [153], and suggest CFBs could modulate spontaneous beating rate [40], this technique has not been applied successfully in the ventricle. Quinn et. al. used optogenetic sensing to argue that CFBs do not connect to CMs, since there was no detectable time-varying signal in optical voltage traces from CFBs in a beating intact heart, despite clear signal resembling APs from areas of injury where MFBs resided [145]. Given the slowing attributed to electrical connection of MFBs to CMs, electrical connection to CMs being a phenomenon unique to MFBs, which are not present in the healthy heart, is reasonable. However, i*n vitro* studies have conflicting reports on whether Cx43 expression is increased or decreased in MFBs relative to CMs (Table 10), with most studies finding an increase in Cx43 expression after MFB differentiation at the transcript [35, 154, 155], protein [62, 79, 155], and functional [35, 62, 79] levels, but others finding no change [84], or even a decrease [38, 61].

The clearest evidence that CFBs are electrically connected to CMs comes from Salvarani et. al [35]. In order to maintain cells as CFBs, they treated CFBs with a TGF-β receptor I blocker, which has been found to prevent CFBs from differentiating into MFBs

in culture [32]. They found electrical connections between CFBs and CMs using dual-cell patch clamp at a level about 1/5 that between MFBs and CMs. Despite this, they found that CFBs did not cause conduction slowing in CM syncytia. In this work, we use a similar TGF-β receptor I blocker to maintain CFBs in their fibroblastic state, and optogenetics to demonstrate CFBs are sufficiently electrically connected in syncytia to produce conduction slowing in CMs, if they have sufficient inward currents.

Paper	MF Cx43/ CF Cx43	Method	model	How MF were made	Passage/ Day
Vasquez 2010	2.34	Western	adult rat	infarction	P1-3 up to 1 month
	1.81	FRAP			
	1.35	Western			Freshly isolated
Zhang 2010	3	Western	Adult mouse	infarction (infarct region)	P1 day 4
	3			infarction (away from infarct)	
	1.75	Dye transfer distance		infarction (infarct region)	
	1.59			infarction (away from infarct)	
	2.03	Western		24 h 10 ng/mL TGF-β	P2 day 8
Follonier 2008	~1/3	Staining	Neonatal rat	4 day 2ng/mL TGF- β	P0 Day 4
	~1/4	Dye transfer distance			
Salvarani 2017	1.77	rtPCR	Neonatal rat	24-48 h TGF- β (compared to same time SD-208)	P1 Day 8 (?)
	5.7	nS/um			
Asazuma-Nakamura 2009	No change	Staining	Neonatal rat	5 ng/mL TGF- β up to 72 h (compared to same time 10 μM SB-431542)	P2
Kofron 2017	2.5	rtPCR	Neonatal rat	Transduction of GαQ	Day 3
	5.1			Transduction of GαQQL (constitutively active)	
Doble 1994	~10	mRNA	Neonatal rat	20 ng/mL bFGF	P1 Day 4
	~2.2	Western			

Table 10. Reported changes in connexin expression and function after differentiation from cardiac fibroblast to myofibroblast.

Methods

Unless otherwise noted, methods from Chapter 2 are applied in the same way to CFBs.

Cell culture

CFBs were produced by adding the TGF-β receptor I blocker SD-208 (Sigma) one day after each passage at a concentration of 3 μM. For dedifferentiation experiments, MFBs were created as in Chapter 2, and added to a subset of CMs. 3 μM or 10 μM SD-208 was added to some CMs or MFB/CM co-cultures at the time of MFB plating.

qPCR

Instead of being plated onto CMs, some ChR2-CFBs or ChR2-MFBs were placed in RNAlater (Thermo) for mRNA analysis by Shoshana Das using standard methods.

Gene	Forward Primer	Reverse Primer
GAPDH	GCAAGAGAGAGGCCCTCAG	TGTGAGGGAGATGCTCAGTG
Actb	CCCGCGAGTACAACCTTCTTG	GTCATCCATGGCGAACTGGTG
Rpl7	TCCGAGGTATCAATGGAGTGAGC	ATGCAATGTAGGGCTCCACG
Acta2	CCATCAGGAACCTCGAGAAGC	AGCTGTCCTTTTGGCCCATT
Col1a1	GAGAGGTGAACAAGGTCCCG	AAACCTCTCTCGCCTCTTGC
Col3a1	AGTGGCCATAATGGGGAACG	CAGGGTTTCCATCCCTTCCG
FN-EDA	ACTCAAGCATCGGCCTGAGGTG	TGATGTCATAGTCAATGCCGGGTTCCA
Tgfb1	GGACCGCAACAACGCAATC	TGCTTCCCGAATGTCTGACG
Ccn2	CTAGCTGCCTACCGACTGGAA	ATTGGTAACCCGGGTGGAGA
Postn	CTTGCAAAAAGACACACCTGCAA	AACGGCCTTCTCTTGATCGC
Tnc	ACAACAGCCATGGGCTCTCC	CTCCACCTGAGCAGTCGGT
Fap	CCGTGTATCGAAAGCTGGGT	AACCTCCGTAGGACCATCCC
Gja1	TTTCATTGGGGGAAAGGCGT	GTCTGGGCACCTCTCTTTCAC
Gjc1	CCTCCCCGCTTTTCGGATTAT	CCCAAATTCTCTCTTGAGTTCCTCG
Scn5a	CAAGCCCTACGCCGAGC	GCCTGGAAGGAAGCTGATG
Kcnd3	CGAACCTCCACCATCAAGAACC	TGCGTGGTCTTCTTGCTACG
Nalcn	CGCAACCTGAGTCAAGCAGT	CAGACGCCATTGCCCAATCT
Abcc9	TGGACGATCCATTCTCCGCT	CTATGATCCAGTCCGCGTGC
Kcnh2	AAGTTTGAGGGCCAGAGCCG	CCATGCAGGAAATCGCAGGT
Kcnk3	CGTCATCACCACAATCGGCTAT	TGTTGATGCGTTCACCCAGG
ChR2	ATACTGTGCCAAAGGGTCGG	TGACCTACGGTGGAGCCATA
Trpm7	TGTACCTCCACGAGGTGAGC	GCTCTTCGTAAACCGCCTCC
Trpc3	ACCAAGGTCAAGAAGTGCCG	ATGTTGCCGTACTGCGTCG
Trpc1	TGCGTAGATGTGCTTGGGAG	CGTTCCATAAGTTTCTGACAACCG
Trpc6	CTATCCCAGCTTCCGGGGTAA	TGCATCCAGAAAGCGTTCCTC
Trpv4	TCCCAAGCAGGCCGAGAAG	CAGGGAAGAGAGGGGGAAG
Cdh2	GGCCTTGCTTCAGGCATCTC	GCACGTCCTTCGGTAAGACC
Cdh11	GAATGGGACTGGGACTGG	AGTAATTTCTGGGGCCCTTGC

Table 11. Primers for qPCR.
Primers chosen by Shoshana Das.

Fibroblast vs. myofibroblast size and strain energy measurements

CFBs and MFBs were produced as described above and in Chapter 2, except after the second passage, 10,000 cells were plated in a 35-mm dish onto force-sensing micropost arrays produced as described previously [156]. Cells were imaged 20 h after seeding via bright field using an inverted microscope (Nikon TE-2000), and total strain energy for each cell type was calculated. These experiments were conducted by Yu Shi. Cell area (A) in was calculated as $A = \frac{\sqrt{3}}{4} d(P \quad 2)$, where d is the distance between the microposts (making $\frac{\sqrt{3}}{4} d$ the area of each equilateral triangle formed by the microposts), and P is the number of microposts covered (since the number of contiguous triangles covered is always 2 less than the number of vertices). For our micropost arrays, $d = 16\ \mu m$.

Mathematical modeling

Currents for CFBs were modeled by a hyperbolic least squares fit of $I_{CFB} = (a \tanh(V_{CFB} + b) + c)(V_{CFB} + b) + d$ to the I/V curve measured by Salvarani for TGF-β1-treated CFBs [35], resulting in $I_{CFB} = (0.0081 \tanh(V_{CFB} + 15) + 0.0206)(V_{CFB} + 15) + 0.437$, with I_{CFB} in nA, and V_{CFB} in mV (Figure 22).

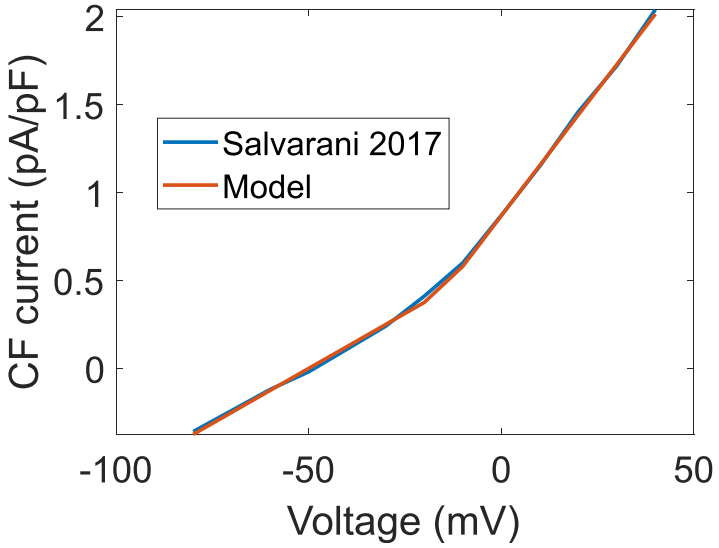

Figure 22. Fibroblast current-voltage relationship of experimental data vs. model.

Results

Fibroblast transduction

We transduced CFBs with different amounts of virus to determine the proper viral dose. We found that unlike for MFBs, the highest dose of virus decreased ChR2 expression, likely due to increased cell death (Figure 23). We choose to use 2,000 MOI for experiments to match the MFB dose and because it maximized the number of transduced cells.

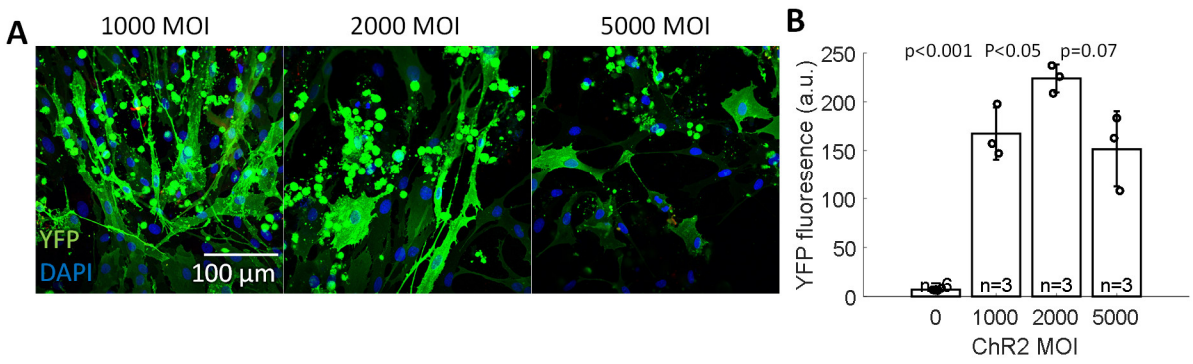

Figure 23. Transduction of fibroblasts with ChR2.
A. Confocal images of SD-208-treated CFBs transduced with varying multiplicity of infection of ChR2 adenovirus. Green shows YFP, which marks cells transduced with ChR2, and blue shows DAPI, labeling cell nuclei. Higher doses of virus were associated with significant cell death (rounded cells). All images are taken at the same scale and settings. **B.** YFP fluorescence at different MOI.

Characterization of fibroblasts and myofibroblasts

To ensure that cells treated with SD-208 were behaving as undifferentiated CFBs, and that cells differentiated into MFBs by TGF-β1 were behaving as differentiated MFBs, we performed qPCR for transcripts known to be upregulated in MFBs. We found increases in all of the transcripts, and all but one were significant (Figure 24). We also stained both cell types for α-SMA. We saw high expression of α-SMA in the TGF-β1-treated cells, and very little expression in the SD-208-treated cells (Figure 25A). To demonstrate quantitatively the difference in α-SMA expression, we used a plate fluorescence reader to obtain an average fluorescence measurement from each well and found that TGF-β1-treated cells indeed expressed significantly more α-SMA than SD-208-treated cells (Figure 25B). We also seeded CFBs treated with SD-208 or TGF-β1 onto micropost arrays at low density to measure the strain energy they produced (Figure 25C). CFBs treated with TGF-β1 were significantly larger (1350±620 vs.

370±600 μm^2, Figure 25C-D) and had a greater strain energy per cell area (0.163±0.100 vs. 0.069±0.065 fJ/μm^2, Figure 25E) than those treated with SD-208.

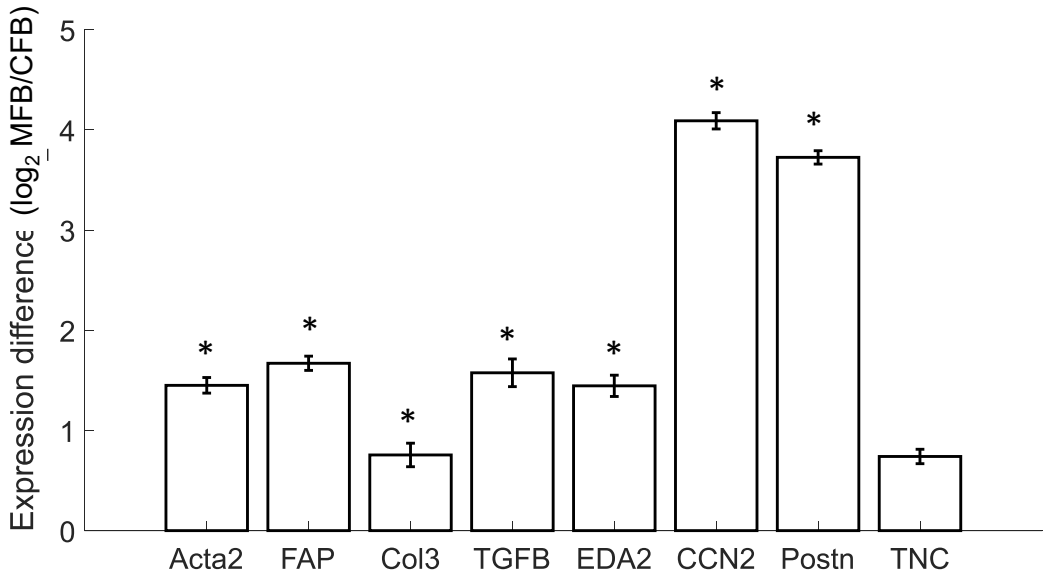

Figure 24. qPCR of fibroblasts and myofibroblasts.
qPCR showed increased expression of transcripts expected to be upregulated in MFBs relative to CFBs. n=2 technical replicates. * = $p<0.05$. Data from Shoshana Das.

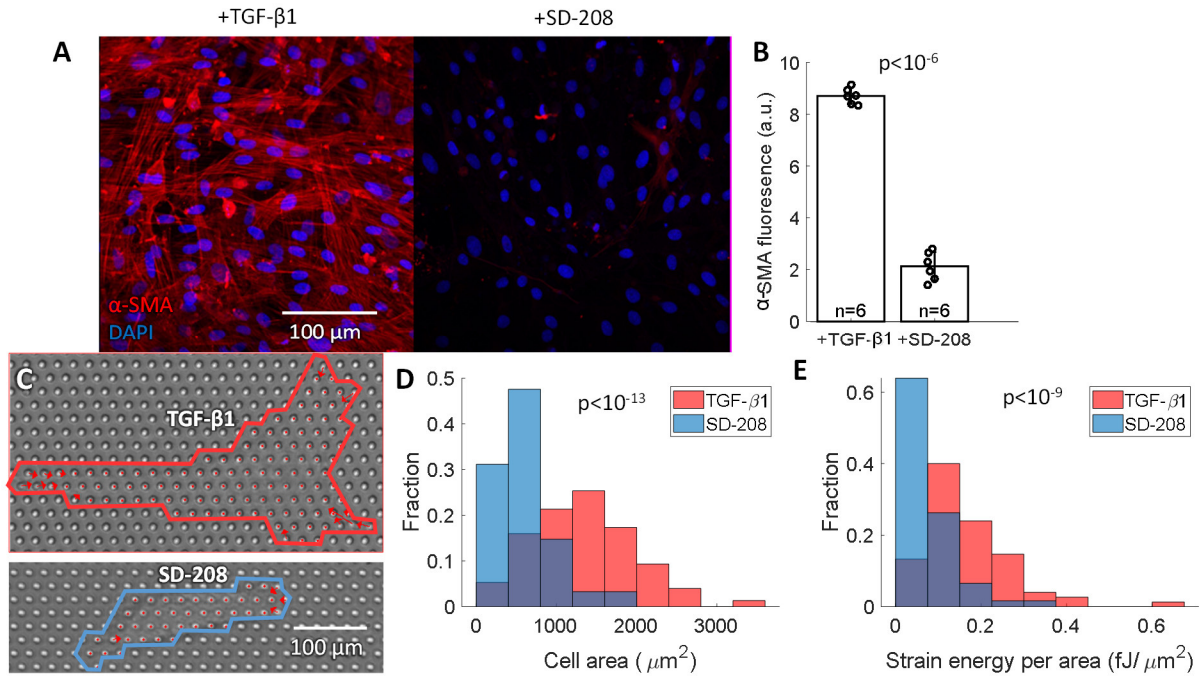

Figure 25. Comparison of fibroblasts and myofibroblasts
A. Confocal images of CFBs treated with TGF-β1, and the TGF-β receptor I blocker SD-208. Smooth muscle actin (α-SMA, red) is a marker of differentiation into a MFB, and DAPI (blue) shows cell nuclei. All images are taken at the same scale and settings. **B.** α-SMA fluorescence in multiple wells for each treatment as measured by a plate reader. **C-E.** TGF-β1-treated and SD-208-treated CFBs were seeded at low density on microposts by Yu Shi to measure strain energy. **C.** Red dots show posts where a TGF-β1-treated (top) and a SD-208-treated (bottom) cell attached to posts, and arrows show force vectors. Figure modified from figures made by Yu Shi. **D.** Histograms of areas of cells treated with TGF-β1 (red, n=75) or SD-208 (blue, n=61). **E.** Histograms of strain energy, as calculated by Yu Shi, per area, of the same cells as in **D**.

Fibroblast currents can also cause electrophysiological changes in cardiomyocytes

Having demonstrated that MFBs were sufficiently electrically connected to CMs for inward currents in MFBs to cause electrophysiological changes in CMs (Chapter 2), we examined if the same was true for CFBs. We found that application of light to ChR2-CFB/CM co-cultures caused statistically significant, reversible, dose-dependent spontaneous beating faster than the 2 Hz paced rate (CL at 0.057 mW/mm^2 light = 258±22 ms for ChR2-CFB/CM vs. 500±2 ms, p<.001, Figure 26A). We also found

application of light caused reversible conduction slowing in ChR2-CFB-CM co-cultures (ΔCV at 0.006 mW/mm^2 = -1.2±1.5 cm/s, p=0.04, Figure 26B), although because of the high propensity for spontaneous beating, we were only able to measure one sample at the higher light intensity. Similarly, we found a significant decrease in APD_{80} (ΔAPD_{80} at 0.006 mW/mm^2 = -6±6 ms, p=0.01, Figure 26C). Other p-values are included in Table 9.

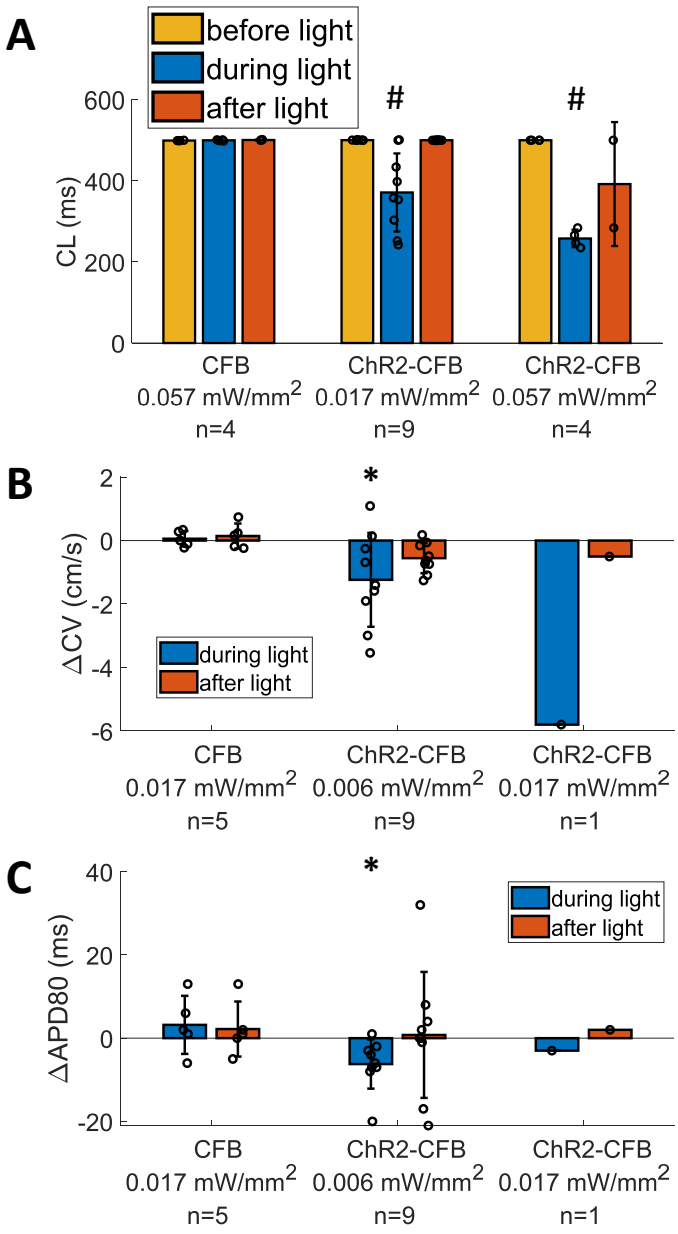

Figure 26. Effects of light induced currents in ChR2-transduced fibroblasts on co-cultured cardiomyocytes.

A. Cycle length before, during, and after application of light at different power during 2 Hz pacing, for co-cultures of CM with CFB or ChR2-transduced CFB. **B.** Change in CV (vs. before light application) during and after application of light at different power during 2 Hz pacing, for co-cultures of CM with CFB or ChR2-transduced CFB. **C.** Change in APD_{80} (vs. before light application) during and after application of light at different power during 2 Hz pacing, for co-cultures of CM with CFB or ChR2-transduced CFB. * shows $p<0.05$ and # shows $p<0.005$ difference in parameter before vs. during light application.

Blockade of TGF-β receptor I reduces effects of cardiac fibroblasts that have already differentiated into myofibroblasts

To investigate if TGF-β receptor-I-blockade could reduce the effect MFBs had on CV by changing their electrophysiology to be more like CFBs, we added SD-208 to CMs as well as to MFB/CM co-cultures. We found that MFB significantly slowed CV, while SD-208 only had a non-significant negative effect on CV. However, SD-208 significantly reduced the slowing caused by MFBs.

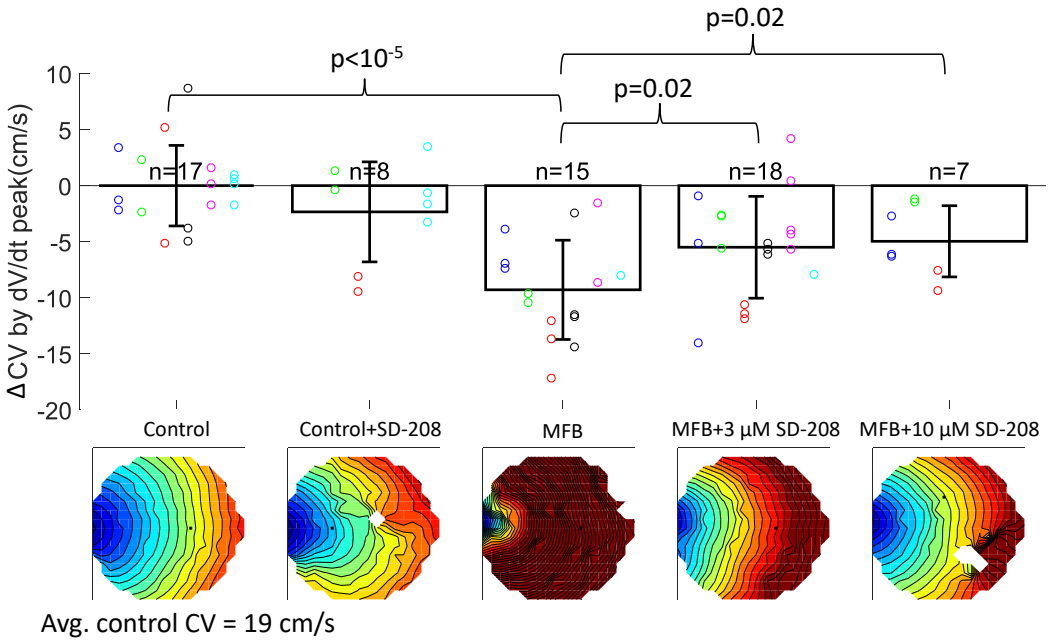

Figure 27. The TGF-β receptor blocker SD-208 partially reverses myofibroblast-induced conduction slowing.
Conduction velocities were normalized to the mean of the control for each group. Colored circles indicate samples from different cell batches. Representative activation maps for each group displayed below bar graph (5 ms isochrones, 17 mm diameter).

Comparison of experimental results to mathematical model

To understand the effects of ChR2-CFBs on CMs, we changed our current-voltage formula to that of CFBs treated with the TGF-β-receptor I blocker SB431542 [35] that maintained them in a CFB state (Figure 22). We found similar spontaneous

beating and CV decreases, although spontaneous beating began at lower light intensity in ChR2-MFB co-cultures (Figure 28A vs. Figure 20A), while light caused more slowing in ChR2-CFB co-cultures (Figure 28B vs. Figure 20B). Unlike in ChR2-MFBs, where increased conductance between CMs and MFs always decreased APD_{80}, in ChR2-CFBs with low light levels, increasing CFB-CM conductivity actually increased APD_{80} (Figure 28E vs. Figure 21A). To compare our optogenetic actuation method to optogenetic sensing, we plotted the voltage amplitude of CFB depolarizations caused by CM APs, which would be measured in optogenetic sensing, versus the change in CV caused by high intensity (1 mW/mm^2) light applied to ChR2-CFBs, which would be measured using the optogenetic actuation method described in this work. We found that while both increase with increasing CFB-CM coupling, as expected, fluctuations in CFB voltage become measurable at levels of connectivity at which the CFB cannot influence CM CV (Figure 28F, 0.0001 μS/CM).

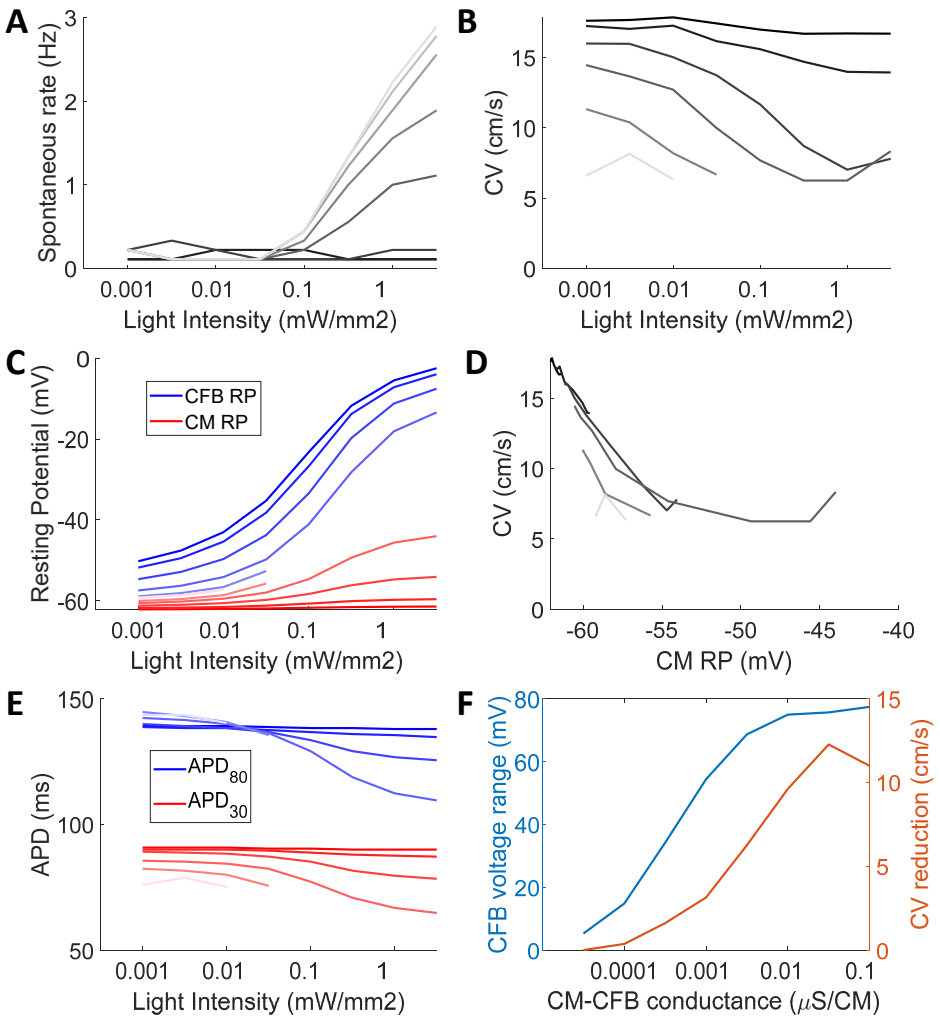

Figure 28. Modeling a strand of ChR2-transduced fibroblasts on top of a strand of cardiomyocytes.
Some data missing due to spontaneous beating faster than paced 2 Hz rate or to block. **A-E:** MFB-CM coupling varies by half-log10 increments from $10^{-4.5}$ μS (dark) to 10^{-1} μS (light). **A.** Spontaneous beating rate for CMs at different CFB-CM coupling and light intensities. **B.** CV for CMs at different CFB-CM coupling and light intensities. **C.** RP of CFB (blue) and CM (red) at different coupling levels and light intensity. **D.** CV vs. RP for strands from **B** and **C. E.** Effect of cell coupling and light intensity on APD_{80} (blue) and APD_{30} (red). **F.** Comparison of optogenetic sensing and actuation. Blue line shows CFB voltage amplitude, which is measured using optogenetic sensing. Orange line shows CV reduction by application of high levels of light, which is measured during optogenetic actuation.

Discussion

In vitro model and TGF-β receptor blockade

While it is well-known that CFBs spontaneously differentiate into MFBs over time in culture [157], the fraction of differentiated CFBs ranges significantly between studies, from <0.01% after five days [78] to >90% after one day [63] for similar cell sources and culture conditions. Furthermore, CFB to MFB differentiation occurs along a spectrum, with at least one intermediate state of proliferating α-SMA-expressing cells, while fully differentiated MFBs do not proliferate [32]. In order to consistently produce fully undifferentiated CFBs we applied the TGF-β receptor I blocker SD-208 to our CFBs and demonstrated decreased expression of genes that are upregulated in MFBs [123, 158–162] (Figure 24), as well as decreased α-SMA protein expression (Figure 25A-B), size (Figure 25C-D) and contractile energy (Figure 25E). This is in agreement with previous results showing TGF-β receptor I blockers prevent CFBs from differentiating to MFBs, as demonstrated at the message level by differences in gene expression [32, 35], structurally by the suppression of SMA [32, 35], vinculin [32], and collagen [32], as well as functionally by suppression of contractility [32]. Despite the finding by Driesen, et. al. that MF differentiation by high levels of TGF-β is irreversible, we were still able to improve CV in MFB/CM co-cultures by treatment with SD-208 (Figure 27), suggesting that SD-208 may change MFB electrical phenotype to be more similar to that of CFBs, while leaving the increased contractile and possibly even ECM production properties of MFBs intact. However, we have not ruled out SD-208-induced apoptosis of MFBs as a mechanism for this effect.

Fibroblasts are also sufficiently electrically connected to cardiomyocytes to cause slowing

While there is clear evidence that MFBs electrically couple to CMs, at least *in vitro*, fewer studies have shown CFB coupling *in vitro*, and many early studies are marred by the fact that CFBs spontaneously differentiate into MFBs over time *in vitro* [157]. The first suggestion of CFB-CM electrical coupling was by Rook, et. al. using dual-cell patch clamp [76]. They were able to conclusively show that CMs and non-CMs could electrically connect, and even demonstrated excitation passing through a CFB bridge to excite a distal CM. While they conducted their experiments within 24-48 hours of isolating the cells, they did not do any characterization of their CFBs to determine whether they had spontaneously differentiated in MFBs, as has been reported to occur within this timeframe, and so may have been working with MFBs [63]. Kohl, et. al. were able to use microelectrode recordings of adjacent cells in SAN to argue CFB could couple to CM [153], but as they pointed out, it is difficult to tell the difference between a recording of a CFB and that of a poorly impaled CM because CFB are expected to act as a voltage follower of CMs [70].

Fahrenbach, et. al. found CFBs could cause slowing and spontaneous beating similar to that caused by MFBs, but they used CFBs up to passage 10, and did not confirm they were CFBs, so they were in fact almost certainly MFBs. Kizana, et. al. noted that CMs cultured on Cx43-KO mouse CFBs spontaneously beat at a higher rate than those cultured on WT CFBs, but did not explain their method for culturing CFBs and also may have been working with MFBs [163]. Vasquez, et. al. found that CFBs isolated from adult rat hearts could cause some slowing when they were plated on top

of CMs, although not as much as (likely MFBs) isolated from infarcted hearts [62], however these were cultured for up to a month, and were therefore likely proto-MFBs. McSpadden, et. al. also found CFBs could cause slowing, and used FRAP to argue that they were electrically connected to CMs [78]. While their CFBs were a week old, they found no expression of smooth muscle actin at day 5, suggesting that they were in fact still CFBs. Salvarani et al. found that unlike MFBs, fully undifferentiated CFBs do not cause slowing, despite dual-cell patch clamp showing CFBs were electrically connected to CMs [35]. They suggested the lack of slowing was due to reduced CFB-CM coupling (as suggested previously [62]) or reduced currents in CFBs relative to MFBs. This study expands on their results, demonstrating that CFB-CM coupling is present in syncytia, and that it is sufficient to cause slowing, given adequate inward currents in CFBs (Figure 26). In light of this, as well as the conflicting data about changes in gap junction expression in CFBs vs MFBs (See Table 10), changes in gap junction expression between CFBs and MFBs may not be a significant factor in their difference in arrhythmogenicity. Furthermore, CFBs may be relatively benign despite significant electrical connection to CMs because recent flow cytometry has shown CFBs make up a relatively small proportion of the healthy heart, with 30% of all cardiac cells being CMs, and only about 10% being CFBs [152]. Additionally, the smaller size of CFBs versus MFBs and CMs means that they have smaller currents on a per-cell basis, assuming the same current densities (per sarcolemmal area).

Mathematical modeling

We based our model off steady-state currents from Salvarani, et. al. [35], because we could find no other data source that maintained a CFB state using a TGF-β

receptor I blocker as we did. We found that ChR2-CFBs required more light to produce spontaneous beating than ChR2-MFBs (Figure 28A vs. Figure 20B). This is likely due to the elevated RP of MFBs contributing more inward current during diastole to initiate beating. However, we found that application of light produced less slowing in ChR2-MFBs (Figure 28B vs. 17C). This is because the MFB currents cause more initial slowing at a given MFB-CM conductance, and eventually the slowing effect saturates at about 5 cm/s as all the sodium channels inactivate and conduction is calcium-mediated. Therefore, there is less room for light application to cause slowing in ChR2-MFBs compared to ChR2-CFBs. The level of electrical coupling required to produce slowing (0.3-1 nS, Figure 28B) is significantly less than that expected between MFBs and CMs, even considering our MFB to CM ratio of 0.4 ($0.4 \quad 50\ \mu m \quad \frac{2.8\ nS}{\mu m} = 56\ nS$), as well as that expected between CFB-CM pairs ($0.4 \quad 50\ \mu m \quad \frac{0.5\ nS}{\mu m} = 10\ nS$) [35], supporting the hypothesis that electrical connection between even CFBs and CMs is sufficient to allow electrophysiological coupling effects in CMs, given adequate CFB currents, which is in agreement with our experimental findings (Figure 26B).

Our model allowed us to compare optical sensing and actuation. We found that optogenetic sensing may be too sensitive, since at intermediate conductance levels, CFBs can be connected to CMs, but still be incapable of causing slowing in them (Figure 28F). This illustrates that there is a difference between the degree of coupling for CMs to drive CFBs, which can occur at low coupling due to the high resistance of CFBs, and for CFBs to alter CM electrophysiology, including CV, as has been discussed previously [70, 134].

Future directions

The current study suggests that using a design similar to the optogenetic sensing study by Quinn et. al. [145] but with an optogenetic actuator could directly determine whether MFBs or even CFBs are electrically connected enough to allow conduction slowing and spontaneous beating in CMs *in vivo*. Clinically, the suggestion that even CFBs are electrically connected enough to CMs to cause slowing, provided there is sufficient inward current, suggests that the important difference between innocuous CFBs and deleterious MFBs is not simply due to MFBs having increased electrical coupling, but instead their heterogeneous distribution, as well as increased size and sarcolemmal currents. Therefore, drugs that dedifferentiate MFBs or otherwise reduce their currents may be more useful than simply blocking MFB Cx43 in treating sudden cardiac death following cardiac injury, such as myocardial infarction. In fact, a series of studies has found application of Cx43-transduced MFBs or skeletal myoblasts, or direct injection of Cx43 lentivirus to an infarct reduced the risk of arrhythmia [59, 164], further suggesting reducing Cx43 expression in MFBs may not be helpful. Therefore, a component of the salutary effects of MFB dedifferentiation drugs may be improvement of MFB electrophysiology, specifically decreased inward currents and less depolarized RP, and this presents an interesting avenue of investigation, for which we have preliminary evidence (Figure 27). Indeed, a number of drugs shown clinically to reduce sudden cardiac death in the context of heart failure also may dedifferentiate MFBs, such as losartan [165], ramipril [166], and simvastatin [167], allowing the possibility of MFB dedifferentiation as a mechanism of action. Finally, the ability of continuous current, optogenetic or otherwise, to increase spontaneous beating rate (Figure 26A), while still

allowing for endogenous regulation of beating rate, may be applicable in the sinoatrial node to treat sick sinus syndrome.

Conclusion

This study used pharmacological promotion of a CFB phenotype in tandem with optogenetic actuation of ionic current to directly show that inward currents in CFBs can acutely cause ectopic beating and conduction slowing in CM syncytia.

Acknowledgements

This study was conducted in the laboratory of Dr. Leslie Tung, with Yu Shi in the laboratory of Dr. Daniel H. Reich, Shoshana Das in the laboratory of Christopher S. Chen, as well as input and materials from Dr. Emilia Entcheva. It was supported by NIH grant R01 HL127087. Confocal imaging was supported by NIH grant S10 RR024550 (Scot Kuo). This work has appeared in abstract form [151], as well as a platform presentation at the 2019 Biophysical Society Annual Meeting.

Chapter 4: An optogenetic chronic point-pacing system for maturation of cardiomyocytes

Introduction

Many papers have shown the benefits of chronically pacing CMs (reviewed in [92, 93]), however, electrical pacing requires a specialized set-up, and in many cases increases the risk of contamination since electrodes or an agar bridge must be in direct contact with cell media. Furthermore, the electrodes generate ROS and metal ions in solution (depending on electrodes or presence of agar bridge) [168], which may stress cells. An optogenetic approach has the potential to eliminate these problems by allowing for contactless pacing. Systems for chronic optical field pacing have been made by individual labs [169], and commercially [170], but only one recent publication [171], used it to mature CMs, and all still had used a single LED per plate, necessitating special plates or other equipment to use. In this study, we use forced aggregation of HEK-293 cells stably transfected with ChR2 ("spark" cells) to create "spark" clusters, which we then add to CM monolayers and use with a large LED panel, allowing us to point pace them in a simple, contactless, and scalable way (Figure 29).

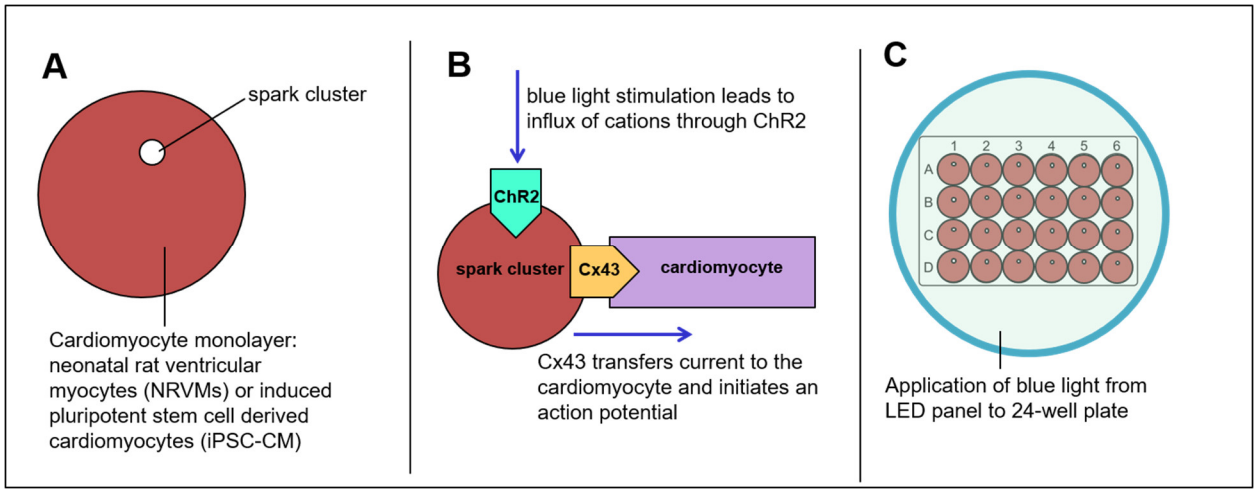

Figure 29. Planned optogenetic pacing system.
(A) A cluster of ChR2-transduced HEK cells (spark cells) is placed on top of a CM monolayer and allowed to attach. (B) A spark cluster electrically connects to CMs, allowing for light-induced inward currents to spread to the CMs and stimulate them. (C) By simply adding a single cluster to each well, a global flash of light can simultaneously point stimulate multiple wells. Figure by Shivani Pandey.

Methods

Stimulator design and testing

A commercially available LED panel (Yescom, 15x15 LED, 28.5 mm x 28.5 mm, 1.7 cm between LEDs, 22W, 2475 lm) was stripped of its AC/DC converter and connected directly to a custom circuit (Figure 30) built with Dr. Renjun Zhu. This circuit employed a Darlington transistor pair to amplify the output of a waveform generator (Agilent 33229A). For use in conjunction with an in-incubator microscope, one side was cut down to 27 mm, and a 7 mm hole was punched out of the panel between four central LEDs, without damaging any LEDs. Under my supervision, Shivani Pandey constructed a brightness-voltage curve for the circuit by positioning the LED panel 4 cm away from an optical power sensor (Thorlabs PM100A), setting the voltage on a variable power supply (TekPower TP5003T) to 42 V, and moving it to different regions under the central region of the LED panel, recording the local maximum and minimum

brightness. She also made a current-voltage curve by recording the current at each voltage between 42 V and 50 V. Finally, she made a brightness-distance curve for the circuit by setting the voltage to 42 V and recording the maximum brightness at each distance. Based on this data, in the final iteration, a 54 V, 3.45 A power supply (Mean Well HLG-185H-54A) was used to power the LED panel.

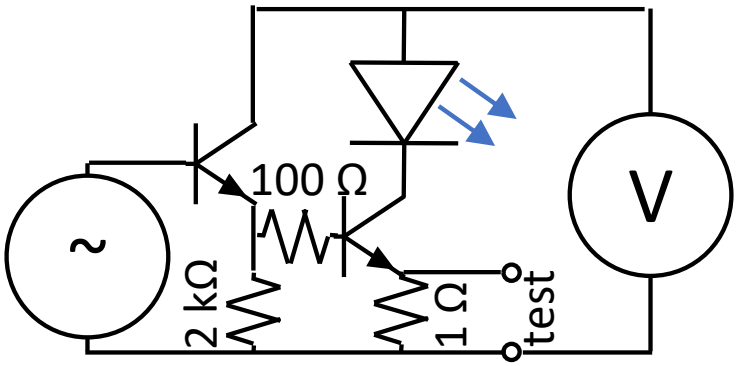

Figure 30. Schematic of optical stimulation control circuit
A Darlington transistor pair was used to amplify the signal of a waveform generator. A test lead was included to measure current through the LED.

Spark cluster fabrication

Spark cells were provided by the lab of Dr. Emilia Entcheva. They were seeded at $2x10^4$-$1x10^5$ per well in either a 0.5% 96-well V-bottom plate (ThermoScientific Nunc) coated with agarose (Sigma) or a 96-well Corning® Spheroid Plate (Sigma Aldrich, CLS4520), in approximately 200 µL CM culture media. In some cases, the plates were centrifuged at 800g for 10 minutes to concentrate cells in the bottom of the plate to try to improve aggregation, before being placed in an incubator overnight. Spark cells were produced and maintained by either Shivani Pandey or Renjun Zhu.

Cardiomyocyte isolation

NRVMs were isolated and plated as described in Chapter 2. Monolayers were kept in culture for 1-4 days to allow formation of a syncytium as well as resumption of spontaneous beating before spark clusters were introduced.

An arrhythmogenic right ventricular dysplasia 25.8 hiPSC line with a heterozygous PKP2 mutation c.971_921InsT [6] was a kind gift from Dr. Lior Gepstein. hiPSC-CMs were produced using a monolayer-based protocol [7], dissociating at day 40 after initiating differentiation and plating onto coverslips (Nunc, Thermanox, Thermo) coated with 1:150 Geltrex (Thermo) at a density of 240,000 CMs/cm^2. The resultant hiPSC-CM monolayers were maintained in culture for 3 days prior to adding spark clusters. hiPSC-CMs were produced and maintained by Dr. Adriana Blazeski.

Optical mapping

NRVM monolayers with spark clusters were stained with di-4-ANBDQBS as described and mapped in Tyrode's solution using a MiCam Ultima system. Optical voltage recordings were collected with Dr. Renjun Zhu using a 655 nm excitation LED module (Luxeon SinkPAD-II Rebel 7 LED Round Module), and a 760 nm long-pass excitation filter (Newport, 20CGA-760). Spark clusters were excited with a 470 nm LED module (Luxeon SinkPAD-II Rebel 7 LED Round Module).

Chronic pacing and immunostaining

Spark cells were given twelve hours to electrically couple to CMs prior to beginning pacing experiments. Then, with Shivani Pandey, the cells were placed on a microscope system with an automated stage (Etaluma Lumascope 720) in an incubator, and the LED panel was positioned 4.5 cm away from the cells to chronically pace them

in culture, using square light pulses at a constant pulse width of 20 ms and brightness of 0.2 mW/mm^2. 30-second videos of cell beating at 35-50 fps (as limited by data transfer rate) were recorded every 15 minutes for up to 10 hours. After pacing experiments, cells were fixed, permeabilized, and immunostained by Shivani Pandey with rabbit anti-GFP (Invitrogen), and mouse IgG1 anti-α-actinin (Sigma Aldrich) using standard procedures.

Contraction and beating rate measurement

Videos of cell contraction were analyzed using custom MATLAB software. Light flashes were identified by saturated signal in a vertical line scan, and video images during light flashes were replaced with neighboring frames. A contraction surrogate at each frame (C_t) was calculated as $C_t = \sum_x \sum_y \left(I_{xyt} \quad I_{xyk}\right)^2$ where I_{xyt} is the brightness of an individual pixel, and I_{xyk} is the brightness of the same pixel during the reference or "key" frame. The first 5 frames of a video were tested as the key frame, with the one leading to the highest variance of C_t being used, to prevent the key frame from occurring in the middle of contraction, which led to two smaller deflections for each beat, rather than a single larger deflection. C_t was then linearly dedrifted, and a 3 or 5 point derivative calculated. Capture was identified by the peak of the signal derivative exceeding a threshold, which was defined manually for each CM sample to properly record visible beats.

Spark cell transduction with Cx43 and sorting

Under my guidance, Shivani Pandey plated spark cells and HEK-293 cells in a 6 well plate and transduced subsets with Cx43-GFP lentivirus (a kind gift from Dr. Gordon Tomaselli) at 10 MOI. Cells were trypsinized and collected for fluorescence-activated cell sorting by the Ross Flow Cytometry Core at the Johns Hopkins School of Medicine

to separate out ChR2/Cx43 positive cells (as indicated by YFP andGFP fluorescence, respectively), by using YFP+ only, GFP+ only, and double-negative cells as controls.

qPCR on spark cells

1 mL Trizol (Life Technologies) was added to wells containing spark cells and Cx43-transduced spark cells, and cell lysate was transferred to 1.5 mL tubes. Five minutes later, 200 µL chloroform was added to each tube, and they were shaken for 15 s. Three minutes later they were centrifuged at 12,000g for 15 min at 4°C. After this the upper layer was carefully transferred to new tubes. 500 µL isopropyl alcohol was added, and the tubes were shaken vigorously. Ten minutes later the tubes were centrifuged for 10 min at 12,000g at 4°C, after which the supernatant was discarded. The remaining RNA pellets were resuspended in 1 mL 75% ethanol, before being centrifuged for 5 min at 7000g at 4°C and discarding the supernatant. The previous step was repeated to further rinse the RNA, then the tubes were placed upside-down on Kimwipes (Kimberly-Clark) for 5-15 min to remove the rest of the ethanol. Finally, the RNA was suspended in 50 µL DEPC water (Invitrogen), before being quantified using a Nanodrop spectrophotometer (Thermo-Fisher). RNA was converted to cDNA using the PCR Master Mix kit (Thermo Fisher Scientific, Waltham, MA), with the MyGo Mini PCR system (IT-IS Life Science Ltd., Republic of Ireland). Four replicates of qPCR were performed on GAPDH in Cx43-transduced and untransduced cells, using the forward and reverse primers GGCCTTCTTGCTGATCCAGT and TCTTCATGCTGGTGGTGTCC for Cx43, and CCCACTCCTCCACCTTTGAC and CCACCACCCTGTTGCTGTAG for GAPDH. The PCR program run for each sample consisted of 120 seconds hold at 95°C, 40 cycles of amplification that alternated

between 90°C and 65°C, 10 seconds pre-melt hold at 95°C, and a melting step that increased from 60°C to 97°C at 0.1°C/second. CT values were obtained using MyGo Mini PCR Software (IT-IS Life Science Ltd., Republic of Ireland)

Statistics

All data are reported as mean±SD. Paired or unequal variance t-test was used to determine statistical significance as appropriate.

Results

Optogenetic stimulator design

To choose a power supply, brightness-voltage, current-voltage, and brightness-distance curves for the panel were constructed (Figure 31). The brightness-distance curve showed that light intensity varied significantly depending on whether a sample was directly under or in between LEDs for separation distances <4 cm (Figure 31A). Therefore, in our final iteration, this distance was set at 4.5 cm. To limit light exposure, we wanted to choose a pulse duration that could stimulate with the least energy. Based on previously published work examining stimulation threshold for an island of spark cells surrounded by NRVMs, we expected ~20 ms light duration would allow the lowest pacing power, with a stimulation threshold of ~0.04 mW/mm^2 [172]. Brightness-voltage curves showed that we could achieve 0.15 mW/mm^2 at 50 V and 4 cm, and current-voltage curves showed 2.3 A current at 50V, so we chose a power supply that could output 54V and 3.45A. We attempted to measure brightness and current draw from this power supply directly, but our circuit could not output enough current long enough for us to measure it in the system. Instead, we extrapolated our current-voltage and voltage-

brightness curves, to conclude this supply is current-limited (See Figure 31B) and outputs 0.2 mW/mm^2 at 4 cm (Figure 31C), which based on our brightness-distance measurements is a minimum of 0.16 mW/mm^2 at the 4.5 cm we used in our final iteration (Figure 31). This gives us a safety factor of ~4, which is important since some light will be absorbed or reflected by the tissue culture plates.

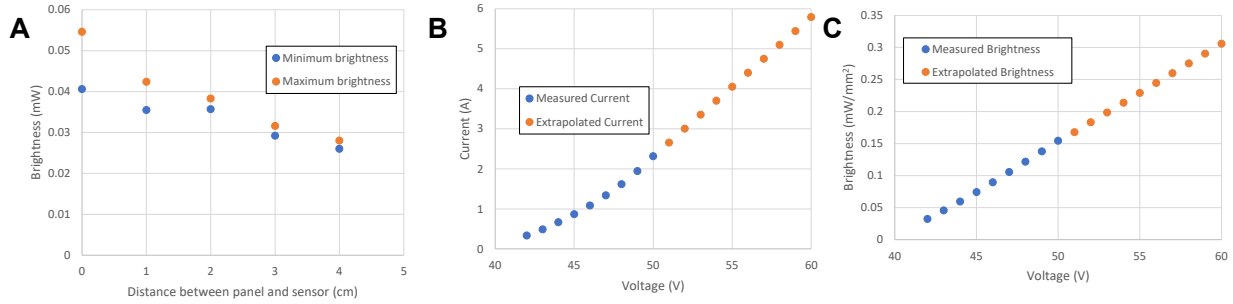

Figure 31. Design curves for optogenetic stimulation
A. Light brightness vs. distance at 42 V. Sensor was moved laterally to find maximum and minimum brightness at each distance due to spacing of LEDs. **B.** Current vs. voltage for LED. Variable power supply could only output 50 V, so currents at higher voltages are extrapolated. **C.** Brightness vs. voltage for LED, measured at 4 cm. Variable power supply could only output 50 V, so brightness at higher voltages are extrapolated. From Shivani Pandey.

Cluster fabrication and characterization

Spark cells plated into low-attachment 96 well plates and centrifuged formed clusters within 24 hours (Figure 32). In one batch, HEK-293 cells formed clusters in 21 out of 24 agarose-coated wells. Confocal imaging of a cluster on CMs demonstrated continued expression and proper trafficking to cell membranes of ChR2-YFP *in situ*. The clear boundary of the cluster demonstrated that the cells remain grouped together and did not diffuse into the CM substrate (Figure 33).

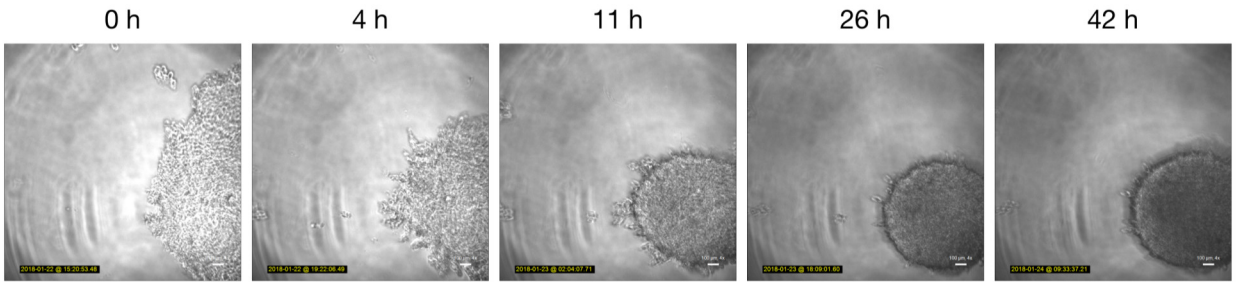

Figure 32. Time lapse images of cluster formation.
Scale bar is 100 μm. From Dr. Renjun Zhu.

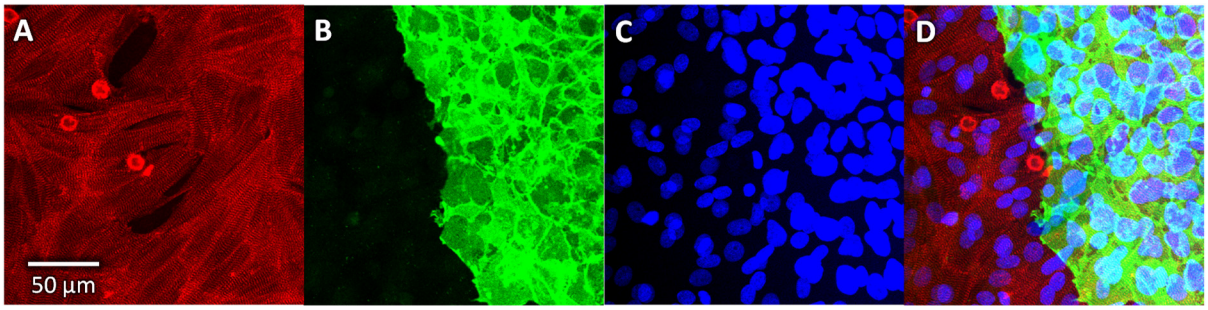

Figure 33. Confocal image of cluster on cardiomyocytes.
A. α-actinin **B.** ChR2 **C.** DAPI **D.** Superimposed stains.

Acute pacing experiments

Phase contrast imaging during acute pacing showed that we could pace-capture the CMs at up to 2 Hz. To test if the optically initiated activation could point-pace the entire monolayer, we optically recorded APs across the monolayer. While a spontaneous AP originated from the edge of the monolayer (Figure 34Aa, 946 ms), the optically-triggered AP originated from the location of the spark cluster (Figure 34Aa, 2640 ms), as identified by the bright background fluorescence signal (Figure 34B). The AP then propagated from the spark throughout the entire monolayer, as shown by the activation map (Figure 34C).

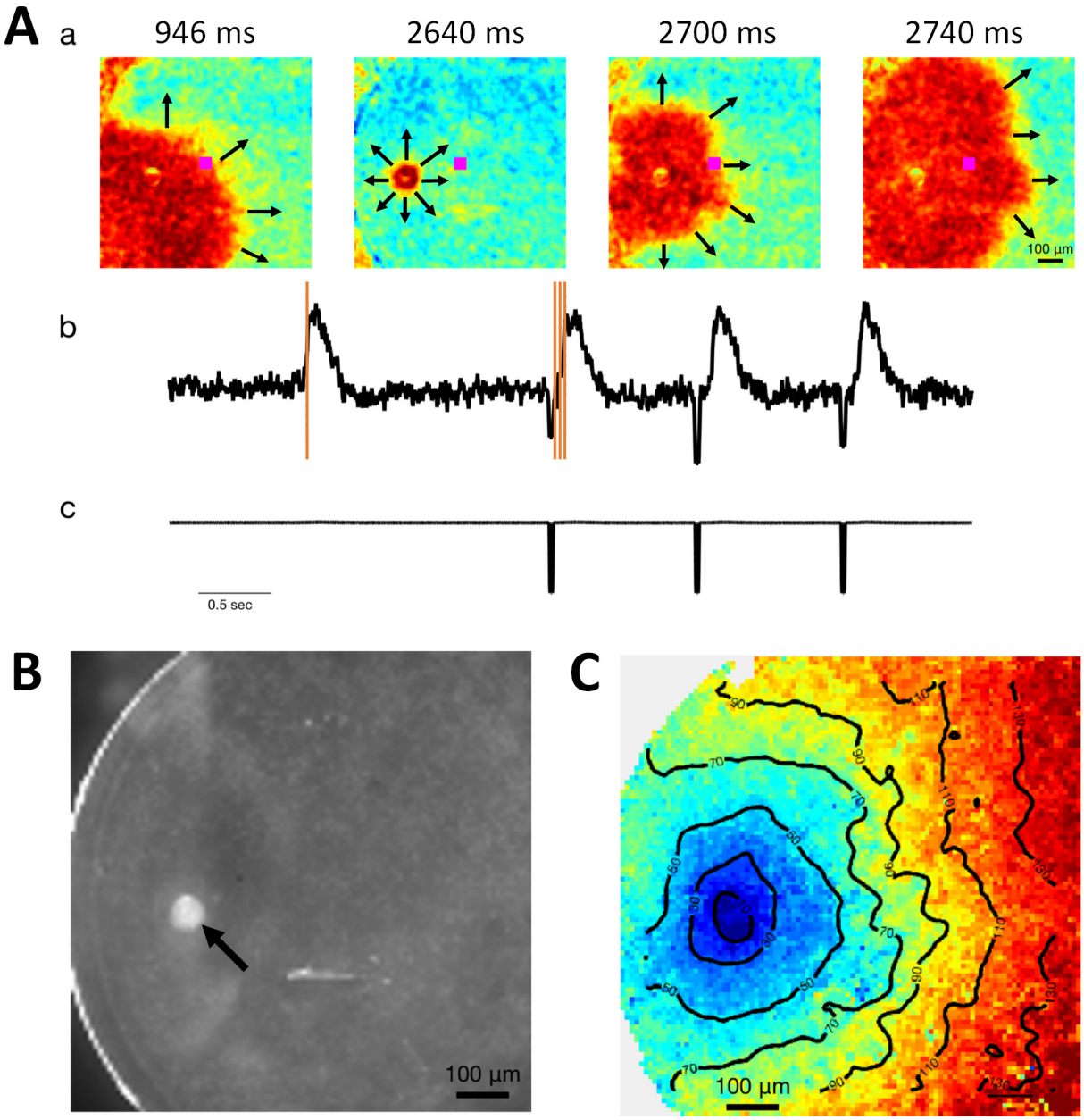

Figure 34. Optical mapping of optically-paced cardiomyocytes.
A a. Membrane potential across the NRVM monolayer at different time points. Red indicates depolarized cells; blue and green indicate cells at rest. **b.** Optical APs recorded from the center of the field of view (purple box in Aa). Orange lines correspond to the time points where the snapshots in Aa were taken. **c.** Recording of the stimulating light. **B.** Background fluorescence image of the NRVM monolayer. Arrow points to spark cluster (seen as white dot, due to clustering of fluorescing cells). **C.** Activation map and isochrones (20 ms spacing) of an optically paced AP. From Dr. Renjun Zhu.

Chronic pacing experiments

Using our in-incubator microscope and optical pacing system, we took baseline recordings before optical pacing and found a mean beating rate of 43 BPM, with extensive CL variability sample to sample, and sometimes even within single samples over a 30 s interval (Figure 35). However, we found we were able to pace-capture our cells inside an incubator using our optical pacing system (Figure 36). Time lapse imaging of coverslips before and during pacing allowed us to determine capture over 30 s intervals over 6 hours (Figure 37A). Capture at 60 bpm with optical pacing was achieved in 3 of 5 NRVM cultures, with a fourth capturing intermittently. The three captured samples maintained capture for at least 4 hours (Figure 37A). Well-to-well variability (SD) of beating rate increased from 3.3 BPM before pacing to 8.0 BPM after, since only some samples captured. Histograms of cycle length before and during pacing showed significant variability in inter-beat interval (IBI), while the captured samples beat both faster, at 1 Hz, and more regularly (Figure 37B). This is clearly demonstrated by plots of mean CL and standard deviation of cycle length before and during beating (Figure 37C and D). Furthermore, even the coefficient of variation is reduced in the captured samples, despite the shorter IBI (Figure 37E). Interestingly, in the case where capture was intermittent, the SD and COV of IBI was higher than it was before pacing (Figure 37E and F). To isolate the effects of pacing capture, we only included samples during pacing before any significant dropout of previously capturing samples, as marked by an orange bar in Figure 37A.

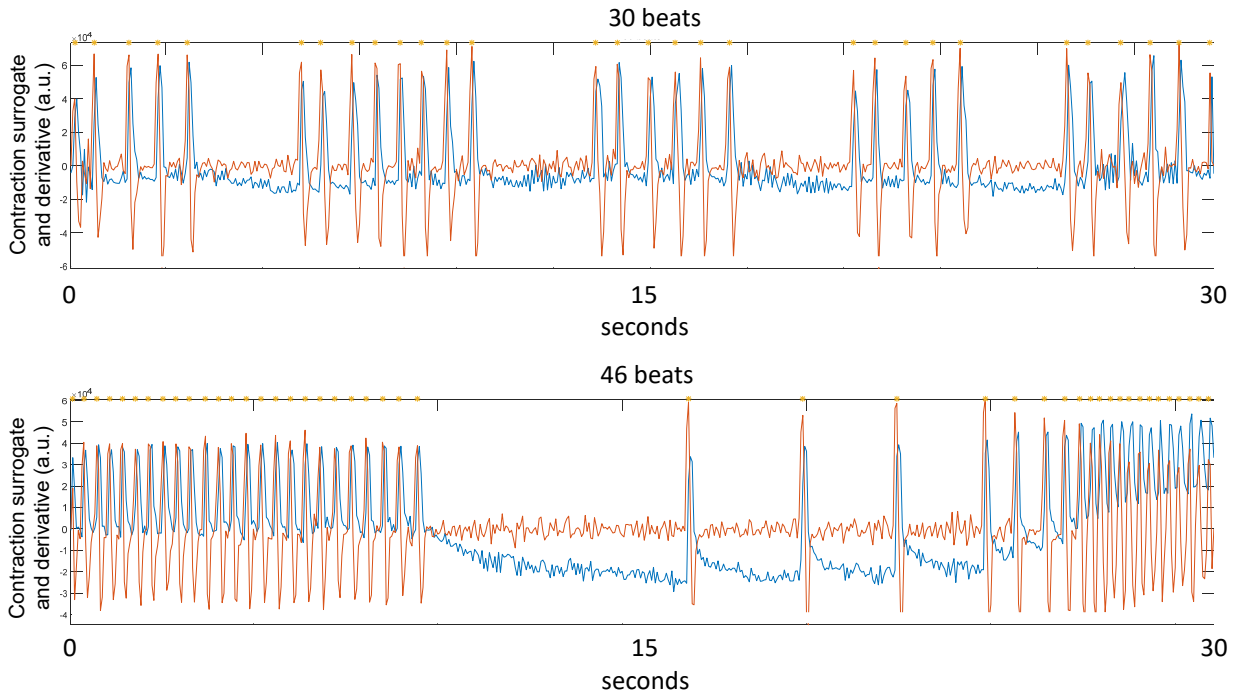

Figure 35. Beating variability in unpaced NRVMs.
Two examples of beating in unpaced NRVMs. The blue trace shows contraction surrogate and the orange is its derivative. Along the top of the plot, yellow asterisks indicate a detected beat.

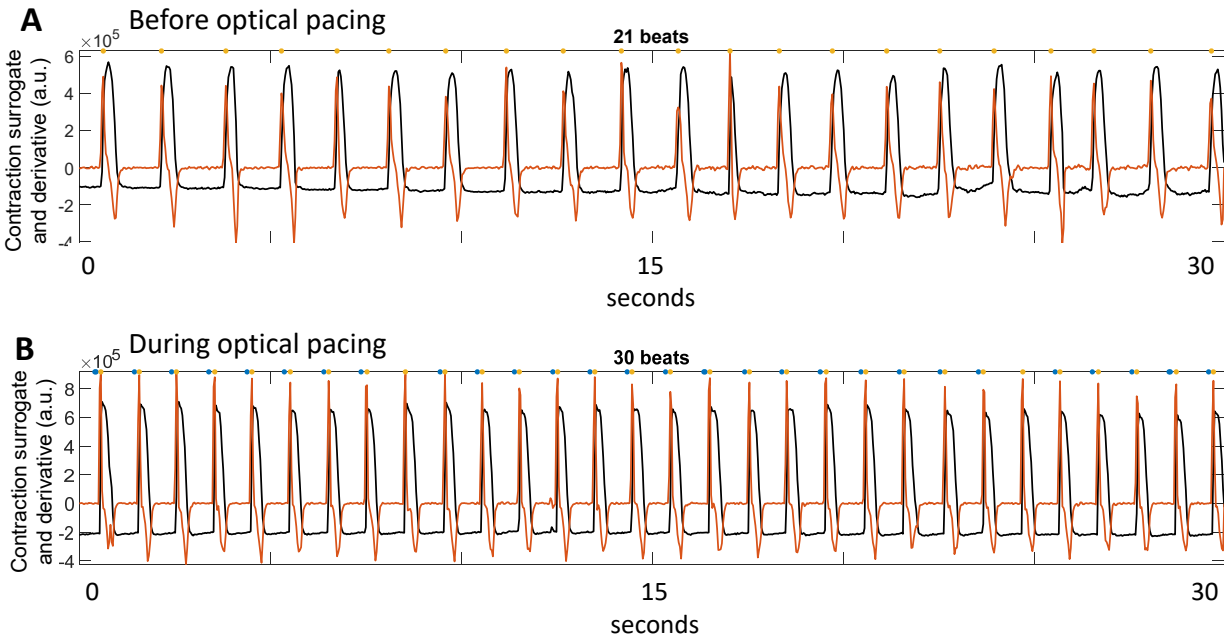

Figure 36. Optical capture of NRVMs.
Traces of contraction before (**A**), and during (**B**) 1 Hz optical pacing. The black trace shows contraction and the orange is its derivative. Along the top of the plot, blue markings indicate each light pulse and yellow markings indicate capture.

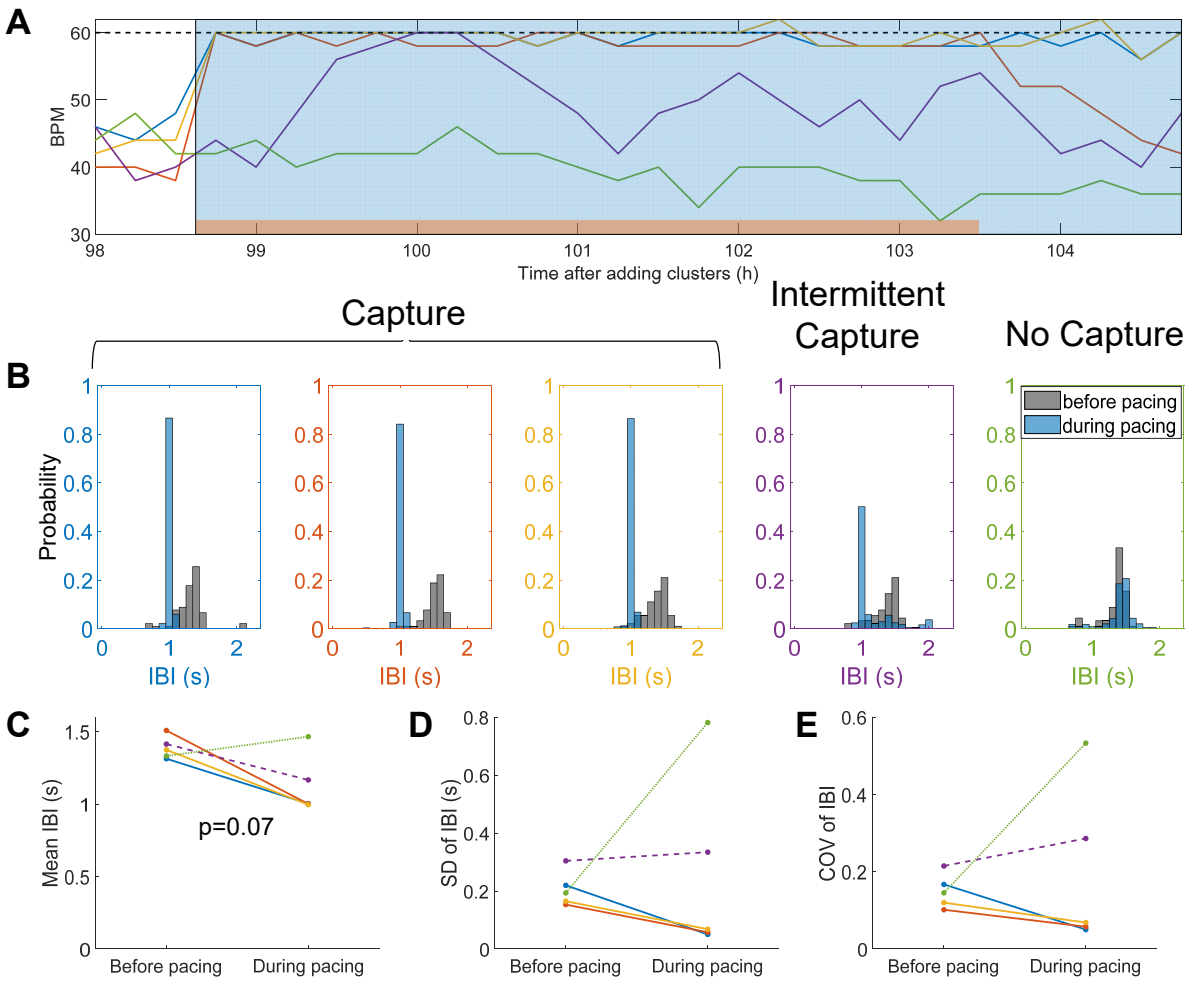

Figure 37. Chronic optical pacing of NRVMs.
A. Beating rate over time for multiple samples. Blue rectangle shows optical pacing. Orange rectangle shows times analyzed for during pacing group in **B-E.** Black dashed line is paced rate. **B.** Histograms of beating rate show distribution of inter-beat intervals (IBI) before and during pacing. Axes colors correspond to the samples in **A** and **C-E**. **C-E.** Mean of IBI (**C**) SD of IBI (**D**) and COV of IBI (**E**) before and during pacing. Solid lines denote electrically captured samples, dashed shows intermittent capture, and dotted shows no capture. Colors correspond to the samples in **A** and **B**.

To see if our spark cluster method could pace a more clinically relevant cell type, we attempted to use them to pace hiPSC-CMs with a mutation for arrhythmogenic right ventricular dysplasia. Baseline recordings before optical pacing showed a mean beating rate of 37 BPM. All four samples could be paced at 60 BPM, but unlike NRVMs lost capture after approximately an hour (Figure 38A). Histograms revealed less consistent

IBI than NRVMs even while cells were nominally capturing, indicating some level of continued missed or early spontaneous beats (Figure 38B). As expected, pacing significantly reduced IBI to 1 Hz (Figure 38C). Because every well was successfully captured, well-to-well standard deviation of beating rate decreased from 4.1 BPM before pacing to 1.5 BPM after. Pacing also reduced SD and COV of IBI, as seen in captured NRVMs (Figure 38D and E). As with NRVMs, we only included samples during pacing before any significant dropout of previously capturing samples, as marked by an orange bar in Figure 38A.

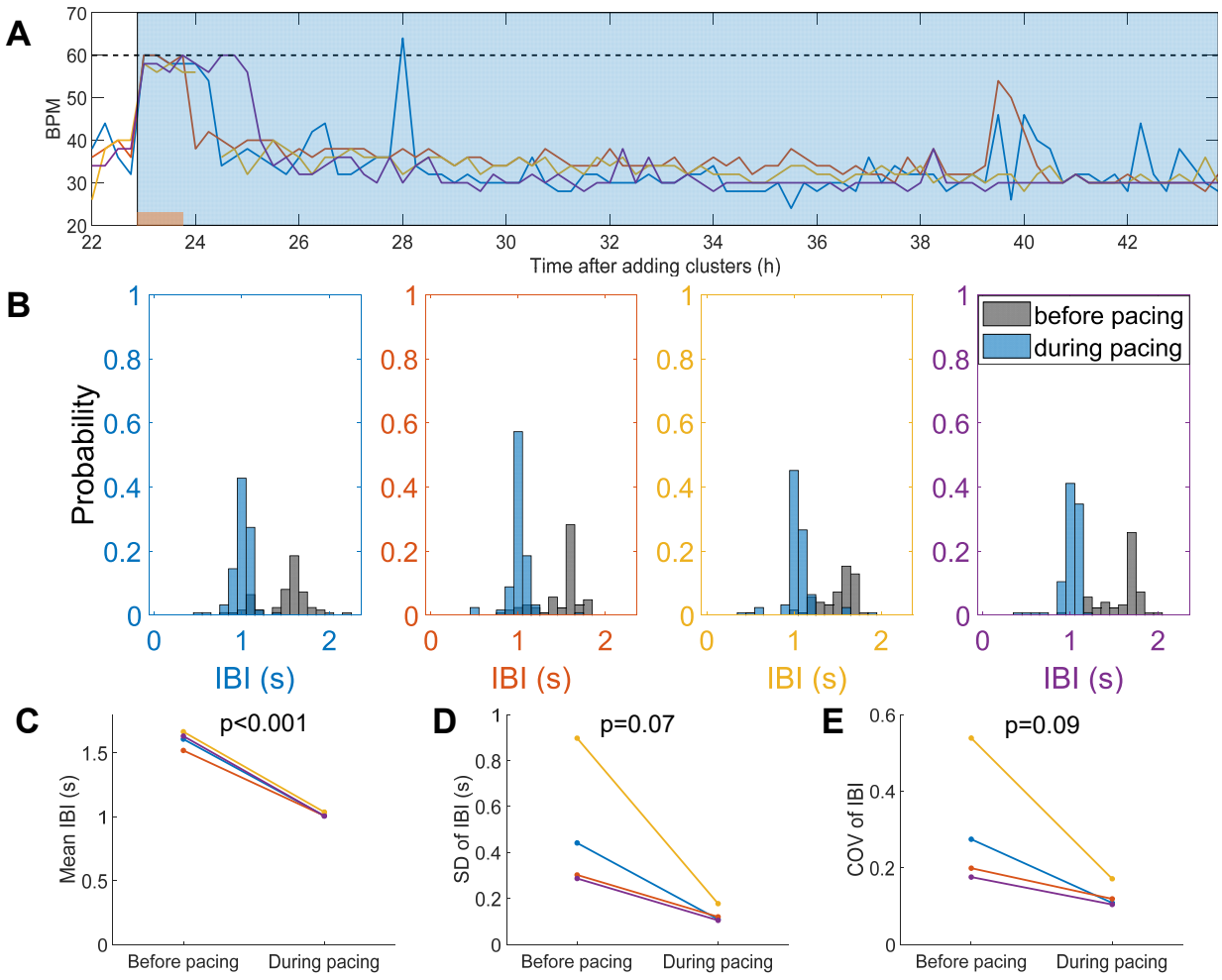

Figure 38. Chronic optical pacing of hiPSC-CMs.
A. Beating rate over time for multiple samples. Blue rectangle shows optical pacing. Orange rectangle shows times analyzed for during pacing group in **B-E.** Black dashed line is paced rate. **B.** Histograms of beating rate show distribution of beating rates before and during pacing. **C.** Mean cycle length before and during pacing. **D.** Mean standard deviation of cycle length during each 30 second recording before and during pacing. **E.** Mean coefficient of variation before and during pacing.

Cx43-transduced spark cells

To try to improve pacing consistency, we transduced spark cells with GFP-Cx43. Using fluorescence-assisted cell sorting, we found that although GFP+ only cells had bleed-through into the YFP channel (Figure 39C), there was almost no bleed-through of YFP into the GFP channel (Figure 39B). Since we knew that almost all our cells were

YFP (ChR2) positive, since they were a stably transfected cell line, we only had to be able to differentiate cells that were also GFP (Cx43) positive, making the GFP bleed-through into the YFP channel irrelevant. Therefore, we were able to identify spark cells that were transduced with Cx43 by GFP signal (Figure 39D) in excess of YFP-only cells (Figure 39B) and collected the highly doubly-transduced (Hi DP) population for further analysis. qPCR confirmed increased expression of Cx43 by a factor of 23 (95%CI = 5.6-98). However, live cell imaging of Cx43-transduced spark cells showed decreased GFP/YFP (the signals can't be separated since the wavelengths are similar) compared to spark cells, suggesting interference with ChR2 expression, possibly due to cell stress (Figure 40), so these cells were not used for further study.

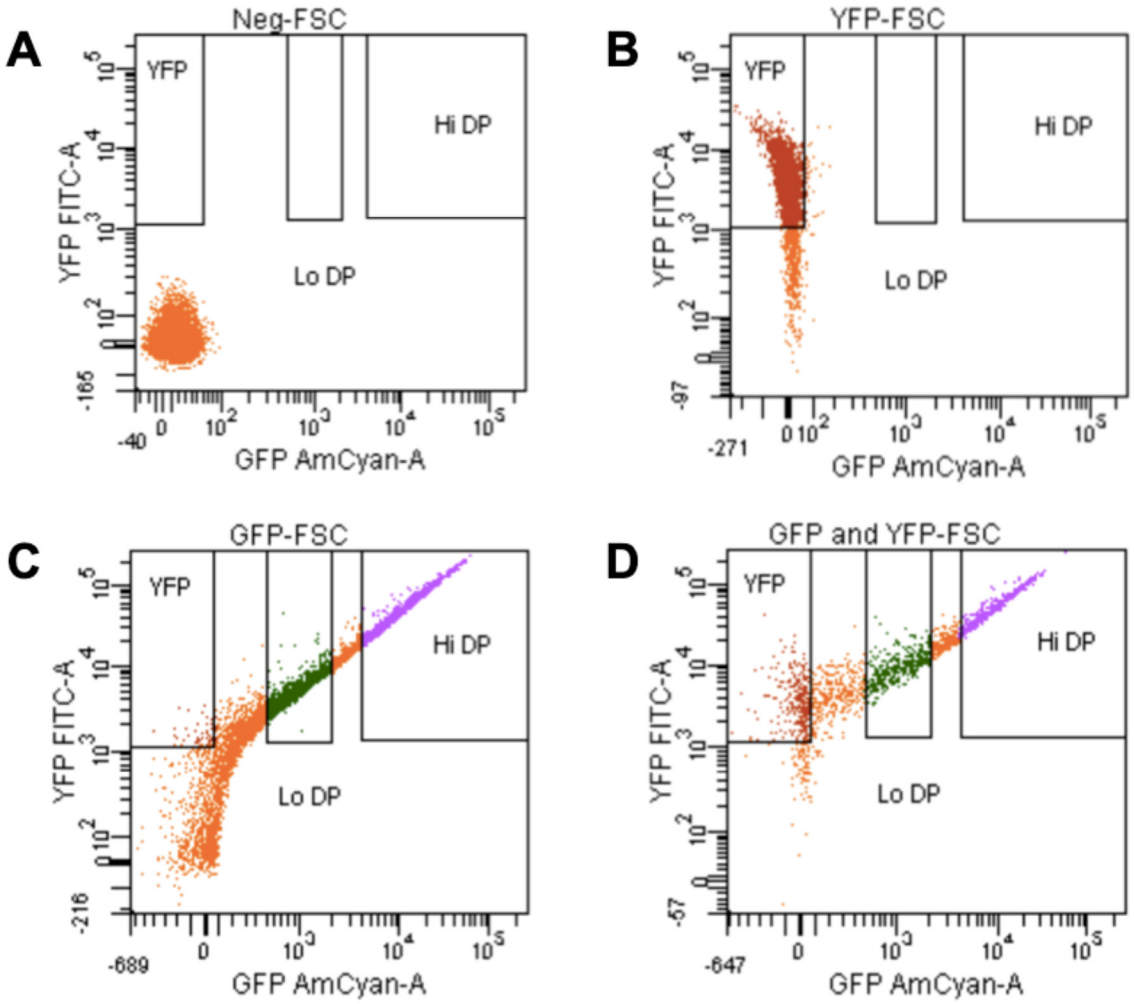

Figure 39. Fluorescence-activated cell sorting of Cx43/ChR2 positive cells.
YFP fluorescence along y-axis shows ChR2 transduction, while GFP fluorescence along x-axis shows Cx43 transduction. Boxes show YFP+, GFP- cells, YFP+, low GFP+ cells, and YFP+, high GFP+ cells. **A.** Naïve HEK-293 cells (YFP/GFP negative). **B.** spark cells (YFP-positive) **C.** Cx43-transduced HEK-293 cells. **D.** Cx43-transduced spark cells. From the Johns Hopkins Flow Cytometry Core. YFP box corresponds to cells considered to express YFP only (brown). Lo DP refers to cells expressing YFP and a low amount of GFP fluorescence (green). Hi DP refers to cells expressing YFP and a high amount of GFP fluorescence (purple). Hi DP cells were collected and used for further analysis.

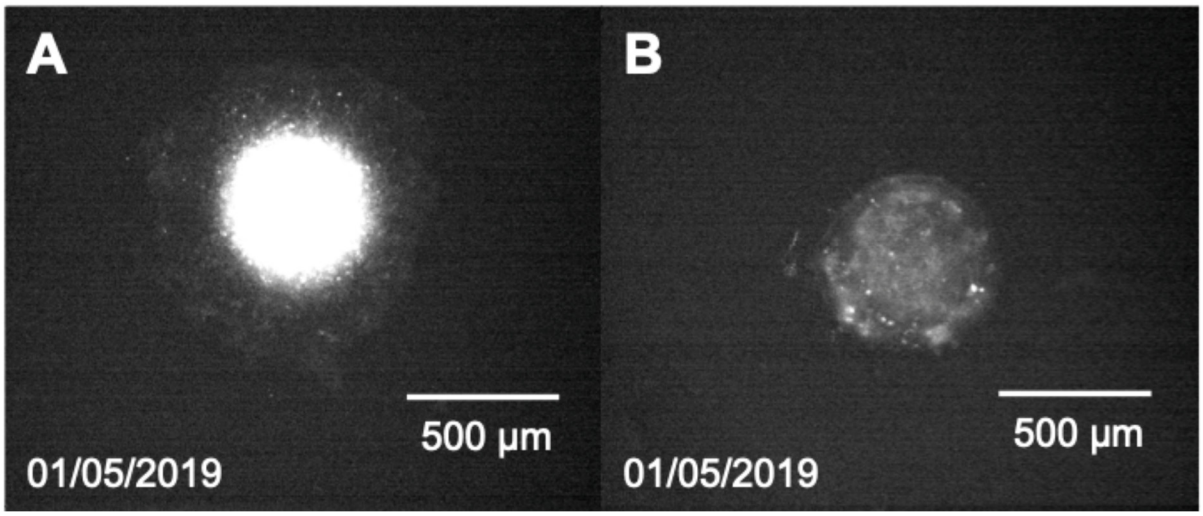

Figure 40. Fluorescence images of transduced and untransduced spark clusters.
A. Control spark cluster **B.** Cx43-transduced spark cluster. From Shivani Pandey.

Discussion:

While a number of groups have used optogenetics to pace cardiac tissue [128], including for up to 2 hours *in vivo* [8], only recently has an opsin been used to pace CMs chronically *in vitro*, where it may be used to mature cells [171]. That study found that pacing for one week starting at day 7 in hiPSCs increased spontaneous beating rate, maximum capture rate, and rate of force development, while reducing force drop-off at higher pacing rates. However, they used custom-made culture plates that required an LED for each well, while we used a single commercially available LED panel, with the capability to stimulate multiple off-the-shelf plates. Also, while they, as well as many others using electrical stimulation, used field pacing to mature cells, this creates the unnatural condition of forcing all cells in the tissue to contract simultaneously against each other, preventing them from undergoing physiological length changes that are likely important for mechano-electric feedback [173]. While deformable membranes on deformable anchors have mitigated this issue somewhat by allowing for length changes

during contraction and led to improved maturation by pacing ([102, 104, 174, 175], see Chapter 1 for more detail), the fact remains that the heart itself is not field paced, and instead contracts sequentially, resulting in stretching before and after an individual cell has an action potential, which may be important for proper gene expression and function. This is supported by data studying cardiac resynchronization therapy mechanisms that found marked “reverse remodeling” in hearts from dogs treated with resynchronization therapy (which alters the timing of activation) after artery ligation and rapid pacing to mimic heart failure, even in the absence of significant improvement in ejection fraction, suggesting the activation timing itself may play an important role [176]. A number of studies have attempted to create electromechanical bioreactors, in which cultured cells are both electrically paced and cyclically stretched, with the hope of investigating the effects of combined electrical and mechanical stimulation [177–180]. More recently, some studies have varied the timing of electrical and mechanical stimuli to investigate how electromechanical delay affects cellular function, and shown that this changes gene expression [181, 182]. One study attempted to mimic the pre-stretch that occurs *in vivo* by combining mechanical stretching and electrical pacing and found increased SERCA2 and cTnT versus other groups, including synchronous electrical and mechanical stimulation providing further evidence that timing of contraction affects gene expression and proper cardiac function [183]. Chronic point pacing may provide the same effect more simply, but has only been attempted in one pilot study [184].

Therefore, we chose to use clusters of spark cells, rather than “sprinkling” them onto or directly transducing CMs, as has been done previously [9], because it allows us to, with a simple global application of light, point pace cells, which is more similar to

what occurs *in vivo* in a way that may be important for maturation [10], and is difficult to do electrically at scale [11]. Furthermore, it is an improvement over other optogenetic stimulation methods because it only perturbs the CMs in a small region (Figure 34B), while the paced AP can propagate across and activate the entire tissue (Figure 34C). While others have narrowly focused light to optogenetically point pace acutely [185, 186], none of them have done so chronically for maturation, and this method requires direct transduction of CMs and is less scalable. Our technique should make chronic *in vitro* point pacing of CMs simpler, since pacing requires no contact or manipulation once the cluster is placed, the clusters are straightforward to manufacture, and a single commercially available LED panel may be used to stimulate entire plates of cells.

We chose our pulse width to be that which required the minimum power to stimulate, and the brightness to exceed the pacing threshold (~0.04 mW/mm^2 at 20 ms), based on previously published measurements [9]. In addition to increasing the beating rate to help mature CMs (Figure 37 and Figure 38), we also hoped to reduce both well-to-well and temporal variability in beating rate to create more reproducible results. While we were able to do this in hiPSC-CMs since all wells captured (Figure 38), in NRVMs, where some wells only captured intermittently or not at all (Figure 37B-C), well to well (Figure 37B) and temporal (Figure 37E-F) variability actually increased, demonstrating the importance of further work to attain more consistent capture. Furthermore, in our hiPSC-CM experiments, we lost capture after only an hour. Whether this was caused by metabolic insufficiency, calcium dysregulation, or changes in protein phosphorylation or gene expression, and whether these are due to the disease phenotype of our cells, or the immaturity of our hiPSC-CMs remains to be studied in future experiments.

Conclusion

We have developed a straightforward method to leverage optogenetics to chronically pace CMs *in vitro*. While much work remains to be done, this technique holds the promise of increasing maturation and reducing variability of CMs, and the ability be easily implemented and scaled up to stimulate many samples in parallel.

Acknowledgements

This study was conducted in the laboratory of Dr. Leslie Tung, with Dr. Renjun Zhu, and undergraduate researcher Shivani Pandey, as well as input and materials from Dr. Emilia Entcheva. It was supported by NIH grant R01 HL127087. Confocal imaging was supported by NIH grant S10 RR024550 (Scot Kuo). This work has appeared in abstract form [187], as well as a poster presentation at the 2019 Biophysical Society Annual Meeting.

Chapter 5: Engineered heart slices for electrophysiological and contractile studies

Introduction

The applications of tandem cell units described in the previous chapters use monolayers of CMs, but the results would be stronger if they were performed on a system that better represented the properties of the intact heart. For example CFB differentiation is significantly affected by ECM stiffness [118–120] and composition [121, 122]. Various strategies have been employed in the fabrication of functional cardiac preparations that mimic native myocardium [188, 189]. However, significant challenges remain in the ability of present engineered tissues to recapitulate the complex biochemical and biomechanical environment in native myocardium. Decellularization of whole organs can provide a natural scaffold that can be repopulated with a variety of cell types. Decellularized myocardial matrix has been successfully obtained by whole-heart perfusion [111, 116] or through treatment of mm-thick sections of myocardium [190], and shown to provide a biocompatible substrate for cellular attachment while largely preserving matrix composition, organization, and mechanical properties. CMs cultured on this native matrix survive [114, 191], contract [190], and respond to electrical stimulation [111, 115, 117]. Thus, decellularized myocardium is proving advantageous for the maintenance of CMs and is receiving increasing attention as a scaffolding material for cardiac tissue engineering. Despite this progress, recellularization of three-dimensional native tissue remains a challenging proposition, particularly in the whole organ. On the other hand, recellularization of smaller and thinner tissues should be

easier to achieve. With this approach in mind, our objective was to develop a physiological tissue system that supports CM survival and organization at confluent densities, contracts, and exhibits electrical conduction, anisotropic properties, and tissue-level arrhythmias.

Methods

Preparation of decellularized slices

Cylindrical plugs of myocardial tissue were punched out of the excised left ventricle of hearts from slaughterhouse pigs using a 14 mm or a 16 mm-diameter hollow metal punch (Mayhew, Turner Falls, MA). Plugs were stored at -80°C until sectioning, for a minimum of 16 h. To obtain sections for decellularization, plugs were partially thawed, and an epicardial portion ~1 cm thick was cut out, embedded in agarose, and glued to the cutting stage with cyanoacrylate. Slices 300 μm thick were then sectioned using a vibratome equipped with a ceramic blade vibrating at a rate of 100 Hz, amplitude of 1 mm, and advancing at a speed of 0.01 to 0.03 mm/sec. The cutting solution was UltraPure water (Invitrogen, Carlsbad, CA) chilled to 4°C (Specimen Bath Cooler 7610, Campden Instruments), with 1% antibiotic-antimycotic (Gibco, Gaithersburg, MD) and 1% penicillin/streptomycin (Life Technologies, Grand Island, NY). All tools in contact with the tissue or solutions were sterile. Slices were stored at 4°C in PBS or HBSS overnight prior to decellularization. In this report, "native" slices refer to tissue slices prepared in this way and remaining in PBS instead of undergoing decellularization.

Slices were decellularized by a procedure modified from Ott et al [111]. Slices were placed in wells of a standard 12-well culture plate and treated with 1 mL of each of

the following solutions (diluted in UltraPure water, where applicable) while being rotated at 150 rpm on an orbital shaker: 2 washes of 1% SDS (Life Technologies) for 1.5 h each, 1 wash of water for 15 min, 1 wash of 1% Triton X-100 (Sigma-Aldrich) for 7 min, and 3 washes of PBS or HBSS for 15 min each. Afterwards, decellularized slices were left in PBS or HBSS to rotate at 110 rpm on an orbital shaker overnight. All detergents, wash, and storage solutions were supplemented with identical concentrations of antibiotics and antimycotic as in the cutting solution. Plastic coverslips 14 mm in diameter were sterilized by rinsing in 70% ethanol and exposing to UV for 10 min. The decellularized slices were then carefully spread on the coverslips with the outer perimeter of the slice hooked around the edges of the coverslip. Coverslips with affixed slices were placed in 15 mm-diameter wells of standard 24-well culture plates and kept in sterile PBS or HBSS until use.

Seeding of decellularized slices with neonatal rat ventricular cells

All animal procedures were performed in compliance with guidelines set by the Johns Hopkins Committee on Animal Care and Use and all federal and state laws and regulations. Cell culture media consisted of Medium 199 (Gibco) supplemented with 1% HEPES buffer solution (Gibco), 1% MEM non-essential amino acids (Gibco), 20 μM glucose (Sigma-Aldrich), 2 mM L-glutamine (Life Technologies), 4 μg/mL vitamin B-12 (Sigma-Aldrich), 1% penicillin/streptomycin (Life Technologies), and a variable amount of FBS (Life Technologies). The hearts of 2-day-old Sprague-Dawley rats (Harlan, Indianapolis, IN) were excised, cut into 4-6 pieces, rinsed twice in HBSS, placed in 40 mL 0.25 mg/mL filtered trypsin (Affymetrix, Cleveland, OH) in HBSS solution in a sealed glass container, and rotated at 110 rpm at 4°C overnight (13-16 h). The next day as

much trypsin solution as possible (without removing cells) was pipetted out, and the remainder quenched by adding 25 mL 10% FBS media. The tissue was rotated at 150 rpm in a warm water bath for 3 min. Then, excess media was removed, and 9 mL of 1 mg/mL collagenase (Worthington, Lakewood, NJ) in HBSS was added before sealing the glass container holding the tissue and placing it back in the warm water bath for 3 min. After this, excess solution was removed and discarded. Another 9 mL of collagenase solution was added, the glass container was sealed and rotated in the warm water bath again for 3 min, the cells were pipetted up and down three times, and the excess solution was removed and placed in a 15 mL centrifuge tube with 4 mL cold HBSS, which was placed in ice to quench the collagenase activity. This was done 3 more times. The tubes were centrifuged at 3,000 rpm for 8 min, excess solution was aspirated, and the cells were pipetted out into 10 mL of cold HBSS. They were then triturated by pipetting before being passed through a 40 μm nylon cell strainer (BD Falcon, Franklin Lakes, NJ). The cells were then centrifuged again for 5 min at 1,000 rpm and 1 min at 3,000 rpm, before aspirating out the HBSS, resuspending in 15 mL 10% FBS media with 1% antibiotic-antimycotic, and preplating for one hour in a 75 cm^2 flask (Sarstedt, Newton, NC) to remove CFBs. They were then preplated again in 25 mL 10% FBS media in a 175 cm^2 flask (Sarstedt) without antibiotic-antimyoctic for one hour, before being counted using a hemocytometer (Thermo Fisher Scientific, Hampton, NH). Two million NRVMs were added to each slice to form an EHS. Day 0 of culture was defined to begin at the time of NRVM plating. After 18 h, EHS were washed with warm PBS, and fresh media with 10% FBS was added. On day 2, serum in the culture

medium was reduced to 2% to inhibit non-CM proliferation, and cells were fed with 2% serum every other day thereafter.

DNA isolation and quantification

Native and decellularized slices were dried in a dessicator and weighed. Since the decellularized slices weighed much less than the native slices, ten decellularized slices were combined for more accurate weighing and DNA quantification. They were digested in 500 µL Tris EDTA containing 1% SDS and 1% Proteinase K (Qiagen, Venlo, Netherlands) by volume at 52°C overnight. 500 µL of phenol/chloroform/isoamyl alcohol (Sigma-Aldrich) was added, and the sample was shaken and centrifuged 10 min at 15,000 rpm. The supernatant was removed and placed in a new tube to which 50 µL 3M sodium acetate (Ambion, Life Technologies) and 1000 µL of 100% ethanol were added. This was frozen overnight at -20°C to precipitate the DNA, thawed, and centrifuged 10 min again to pellet the DNA. The liquid was removed, and the tube was washed with 70% ethanol and centrifuged 5 min. Finally the ethanol was removed, and the remaining DNA pellet was suspended in 50 µL Tris EDTA. DNA content was quantified by measuring absorbance in a spectrophotometer (NanoDrop 1000, NanoDrop Products, Wilmington, DE).

Tissue characterization

Native and decellularized slices were frozen at -20°C in optimal cutting temperature media (Sakura, Torrance, CA), and 10 µm-thick cross-sections were cut every millimeter with a cryostat (CM3050S, Leica, Wetzlar, Germany). These sections were imaged using a CCD camera (SensiCAM, Cooke Corporation, Romulus, MI) under a phase contrast microscope. Multiple images were taken of each slice and stitched

together manually to image a large field of view with detail by undergraduate Jourdan Ewoldt. The cross-sectional thickness was measured using a custom MATLAB script. Only sections from each slice that were straight, with little bunching or breaks, were used for thickness analysis.

Slices of native and decellularized ECM were imaged using second harmonic generation (SHG) by a multiphoton microscope (model 710NLO, Zeiss, Oberkochen, Germany) with excitation at 880 nm, and emission acceptance at 415-450 nm.

To image cell survival in EHS, a viability/cytotoxicity kit (Invitrogen) was used to stain live and dead cells in the EHS seven days after plating. After removal of culture medium, EHS were rinsed with PBS and incubated in 1.4 μM calcein-AM and 4 μM ethidium homodimer-1 (EtD) in PBS for 25 min at 37°C and imaged using a fluorescence microscope.

Live/dead staining was also done in combination with SHG microscopy to image collagen organization relative to cells. Calcein was imaged by excitation at 488 nm and emission at 490-540 nm, and EtD was imaged using 543 nm excitation with 600-650 nm emission. In some experiments, the cells were incubated in the cell-permeable nuclear dye DRAQ5 for 5 min instead of EtD to image nuclei of live cells. A z-stack of images was created, and the intensity of above-background signal for calcein, DRAQ5 and SHG at each z-level was normalized to the overall peak intensity for each stain and plotted using a custom MATLAB script. Additionally, the z-stack was thresholded and colored according to depth using ZEN blue edition (Zeiss) to visualize cellular overlap.

Immunostaining

Immunostaining and imaging were performed by Dr. Adriana Blazeski. EHS samples were fixed in 4% paraformaldehyde, sometimes immediately after optical mapping. EHS samples were permeabilized by applying 0.2% Triton X-100 (Sigma-Aldrich) for 5 min and blocked using 10% goat serum (Life Technologies) in PBS for 25 min at room temperature. Primary antibodies against cardiac troponin I (US Biological, Salem, MA), α-actinin (Sigma-Aldrich), vimentin (Dako), and connexin 43 (Sigma-Aldrich) were diluted in Antibody Diluent (Dako).

EHS were incubated in primary antibodies overnight at 4°C, then washed three times with TBS-T (10% TBS and 0.05% Tween 20 in ddH_2O) for 5 min each. Samples were subsequently incubated with a 1:200 dilution of Alexa Fluor-conjugated goat secondary antibodies in antibody diluent (Invitrogen) for 1 hour at room temperature, followed by DAPI (30 μM in PBS) for 25 min. Finally, samples were washed again three times with either DPBS (ECM) or TBS-T (EHS) and mounted on microscope slides using ProLong Gold Antifade (Invitrogen). Immunofluorescence images were obtained using a confocal microscope (LSM 510 Meta, Zeiss). A similar protocol was performed (without secondary antibody incubation or wash) on slices of native and decellularized ECM, with staining using DAPI and phalloidin.

Calculation of nuclear elongation and alignment

Confocal images of EHS stained with DAPI were thresholded above the noise level, and overlapping nuclei were segmented using a previously described method [192], with some changes. First, the concavity points were searched for recursively, such that when a concavity point was found, the outline between it and the convex hull

were searched for additional concavities. Second, the case where non-adjoining sections of outline were part of the same nucleus was allowed. Ellipses were fit using a previously described method [193]. Additional checks, such as a minimum area of 25 μm^2, overlap with other nuclei of no more than 40%, and minimum area in fitted ellipse that is above threshold of 70% were employed. The closest fit matching these parameters was used, and the mean angular orientation and standard deviation was calculated using a previously described method [194].

Contraction measurement

To characterize spontaneous contraction in EHS over time, EHS were removed from the incubator daily (before feeding on days they were fed) and immediately placed on an inverted microscope for viewing. It was then recorded whether each EHS contracted at least once within a 10 second period. If it did contract, it was recorded whether the entire 0.55 mm^2 field of view contracted simultaneously, or if there were patches beating asynchronously. To characterize the amount of contraction, EHS were placed on a 37°C heated stage (Warner Instruments, Hamden, CT) in a 35 mm dish filled with the Tyrode's solution. A section of the EHS was unhooked from the coverslip so that it could move freely. The EHS was paced at 1-5 Hz, and the free region was imaged by a CCD camera (Swiftcam, Swift, Schertz, TX) at a frame rate of 25-125 fps with 600x480 pixel resolution and a 3.07 mm^2 field of view, such that the free edge of the slice was approximately vertical in the rectangular field of view. A custom MATLAB script was used to segment the image and calculate the mean displacement of the EHS over time by dividing the change in slice area by the height of the field of view. The mean displacement during each contraction at each pacing rate was calculated and

used as a surrogate for contractility to measure the force-frequency relationship of the EHS. Although in some cases the EHS would beat spontaneously or not be captured by an electrical stimulus, only the amplitudes of beats with a previous beat preceding it by the set pacing interval were used in analysis.

Electrophysiological studies

Most EHS were optically mapped 5 to 8 days after seeding. Some EHS were mapped 21 days after seeding. EHS were optically mapped using a custom-built 256 channel photodiode array and protocol described previously [129]. Briefly, EHS were placed in the mapping chamber and treated with 20 μM di-4-ANEPPS and 10 μM blebbistatin in Tyrode's solution for 10 min. Tyrode's solution (35±1°C) containing 10 μM blebbistatin was continuously recirculated through the chamber for the duration of each experiment to inhibit motion artifacts. The stimulus voltage threshold was determined at 2 Hz, and a voltage 10% higher was used for experiments. Each EHS was recorded during pacing at increasing rates (1 to 5 Hz, and then decreasing the cycle length (period) by 20 ms, then 20 ms, and then 10 ms steps thereafter) until it lost capture, had significant wavebreaks, or created a reentrant wave. Before each recording, at least 25 stimulus pulses were applied to allow the tissue to reach steady state at the new pacing rate.

For drug studies, 90 μM, 180 μM, and 360 μM solutions of lidocaine were made and superfused over the EHS for at least 15 minutes before measurements were taken as described above. They were paced at 2 Hz during the last 5 minutes of solution flow (600 beats), which has been shown to be long enough to allow lidocaine binding to

reach steady state [195]. Lidocaine, di-4-ANNEPPS and blebbistatin were all dissolved in DMSO. The concentration of DMSO in the bath never exceeded 0.5%.

Optical mapping signals were preprocessed using a custom Matlab script as described in Chapter 2. The isochronal activation map of a perfectly homogeneous anisotropic tissue that has been point stimulated should be a series of equally spaced ellipses (disregarding nonlinearities due to rapid changes of wavefront curvature near the pacing site) [58]. In x-y-t space this forms a right ellipsoidal cone, which we fit to our data by iteratively optimizing the ellipsoidal cone parameters to minimize the sum of the squared distance between each data point and the cone [196]. CV in the longitudinal and transverse directions were calculated as vectors (position, direction, and magnitude) starting at the vertex of the cone with directions along the major and minor axes of the ellipsoid and magnitudes equal to the reciprocal slope of the cone along the major and minor axes, respectively (Figure 41). APD at 30 and 80 percent repolarization (APD_{30} and APD_{80}) were also calculated from the optical voltage signal.

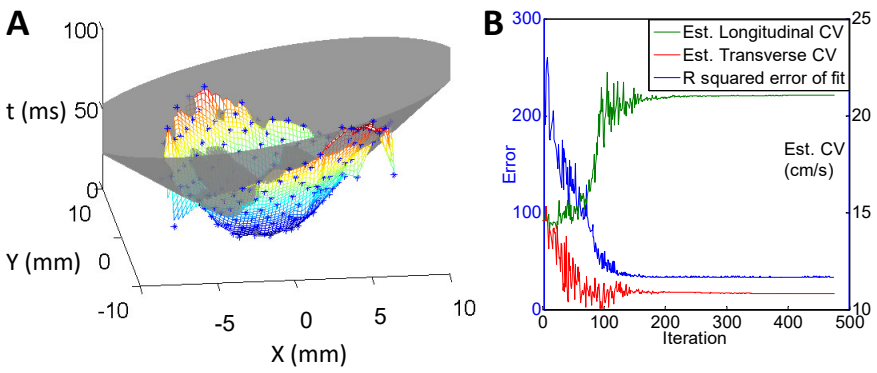

Figure 41. Calculation of conduction velocity.
A. CV was calculated by plotting activation maps in x-y-t space and fitting the activation times to an elliptical cone. Data shown here is for the activation map in Figure 47. **B.** Parameters of an ellipsoidal cone were iteratively optimized to minimize the total squared distance between each data point and the cone (blue line). The reciprocal of the slope of the cone along the major and minor axes was used to determine CV along the fast (longitudinal) and slow (transverse) axes (green and red lines, respectively). The vector directions for CV were taken to be along the major and minor axes of the cone, and their origin to be at the vertex of the cone.

Statistics

All data are presented as mean±SD, except when stated otherwise. Anisotropy ratio and nuclear elongation (length-to-width ratio) were log transformed to make them more normally distributed since they were right-tailed. They were expressed as the log-transformed mean as well as the interval of the log-transformed mean plus or minus one SD, after inverse transformation back into linear space, as discussed in [197]. Paired t-test was used for statistical significance between experimental groups, except when data were normalized and then compared to control (Figure 46D, Figure 47C,D), in which case an unequal variance t-test was used to compare them to 1. Differences were considered statistically significant at $p<0.05$.

Results

Preparation of thin decellularized slices of extracellular matrix

Slices of ECM were prepared from left ventricles of pig hearts (Figure 42A). The tissue was frozen, cut as 14 or 16 mm-diameter plugs, and a 1 cm-deep epicardial portion was cut out and embedded in agarose in a 35 mm dish (Figure 42B). These tissue plugs were then sectioned into 300 µm-thick slices (Figure 42C) and decellularized by SDS and Triton X-100, becoming nearly transparent (Figure 42D). Slices of decellularized ECM did not maintain their shape when lifted out of liquid. To allow for easy handling and cell seeding, each slice was carefully spread over a plastic coverslip and hooked onto the edges of the coverslip (Figure 42D).

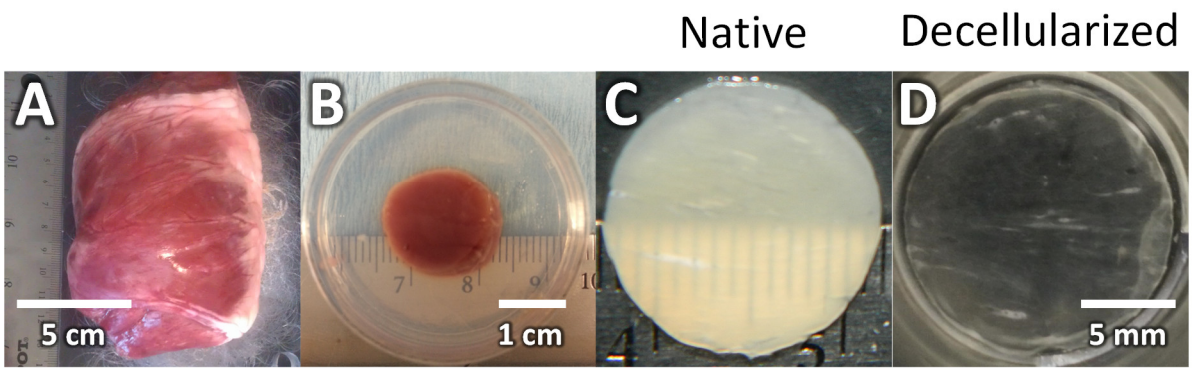

Figure 42. Preparation of engineered heart slices.
A. Left ventricles were excised from pig hearts. **B.** A 1 cm-thick epicardial plug was punched out and embedded in agarose. **C.** Tissue was sectioned into 300 µm-thick slices using a vibratome. **D.** Slices were decellularized by SDS and Triton X-100. And spread on 14 mm-diameter coverslips. **C** and **D** have the same scale.

Because the slices were only 300 µm-thick, they were decellularized after only 3.5 h in detergents, and then washed overnight in PBS or HBSS. Imaging of collagen using SHG showed that fiber alignment and structure was maintained after decellularization (Figure 43A,B). Images of phalloidin staining for F-actin and DAPI

counterstaining for nuclei showed cells were present in native tissue slices (Figure 43C) and absent in decellularized slices (Figure 43D). Cryosections of the ECM were visualized before and after decellularization using phase contrast imaging (Figure 43E,F) and showed that the thickness of the ECM decreased from 301±36 μm (n=4) prior to decellularization to 61±17 μm (n=3) post-decellularization. DNA content decreased from 2.0±0.6 (n=8) to 0.12±0.10 (n=4) μg/mg initial dry weight, and dry weight decreased from 10.2±3.5 (n=8) to 0.9±0.2 mg (n=4).

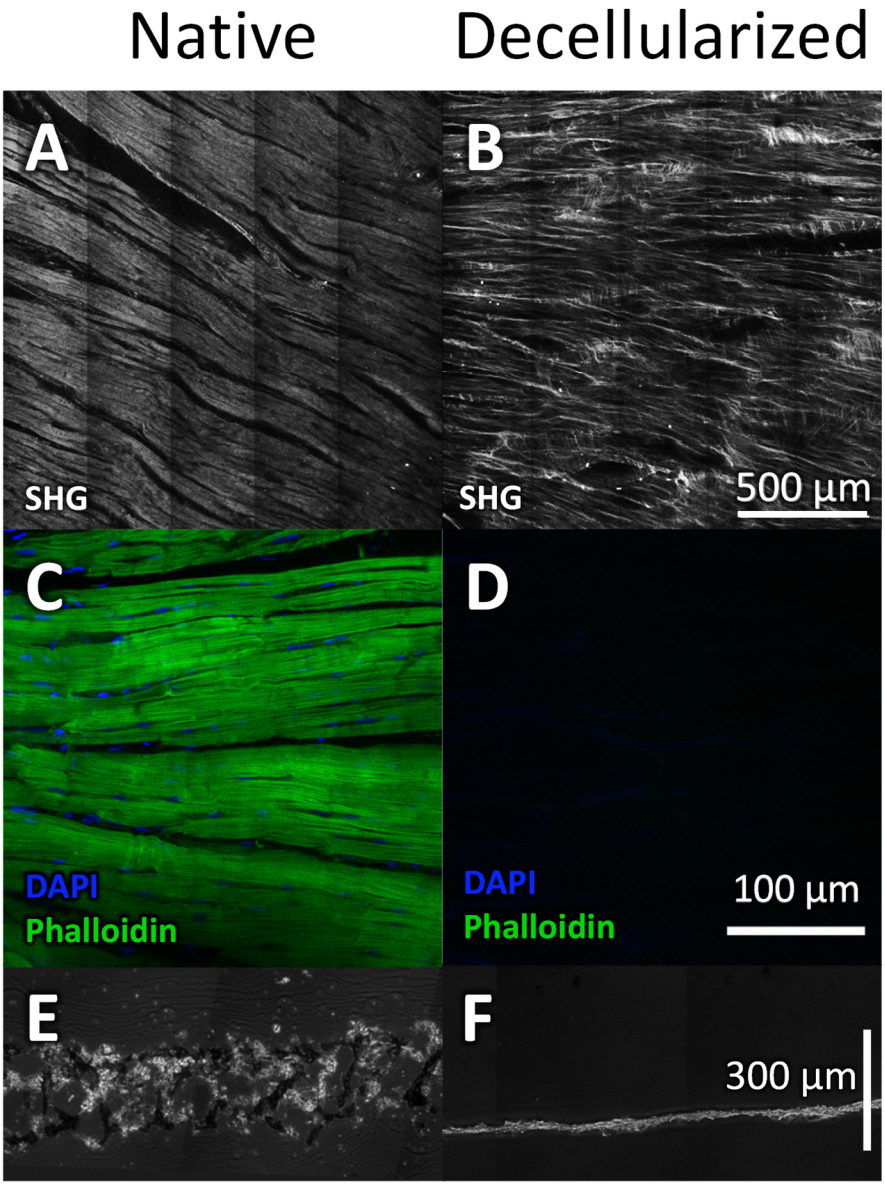

Figure 43. Characterization of decellularized slices.
A-B. SHG imaging showed similar collagen structure and alignment before (**A**), and after (**B**), decellularization. **A** and **B** have the same scale. **C-D**. Confocal images of native (**C**) and decellularized (**D**) ECM stained for nuclei (DAPI) and F-actin (phalloidin) showed a virtual absence of cellular material after decellularization. **C** and **D** have the same scale and imaging settings, and were produced by Dr. Adriana Blazeski. **E-F**.Ten µm-thick cross-sections of slices of ECM before (**E**) and after (**F**) decellularization are shown using phase contrast microscopy. **E** and **F** have the same scale.

Location and orientation of cells seeded on thin slices of decellularized extracellular matrix

Freshly isolated NRVMs were seeded on ECM to form EHS. ECM slices that were not tethered to coverslips compacted into a ball after cell seeding, making them unsuitable for microscopy or experimentation. EHS were imaged with calcein and DRAQ5 for live cells and SHG for collagen so that cell location and orientation could be visualized relative to the collagen matrix in a z-stack (Figure 44). During the first 3-4 days in culture, the cells elongated from their initial rounded shape and by 5-7 days aligned along the direction of the ECM fibers (Figure 44A). The half-maximum of the SHG signal was used to define the surface of the ECM. Three μm below the surface of the ECM, cells were still densely packed (Figure 44A), while 30 μm below the surface some cells could still be found, but were sparse (Figure 44B). Measurements of calcein and SHG intensity as a function of depth (Figure 44C,D), as well as depth-coded images of calcein staining (Figure 44E), showed that the cells were located primarily on the surface of the collagen matrix, but with some penetration into the depth. There were some areas where cells at different depths overlap suggesting that some cells reside below the surface of the main cell layer of the EHS.

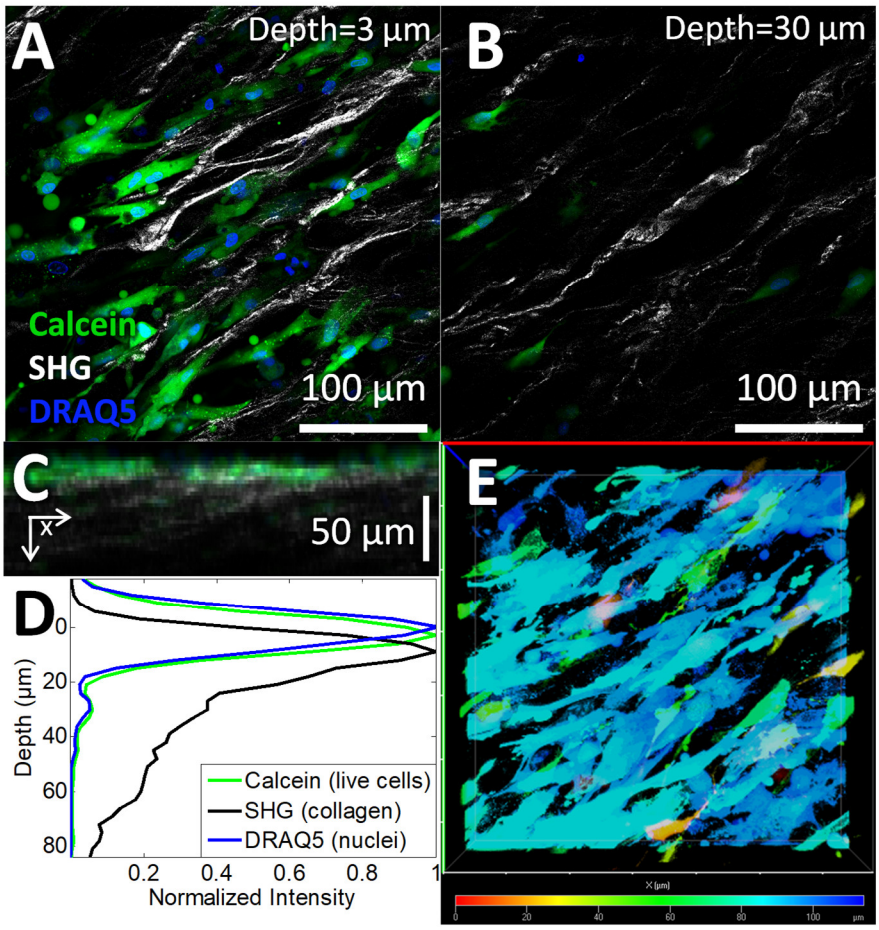

Figure 44. Survival and location of cells in engineered heart slices.
Calcein-AM (live cells), second-harmonic generation (SHG), and DRAQ5 (nuclei) were imaged 7 days after plating to create a z-stack of confocal images. **A-B**. x-y (en face) images from different depths, with zero depth defined to be at the half maximum of the rising edge of the SHG signal (see **D**). **C.** The intensity of calcein-AM, SHG, and DRAQ5 were averaged in the y-direction and plotted in the x-z plane. **D.** These intensities were then averaged in the x-direction and plotted as a function of z (normalized to maximum for each channel), and show a layer of cells residing mostly on top of the ECM. **E**. The calcein signal from the z-stack was thresholded and colored according to the depth.

Live/dead staining showed few dead cells in EHS at day 7 (Figure 45A). CMs had well-formed sarcomeric structure (Figure 45B) and expressed punctate patterns of the gap junctional protein connexin 43 (Figure 45B). Staining with cTnI and vimentin revealed the presence of mostly CMs and some non-CMs (Figure 45C). In general, cells were elongated and aligned (Figure 45B,C). Elongation (length-to-width ratio) and

alignment were quantified by the shape of the cells' nuclei, which had a mean elongation of 2.1 (1.5-2.9) and angular standard deviation of 20° (n=176 nuclei, respectively, Figure 45D).

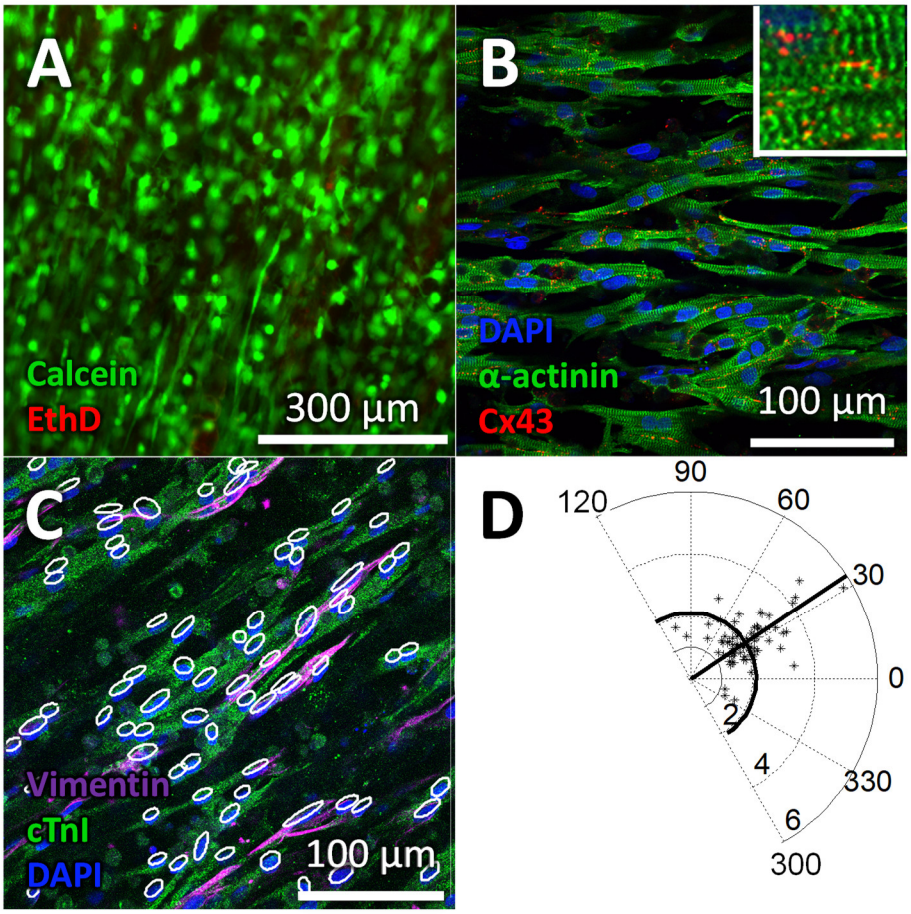

Figure 45. Characterization of cells in engineered heart slices.
A. Staining of live cells with calcein-AM (green) and dead cells with EtD (EthD, red) reveals few dead cells in the EHS 7 days after plating. **B.** α-actinin staining (green) shows alignment and elongation of cells, and distinct sarcomeric striations (insets show portions of the images at 10 times magnification). Connexin 43 (Cx43, red) staining suggests cells are electrically coupled. **C.** Staining with vimentin (violet) for non-CMs, α-actinin (green) for CMs, and DAPI (blue) for nuclei showed mostly CMs and some non-CMs in EHS made from both types of ECM. **D.** Automated analysis of nuclear shapes showed they were elongated and aligned. White ellipses in **C** show fits of nuclei. Radial distances in **D** show elongation (long axis/short axis) of nuclei in **C**, while the angles show the orientation of the long axes of the nuclei. The mean orientation and elongation are marked by solid radial and circumferential lines, respectively. Images in **B** and **C** from Dr. Adriana Blazeski.

Contraction of EHS

During culture, the beating rate of EHS was recorded daily. Two days after cell plating, approximately 40% of the EHS exhibited small asynchronous areas of contraction, 40% showed coordinated contraction across a 0.55 mm^2 field of view, and 20% were quiescent. Over the next 4 days, the fraction of EHS with asynchronous contraction decreased to zero, while the fraction of quiescent EHS increased. By 7 days, about 60% of the EHS were quiescent, while the remainder contracted synchronously and intermittently. Almost all the EHS that were electrically stimulated on days 7-8 after characterization of spontaneous beating exhibited either synchronous contraction across the EHS if assayed for contractility, or activation across the entire EHS if optically mapped, demonstrating that EHS quiescence was not due to cell death. To quantitate contraction, one corner of an EHS was unhooked from the coverslip so that shortening could be observed during electrical pacing (Figure 46A-C). Using displacement as a surrogate for contractile force, we measured the force-frequency relationship of the EHS, and found a statistically significant decrease in contractile force at pacing rates of 4 and 5 Hz relative to 2 Hz (Figure 46D, n=4-6 EHS).

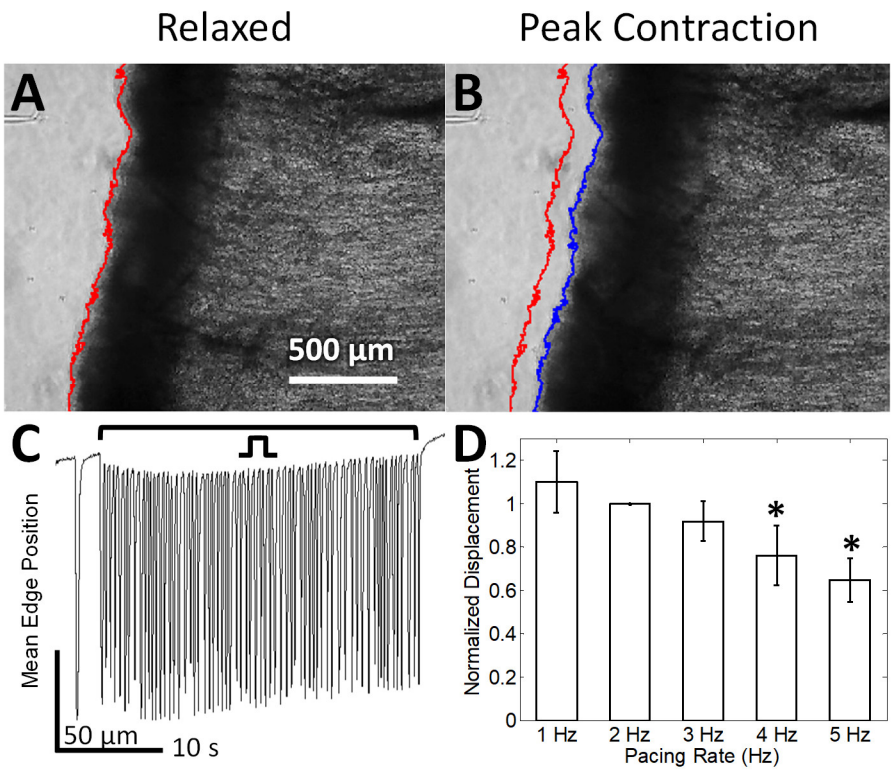

Figure 46. Contraction of engineered heart slices.
A-B. Representative images of EHS while relaxed (**A**), and at the peak of contraction (**B**) show shortening of day 5 EHS with 2 Hz pacing. The edge of the slice is outlined during rest (red line) and at peak contraction (blue line). **C.** The average slice displacement during each frame of the video recording was calculated over a 38 s recording interval. **D.** Using these recordings, the average force-frequency relationship across multiple EHS (n=4-6 for each rate) could be determined. Each EHS was normalized to its 2 Hz peak displacement. * indicates significant decrease ($p<0.05$) in contraction amplitude from that at 2 Hz.

Anisotropic electrical conduction, response to lidocaine, and reentrant activity in EHS

EHS were stimulated at their center by a point electrode. Optical maps enabled the characterization of AP propagation and morphology (Figure 47A,B). At 2 Hz, EHS (n=17) had a normal AP profile with an APD_{80} of 157±39 ms, similar to that reported in NRVM monolayers (137±13 ms on day 6) [94], and an APD_{30} of 69±15 ms. Longitudinal CV was 14.4±5.5 cm/s, transverse CV was 7.5±3.4 cm/s, and the anisotropy ratio of conduction velocities (AR) was 2.0 (1.4-2.8). For pacing rates increasing from 1 to 5 Hz,

APD (Figure 47C) and conduction velocities in the longitudinal and transverse directions (Figure 47D) all had negative rate-dependencies, while AR remained approximately constant at 2.0. Some EHS were kept in culture for 21 days and could be paced and optically mapped (Figure 48). Of four EHS kept until day 21, three could be paced across the entire EHS and had average CVs of 9.7±1.1 and 5.9±0.9 cm/s in the longitudinal and transverse directions, respectively, and APD_{30}s and APD_{80}s of 64±23 and 127±29 ms, respectively, at 2 Hz pacing.

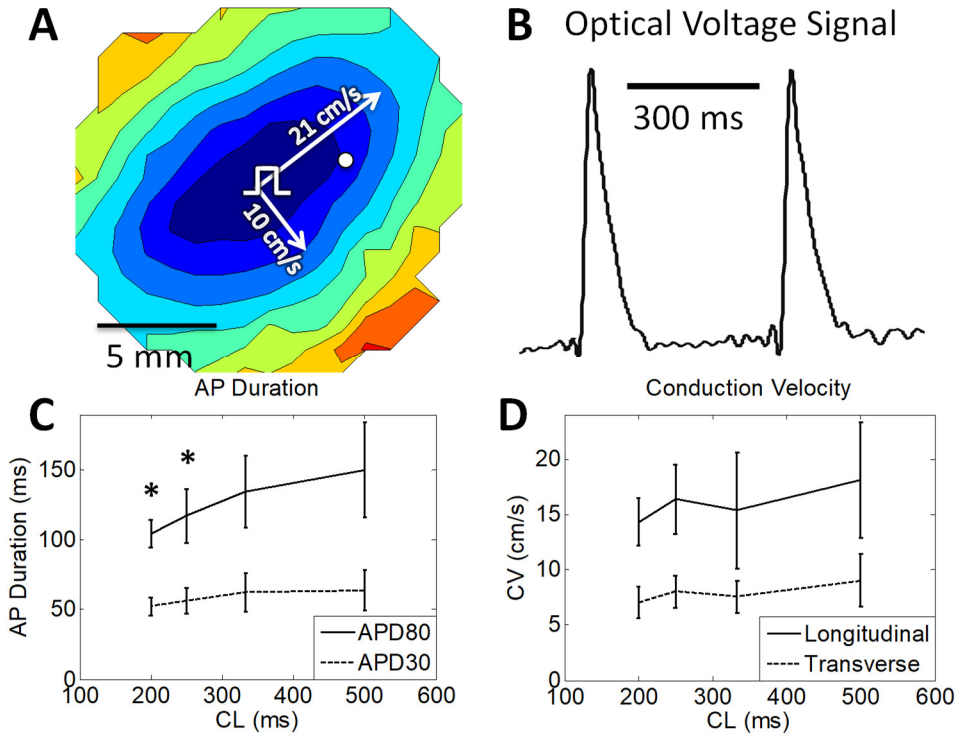

Figure 47. Optical recordings of transmembrane voltage in engineered heart slices. EHS were optically mapped with voltage-sensitive dye after 5-7 days in culture. **A.** Activation map for EHS showed anisotropic propagation during 2 Hz point stimulation. Isochrones are 10 ms. White pulse symbol indicates site of the stimulus electrode. The white dot marks location of recording in **B**. The arrows and values show the calculated longitudinal and transverse CV vectors. **B.** Optical voltage signals in EHS showed normal action potential morphology. **C.** APD_{80} and APD_{30} were measured at different pacing rates. **D.** CVs in the longitudinal and transverse directions were measured at different pacing rates. In **C-D**, the number of EHS recorded was 17,15,13 and 7 at pacing rates 2 to 5 Hz, respectively, with fewer samples at faster rates due to loss of 1:1 capture. * in **C** and **D** indicates significant change ($p<0.05$) from values at 2 Hz.

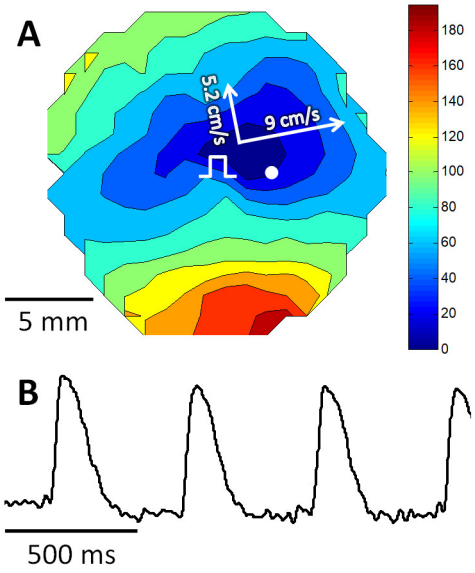

Figure 48. Electrophysiology of engineered heart slice on culture day 21.
A. Activation map. Isochrones are 10 ms. White pulse symbol indicates site of the stimulus electrode. White dot marks location of recording in **B**. White lines and values show the calculated longitudinal and transverse CV vectors. **B.** Optical voltage trace.

Adding increasing doses of lidocaine to EHS (n=4-5) resulted in a statistically significant dose-dependent decrease in CV (Figure 49A-C) and maximum capture rate (Figure 49D) that was largely reversed after washout. Fractional conduction slowing was more pronounced in the longitudinal than transverse direction (Figure 49A-C).

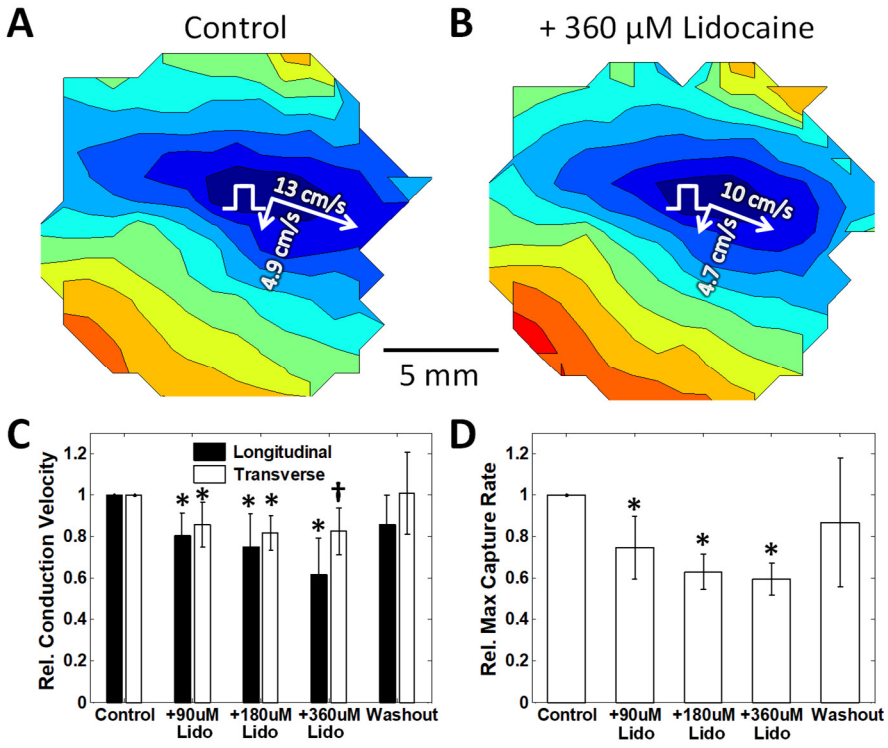

Figure 49. Response of engineered heart slices to lidocaine.
A-B. Activation maps in the absence (**A**) and presence (**B**) of 360 µM lidocaine at 2 Hz pacing rate showed lidocaine caused conduction slowing in EHS. Activation maps in **A** and **B** have 20 ms isochrones and the same color scale. White pulse symbol indicates site of the stimulus electrode. White lines and values show the calculated longitudinal and transverse CV vectors. **C.-D.** Over multiple samples, when normalized to lidocaine-free control (longitudinal CV=10.3±3.1 cm/s, transverse CV=4.0±0.8 cm/s, and max. capture rate=4.1±1.2 Hz), lidocaine decreased transverse and especially longitudinal CV (2Hz pacing shown) (**C**) and maximum capture rate (**D**) in a dose-dependent manner that was largely reversed after at least 15 min washout. * indicates significant difference ($p<0.05$) from control. † indicates significant difference ($p<0.05$) from relative CV in longitudinal direction. n=4-5 EHS; one EHS in **C** lost capture in 360 µM lidocaine.

Reentrant activity could be induced in EHS by pacing at progressively faster rates. At slow pacing rates, EHS exhibited approximately elliptical wavefronts spreading from a point stimulus (Figure 50A), but as pacing rates increased, a reentrant spiral wave sometimes formed (Figure 50B-G,K), which could be terminated by a high-intensity electrical field pulse (Figure 50H-K). In 17 EHS that were rapidly paced, 8 had one or

more pace-inducible spiral waves, which were induced at a pacing rate of 6.3±1.4 Hz. All the spiral waves could be terminated by field stimulation of 6-24 V/cm.

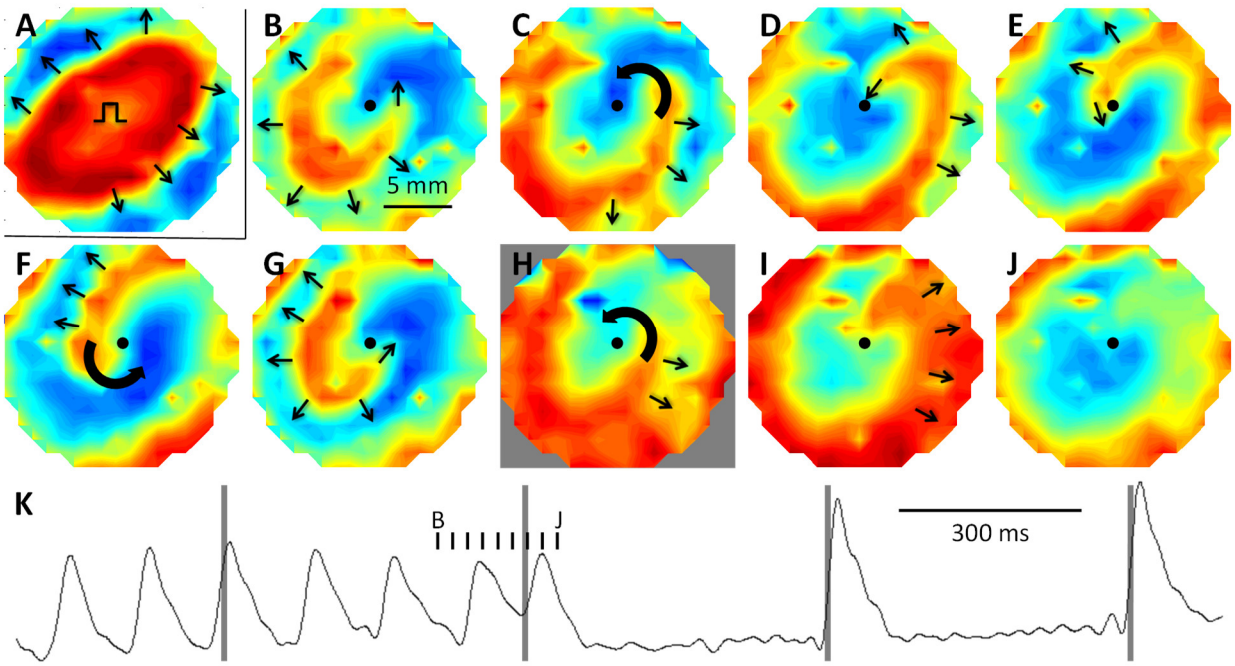

Figure 50. Reentrant activity in engineered heart slices.
A.-J. Snapshots of transmembrane voltage over time. Red shows depolarization, blue shows rest. **A.** EHS produced uniform anisotropic conduction at 2 Hz pacing rate. Pulse symbol indicates site of the stimulus electrode. **B-G.** A counterclockwise spiral wave was induced after pacing at 8.3 Hz. Voltage maps taken 25 ms apart show reentry (**B-G**). Four 24 V/cm electrical shocks were applied 500 ms apart, and the second (**H**, gray background) terminated the spiral wave (**I-J**). Small arrows show movement of AP wavefront. Thick curved arrows show propagation around the central rotation of the spiral wave. **K.** Trace of the entire sequence of applied shocks (gray lines) and the optical voltage recording from the location marked by the small black dot in **B-J**. Small black tick marks indicate when the snapshots in **B-J** were taken.

Discussion

Recellularization of the decellularized heart, either through the coronary circulation or by direct injection, has not succeeded in repopulating the tissue evenly. The study of recellularized hearts has focused primarily on mechanical function, with only two electrophysiological reports to date. Those reports used calcium indicator dyes in hearts recellularized by coronary perfusion. In one, electrical activity was shown to propagate

over a 150 μm-square area of a recellularized mouse ventricle [117], while in the other, cells in recellularized rat ventricles formed patches that were either well synchronized, unsynchronized but organized, or disorganized [115].

Alternatively, global recellularization of isolated slices of myocardium is a much simpler proposition because cells can be seeded directly onto the exposed surface, although penetration of cells into the interior is limited. Two to 10 mm-thick slices of dissected porcine heart have been decellularized by mechanical agitation [190], sonication [198], or perfusion through a blood vessel [199], but these procedures used long treatment times (10 days, 2.5 weeks, and 5 days, respectively), which run the risk of excessive degradation of constituents of the ECM [200].

Our strategy is to plate CMs onto very thin sections of decellularized ECM. By cutting the tissue chunks into 300 μm-thick sections (Figure 42), decellularization time by orbital agitation is greatly reduced to around 3.5 h. Godier-Furnemont et al. [201] and Oberwallner et al. [191] also used orbital agitation to decellularize 300 μm-thick slices obtained from human heart, but over a period of 8 h and 1 week, respectively. Following decellularization, our ECM slices thin down to around 60 μm (Figure 43F), but can still be handled manually. By using tissue plugs from porcine hearts, we can obtain 10-20 sections per plug. Cells can be directly plated on top of the ECM, and the recellularized tissue is more homogeneous than that made by perfusion mediated recellularization of whole hearts. Other advantages of this approach are that EHS are relatively transparent and can be easily monitored during culture using bright-field microscopy and that cell shape, orientation, density and connectivity can be visualized more easily than when the cells are fully embedded in a 3-D tissue matrix.

Myocytes in engineered heart slices experience important physiological cues from 3-D matrix

Fully 3-D engineered cardiac tissues have been achieved by culturing CMs in hydrogels or on synthetic scaffolds [189]. This approach has the advantage of control of the scaffold composition and shape, and has been successfully utilized to produce physiologically functional cardiac tissue constructs [189]. Uniformity of cell density and connectivity through the depth of the tissue remains a challenge, although recent advances appear to have largely addressed this problem for certain types of constructs [188]. However, these systems lack many of the instructive cues offered by the ECM [202].

Following decellularization, the thickness of the sliced ECM reduces from 300 μm to around 60 μm (Figure 43E,F). Similarly, Ott, et al. [111] also found a significant decrease in thickness (from an average of 3.59 to 0.24 mm) after perfusion decellularization of whole hearts. We found that cells in EHS lie mostly at the surface of the slice and experience important biochemical, structural, and mechanical signals from the underlying 3-D ECM, a situation referred to as "2.5-D" [203]. If left untethered, the EHS would compact and ball up, making them unsuitable for further experimentation. However, attachment of the decellularized slices to coverslips (Figure 42D) maintains the distance between ECM fibers in the x-y plane. Cells can settle into small openings and valleys of the ECM matrix, and may extend to a limited degree into the matrix (Figure 44).

Native ECM contains a complex mixture of structural proteins that interact with the CMs and influence their adhesion, growth, and contractile function [202]. For example,

the ECM can retain growth factors and mediate the availability of these and other signaling molecules [110], including latent TGF-β, which is important for MFB differentiation [204]. Additionally, cell function is affected by integrin-matrix binding and other biomechanical pathways [110, 205]. Although the degree of retention of different ECM constituents varies with the decellularization method [113], the complex protein composition of native ECM is largely retained following decellularization, which is an advantage over scaffolds that provide only one or a small number of ECM proteins, since cell growth depends on a variety of ECM proteins [114, 206].

A special advantage of native ECM is that it is a natural scaffold that contains a fine collagen weave that is aligned along the myocardial cells. This alignment is retained following decellularization (Figure 44A-B, Figure 45) [111, 191]. Because structural cues on the micro- and nano-scale are sufficient to cause CM alignment [207], the ECM promotes alignment of the engrafted CMs. Additionally, this scaffold is sufficiently compliant to be substantially deformed by cell contraction (Figure 46).

Thus, important physiological cues that have beneficial effects on CM function are still present in EHS. Indeed, we found that NRVMs in our EHS remained electrically connected and active for at least 21 days in culture (Figure 48), a period of time that is much longer than in NRVM monolayers, which have a maximal culture period of about ten days in our lab [208]. Additionally, Oberwallner and co-workers seeded neonatal mouse CMs or hiPSC-CMs onto 300 μm-thick slices obtained from decellularized human heart, and reported cell attachment and survival, visible contraction of the matrix, and increased cellular metabolic activity compared with cells cultured on tissue culture plastic [191].

Myocytes are elongated and aligned in engineered heart slices

In native atrial and ventricular myocardium, cardiac cells have an elongated rod shape and are aligned along fiber directions, which is important for efficient force production. When CMs are cultured on chemically or topologically defined anisotropic substrates, they have an elongated shape and align along a preferred direction, with better ultrastructural organization and higher contractile force than when cultured on uniform surfaces [209]. Cell elongation and alignment have also been shown to affect the intracellular handling of calcium [209, 210], which is vital to excitation-contraction coupling in the heart and, when disturbed, is a mechanism for many cardiac arrhythmias [211]. We measured nuclear elongation as a surrogate for cellular elongation because nuclear deformation parallels cellular deformation and anisotropy [194], and because the functional consequences of cell shape are mediated by changes in gene expression arising from deformation of the nucleus by microtubules and intermediate filaments and subsequent mechanotransduction events in CFBs and CMs [119, 120].

Another important functional consequence of cell elongation and alignment is anisotropic AP propagation [212], a property of native tissue which, under pathological conditions, can cause propagation to locally fail and create arrhythmic, reentrant circuits [213]. Fiber alignment and anisotropy can vary with location in the heart, and while sophisticated microprinting techniques can be used to recapitulate a DT-MRI image as a two-dimensional pattern of cells [214], our approach is to use the ECM as a template for cellular patterning. EHS can be prepared from any region of the heart to study the effects of the local structure. For example, cells grown on the endocardial surface of decellularized hearts do not align [116], while cells in our slices, taken from near the

epicardium, do. To our knowledge, our study is the first demonstration of anisotropic conduction of electrical activity in recellularized ECM. In EHS, the fibrillar structure of the ECM leads to cell elongation and alignment (Figure 44 and Figure 45), which then results in anisotropic conduction (Figure 47). AR is around 2.0, which falls within the range of 1.4-3.7 that can be achieved with NRVM monolayers cultured on anisotropic 2-D substrates [215] but is somewhat lower than the AR of ~2.7 found in adult ventricular muscle [216].

Cardiomyocytes in engineered heart slices are mechanically active and contract synchronously

CMs in EHS form a confluent, contractile, syncytium (Figure 44-Figure 46) that is electrically coupled by gap junctions (Figure 45B). The CMs produce enough force to overcome the stiffness of the ECM, resulting in EHS shortening during contraction (Figure 46). Optical mapping showed that during spontaneous activity or electrical pacing, APs propagate through the entire surface of the EHS (Figure 47A), which act to initiate and synchronize contraction throughout the EHS. Measurements of the force-frequency relation (Figure 46D) show a monotonic decrease in contraction from 1 to 5 Hz pacing rate, consistent with measurements in other NRVM-based engineered cardiac tissues [217] and native rat myocardium [218].

Engineered heart slices exhibit physiological response to lidocaine

The fact that EHS form an anisotropic syncytium allowed us to study the effect of drugs on longitudinal and transverse conduction velocities, which is not possible in simpler systems. To demonstrate this, we applied increasing doses of lidocaine, a sodium channel blocker that is clinically used as an antiarrhythmic agent [195], and

measured its effect on CV and maximum capture rate. We found a 19% and 14% decrease in CV at 2 Hz by 90 μM lidocaine in the longitudinal and transverse directions, respectively (Figure 49C), which is similar to the reported ~19% increase in conduction time at 1 Hz by 100 μM lidocaine in Langendorff-perfused rabbit hearts [219], although direct comparison of these values is complicated by the different models and pacing rates. Additionally, we found more fractional slowing in the longitudinal direction (Figure 49C) which is consistent with findings in Langendorff-perfused dog hearts [220]. We also found a dose-dependent decrease in maximum capture rate by lidocaine (Figure 49D), which is expected due to its sodium channel blocking activity [195]. These findings demonstrate the applicability of EHS to studying drug effects on cardiac tissue.

Potential applications of engineered heart slices

EHS are an attractive model for physiological and pathophysiological studies because of their contractile and electrophysiological function at a tissue level. Their macroscopic 2.5-dimensional nature represents a step up in structural and functional complexity from one-dimensional tissue constructs (strips, strands, fiber bundles), opening the door to studies involving biaxial stretch or two-dimensional tissue electrophysiology. EHS can be maintained in culture for at least 21 days (Figure 48), raising the possibility of their use for long-term drug studies. The ECM scaffold is an aligned substrate that is inexpensive and does not require specialized facilities to produce. Although we used NRVMs as the cardiac cell type, other cell types, such as hiPSC-CMs, can be substituted.

Although other investigators have recellularized whole-heart ECM with CMs, the distribution of cells is generally patchy and not well-coupled electrically, making them

prone to arrhythmia [115]. In EHS, CMs are electrophysiologically active throughout, behave as an electrically coupled syncytium, and exhibit contraction and anisotropic conduction similar to that in native tissue, with physiological (for rat) negative rate-dependencies of contractility (Figure 46D), APD (Figure 47C), CV (Figure 47D), as well as physiological drug response (Figure 49). Unlike single cells or 1-D tissue constructs, EHS allow 2-D wave propagation and are large enough in area to support reentrant arrhythmias (Figure 50), which are the more life-threatening forms of arrhythmia (like fibrillation). Cell monolayers also support reentrant arrhythmias and have been used for mechanistic studies [221], but they are cultured in a less physiological microenvironment consisting of a rigid flat surface typically coated with a single ECM protein.

The anisotropy of EHS may prove to be especially useful in studying MFB-CM or CFB-CM connections, since CMs *in vivo* are highly anisotropic and preferentially express connexins at their ends [222], while cells cultured on unpatterned plastic are less anisotropic and express Cx43 fairly uniformly over any place they contact other CMs (see Figure 7F). This Cx43 remodeling may increase heterocellular coupling. Additionally, the softer substrate of EHS may prevent spontaneous differentiation of CFBs into MFBs, allowing us to study MFBs without having to block TGF-β. This may help resolve the difference between the findings of Quinn, at. al., in whole hearts that electrical coupling in injured regions occurs between MFB and CM, but not between CFB and CM in healthy regions [145], and our finding and others [35, 78] that both CFB and MFB electrically couple to CMs *in vitro*. While we extensively characterized our CFBs to ensure they were behaving as undifferentiated CFBs, we cannot exclude that

they and CMs are coupling due to the unphysiological conditions of culture, so any steps towards a better engineered model may help resolve this.

For *in vitro* pacing of cells, a key advantage of our spark cluster system is the fact that that we can point pace. Point activation, and the resulting pre- and post-activation stretch of cells may be important for proper maturation. Unfortunately, in our study, the cells were on relatively stiff plastic, and so could not be significantly pre- or post- stretched by neighboring cells. A substrate such as EHS that could be deformed by cells and allow them to transfer their contraction force to their neighbors may be key to deriving the putative benefits of point pacing. While improvements in cell maturity have been made by using electrical pacing with a deformable substrate, as outlined in Chapter 1, these have all field paced, potentially limiting their efficacy, as described in Chapter 4. Point pacing in conjunction with a deformable substrate such as EHS may prove to be more efficacious in maturing CMs.

EHS may also prove to be valuable for studies of myocardial contraction. With the proper interface, they can be stretched to different resting lengths. By changing the thickness of the EHS, the mechanical load presented to the cells can be varied [223, 224]. Additionally, EHS may be superior to adherent cells or cell monolayers for metabolic studies, because of their ability to perform mechanical work.

EHS will undoubtedly be useful for a better understanding of the physiological and pathophysiological roles of the ECM. For example, they can be formed using decellularized slices from different regions of the heart, from old vs. young hearts, and from healthy vs. diseased hearts, all of which can have differing compositions and structure of ECM [114, 225, 226], which will be especially useful for uncovering the

effect of ECM on heterocellular coupling, combined with the method discussed in Chapters 2 and 3. By obtaining sequential ECM slices from the same tissue plug, our approach readily yields multiple EHS with similar characteristics, making them effective as a tool for *in vitro* investigations.

Finally, in terms of clinical applications, EHS may be an attractive alternative to the method of forming myocardial patches by stacking individual sheets of CMs grown on flat surfaces [227]. EHS may also be useful as a preclinical model for drug testing, much as native cardiac slices are being used [228]. Additionally, this may allow for insight into the mechanism of cardiac resynchronization therapy, which still has a paucity of mechanistic data, due to the difficulty and low-throughput of studies that varied the timing of electrical and mechanical stimuli to investigate how electromechanical delay affects cellular function [181, 182]. The pacing system described in Chapter 4 as well as the EHS described here could be used to compare point and field pacing to see if a propagating wave alters gene expression and electrophysiology. This would demonstrate the importance of proper pre- and post-stretch produced by a propagating contractile wave, demonstrating a mechanism of CRT beyond improving pump function. However, functional variability between EHS remains a present limitation, and improved protocols for their production are be needed.

Conclusion

Engineered heart slices are essentially 2.5-dimensional tissues that retain important biochemical, structural and mechanical aspects of the ECM. CMs grown in EHS are aligned and can be maintained in culture, resulting in a tissue that has

anisotropic properties similar to native tissue. EHS contract synchronously throughout and are electrophysiologically active, behaving as an integrated, functional tissue. Thus, they can serve as a model system for studies of physiological and pathophysiological myocardial function "in a dish."

Acknowledgements

This study was conducted in the laboratory of Dr. Leslie Tung with Dr. Adriana Blazeski. This work was supported by Maryland Stem Cell Research Fund grant 2013-MSCRFeIIe0045 (L.T.) and NIH grant S10 RR025544 (L.T.) as well as Mid-Atlantic AHA predoctoral fellowships (A.B. and G.M.K). Special thanks to Dr. Gordon Tomaselli for the use of his Nanodrop spectrophotometer and Esther Kieserman for microscopy assistance. The multiphoton microscope used for SHG imaging was funded by NIH Grant S10 RR024550 (Scot Kuo, PI). This work has been published in Biomaterials [229].

Conclusion

The novel uses of tandem-cell units outlined in this work have the potential to lead to important scientific and clinical progress. Chapters 2 and 3 point the way to a method to conclusively know whether MFBs and CFBs are connected enough to CMs to influence their electrophysiology, which can guide drug design strategies for treating heart failure. Chapter 4 points the way towards a relatively simple, scalable method of contactless pacing that should make it easier to mature cells for basic science studies or tissue engineering applications. Finally, Chapter 5 complements the previous projects by developing an ECM-based scaffold that should present more physiological cues to CMs, as well as CFBs and MFBs, increasing the physiological relevance of our work. This, coupled with the fact that it produces an aligned, deformable substrate may prove to allow further maturation of CMs.

References

[1] Oesterhelt D. Functions of a New Photoreceptor Membrane. *Proc Natl Acad Sci* 1973; 70: 2853–2857.

[2] Deisseroth K. Optogenetics. *Nat Methods* 2011; 8: 26–29.

[3] Nagel G, Szellas T, Huhn W, et al. Channelrhodopsin-2, a directly light-gated cation-selective membrane channel. *Proc Natl Acad Sci U S A* 2003; 100: 13940–5.

[4] Feldbauer K, Zimmermann D, Pintschovius V, et al. Channelrhodopsin-2 is a leaky proton pump. *Proc Natl Acad Sci U S A* 2009; 106: 12317–22.

[5] Nagel G, Brauner M, Liewald JF, et al. Light Activation of Channelrhodopsin-2 in Excitable Cells of Caenorhabditis elegans Triggers Rapid Behavioral Responses. *Curr Biol* 2005; 15: 2279–2284.

[6] Schneider F, Grimm C, Hegemann P. Biophysics of Channelrhodopsin. *Annu Rev Biophys* 2015; 44: 167–86.

[7] Boyden ES, Zhang F, Bamberg E, et al. Millisecond-timescale, genetically targeted optical control of neural activity. *Nat Neurosci* 2005; 8: 1263–1268.

[8] Bruegmann T, Malan D, Hesse M, et al. Optogenetic control of heart muscle in vitro and in vivo. *Nat Methods* 2010; 7: 897–900.

[9] Jia Z, Valiunas V, Lu Z, et al. Stimulating cardiac muscle by light cardiac optogenetics by cell delivery. *Circ Arrhythmia Electrophysiol* 2011; 4: 753–760.

[10] Nussinovitch U, Shinnawi R, Gepstein L. Modulation of cardiac tissue electrophysiological properties with light-sensitive proteins. *Cardiovasc Res* 2014; 102: 176–187.

[11] Yu J, Entcheva E. Inscribing Optical Excitability to Non-Excitable Cardiac Cells: Viral Delivery of Optogenetic Tools in Primary Cardiac Fibroblasts. In: *Optogenetics*, pp. 303–317.

[12] Boyle PM, Karathanos T V., Trayanova NA. Cardiac Optogenetics 2018. *JACC Clin Electrophysiol* 2018; 4: 155–167.

[13] Crocini C, Ferrantini C, Pavone FS, et al. Optogenetics gets to the heart: A guiding light beyond defibrillation. *Prog Biophys Mol Biol* 2017; 130: 132–139.

[14] Yu J, Entcheva E. Inscribing Optical Excitability to Non-Excitable Cardiac Cells: Viral Delivery of Optogenetic Tools in Primary Cardiac Fibroblasts. In: *Optogenetics*. New York, NY: Humana Press, pp. 303–317.

[15] Brown RD, Ambler SK, Mitchell MD, et al. THE CARDIAC FIBROBLAST: Therapeutic Target in Myocardial Remodeling and Failure. *Annu Rev Pharmacol Toxicol* 2005; 45: 657–687.

[16] Fujiu K, Nagai R. Fibroblast-mediated pathways in cardiac hypertrophy. *J Mol Cell Cardiol* 2014; 70: 64–73.

[17] Porter KE, Turner NA. Cardiac fibroblasts: At the heart of myocardial remodeling. *Pharmacol Ther* 2009; 123: 255–278.

[18] Davis J, Molkentin JD. Myofibroblasts: Trust your heart and let fate decide. *J Mol Cell Cardiol* 2014; 70: 9–18.

[19] Turner NA, Porter KE. Function and fate of myofibroblasts after myocardial infarction. *Fibrogenesis Tissue Repair* 2013; 6: 5.

[20] Tomasek JJ, Gabbiani G, Hinz B, et al. Myofibroblasts and mechano-regulation of connective tissue remodelling. *Nat Rev Mol Cell Biol* 2002; 3: 349–63.

[21] Yong KW, Li Y, Huang G, et al. Mechanoregulation of cardiac myofibroblast differentiation: implications for cardiac fibrosis and therapy. *Am J Physiol - Hear Circ Physiol* 2015; 309: H532–H542.

[22] Humeres C, Frangogiannis NG. Fibroblasts in the Infarcted, Remodeling, and Failing Heart. *JACC Basic to Transl Sci*; 4. Epub ahead of print 2019. DOI: 10.1016/j.jacbts.2019.02.006.

[23] Chistiakov DA, Orekhov AN, Bobryshev Y V. The role of cardiac fibroblasts in post-myocardial heart tissue repair. *Exp Mol Pathol* 2016; 101: 231–240.

[24] Stempien-Otero A, Kim DH, Davis J. Molecular networks underlying myofibroblast fate and fibrosis. *J Mol Cell Cardiol* 2016; 97: 153–161.

[25] Deb A, Ubil E. Cardiac fibroblast in development and wound healing. *J Mol Cell Cardiol* 2014; 70: 47–55.

[26] Wipff PJ, Rifkin DB, Meister JJ, et al. Myofibroblast contraction activates latent TGF-β1 from the extracellular matrix. *J Cell Biol* 2007; 179: 1311–1323.

[27] Weber KT, Sun Y, Bhattacharya SK, et al. Myofibroblast-mediated mechanisms of pathological remodelling of the heart. *Nat Rev Cardiol* 2013; 10: 15–26.

[28] Piek A, de Boer RA, Silljé HHW. The fibrosis-cell death axis in heart failure. *Heart Fail Rev* 2016; 21: 199–211.

[29] Weber KT, Sun Y, Bhattacharya SK, et al. Myofibroblast-mediated mechanisms of pathological remodelling of the heart. *Nat Rev Cardiol* 2013; 10: 15–26.

[30] Martin ML, Blaxall BC. Cardiac intercellular communication: Are myocytes and fibroblasts fair-weather friends? *J Cardiovasc Transl Res* 2012; 5: 768–782.

[31] van den Borne SWM, Diez J, Blankesteijn WM, et al. Myocardial remodeling after infarction: the role of myofibroblasts. *Nat Rev Cardiol* 2010; 7: 30–37.

[32] Driesen RB, Nagaraju CK, Abi-Char J, et al. Reversible and irreversible differentiation of cardiac fibroblasts. *Cardiovasc Res* 2014; 101: 411–422.

[33] Chen W, Frangogiannis NG. Fibroblasts in post-infarction inflammation and

cardiac repair. *Biochim Biophys Acta - Mol Cell Res* 2013; 1833: 945–953.

[34] Ma Y, Iyer RP, Jung M, et al. Cardiac Fibroblast Activation Post-Myocardial Infarction: Current Knowledge Gaps. *Trends Pharmacol Sci* 2017; 38: 448–458.

[35] Salvarani N, Maguy A, Simone SA De, et al. TGF-β1 (Transforming Growth Factor-β1) Plays a Pivotal Role in Cardiac Myofibroblast Arrhythmogenicity. *Circ Arrhythmia Electrophysiol* 2017; 10: e004567.

[36] Nguyen TP, Qu Z, Weiss JN. Cardiac fibrosis and arrhythmogenesis: The road to repair is paved with perils. *J Mol Cell Cardiol* 2014; 70: 83–91.

[37] McArthur L, Chilton L, Smith GL, et al. Electrical consequences of cardiac myocyte: fibroblast coupling. *Biochem Soc Trans* 2015; 43: 513–518.

[38] Follonier L, Schaub S, Meister J-J, et al. Myofibroblast communication is controlled by intercellular mechanical coupling. *J Cell Sci* 2008; 121: 3305–3316.

[39] Kamkin A, Kiseleva I, Wagner K-D, et al. Characterization of stretch-activated ion currents in isolated atrial myocytes from human hearts. *Pflugers Arch* 2003; 446: 339–346.

[40] Kohl P, Kamkin AG, Kiseleva IS, et al. Mechanosensitive fibroblasts in the sino-atrial node region of rat heart: interaction with cardiomyocytes and possible role. *Exp Physiol* 1994; 79: 943–56.

[41] Gaudesius G, Miragoli M, Thomas SP, et al. Coupling of cardiac electrical activity over extended distances by fibroblasts of cardiac origin. *Circ Res* 2003; 93: 421–428.

[42] Xie Y, Garfinkel A, Weiss JN, et al. Cardiac alternans induced by fibroblast-myocyte coupling: mechanistic insights from computational models. *Am J Physiol Heart Circ Physiol* 2009; 297: H775–H784.

[43] Maleckar MM, Greenstein JL, Giles WR, et al. Electrotonic coupling between human atrial myocytes and fibroblasts alters myocyte excitability and repolarization. *Biophys J* 2009; 97: 2179–2190.

[44] Tanaka K, Zlochiver S, Vikstrom KL, et al. Spatial distribution of fibrosis governs fibrillation wave dynamics in the posterior left atrium during heart failure. *Circ Res* 2007; 101: 839–847.

[45] Nguyen TP, Xie Y, Garfinkel A, et al. Arrhythmogenic consequences of myofibroblast-myocyte coupling. *Cardiovasc Res* 2012; 93: 242–51.

[46] Kohl P, Kamkin AG, Kiseleva IS, et al. Mechanosensitive fibroblasts in the sino-atrial node region of rat heart: interaction with cardiomyocytes and possible role. *Exp Physiol* 1994; 79: 943–56.

[47] Andrew MacCannell K, Bazzazi H, Chilton L, et al. A Mathematical Model of Electrotonic Interactions between Ventricular Myocytes and Fibroblasts. *Biophys J* 2007; 92: 4121–4132.

[48] Chilton L, Ohya S, Freed D, et al. K+ currents regulate the resting membrane potential, proliferation, and contractile responses in ventricular fibroblasts and myofibroblasts. *Am J Physiol Heart Circ Physiol* 2005; 288: H2931–H2939.

[49] Shibukawa Y, Chilton EL, Maccannell KA, et al. K 1 Currents Activated by Depolarization in Cardiac Fibroblasts. *Biophys J* 2005; 88: 3924–3935.

[50] Li G-R, Sun H-Y, Chen J-B, et al. Characterization of multiple ion channels in cultured human cardiac fibroblasts. *PLoS One* 2009; 4: e7307.

[51] Thodeti CK, Paruchuri S, Meszaros JG. A TRP to cardiac fibroblast differentiation. *Channels* 2013; 7: 211–214.

[52] Yue Z, Xie J, Yu AS, et al. Role of TRP channels in the cardiovascular system. *Am J Physiol Heart Circ Physiol* 2015; 308: H157–H182.

[53] Xie Y, Garfinkel A, Camelliti P, et al. Effects of fibroblast-myocyte coupling on cardiac conduction and vulnerability to reentry: A computational study. *Hear Rhythm* 2009; 6: 1641–1649.

[54] Jacquemet V, Henriquez CS. Loading effect of fibroblast-myocyte coupling on resting potential, impulse propagation, and repolarization: insights from a microstructure model. *AJP Hear Circ Physiol* 2008; 294: H2040–H2052.

[55] Miragoli M, Gaudesius G, Rohr S. Electrotonic modulation of cardiac impulse conduction by myofibroblasts. *Circ Res* 2006; 98: 801–810.

[56] Mahoney VM, Mezzano V, Morley GE. A review of the literature on cardiac electrical activity between fibroblasts and myocytes. *Prog Biophys Mol Biol* 2015; 120: 1–6.

[57] Jacquemet V, Henriquez CS. Modelling cardiac fibroblasts: interactions with myocytes and their impact on impulse propagation. *Europace* 2007; 9: vi29–vi37.

[58] Kléber AG, Rudy Y. Basic mechanisms of cardiac impulse propagation and associated arrhythmias. *Physiol Rev* 2004; 84: 431–88.

[59] Roell W, Lewalter T, Sasse P, et al. Engraftment of connexin 43-expressing cells prevents post-infarct arrhythmia. *Nature* 2007; 450: 819–824.

[60] Ruberman W, Weinblatt EVE, Goldberg JD, et al. Ventricular Premature Complexes and Sudden Death After Myocardial Infarction. *Circulation* 1978; 64: 297–305.

[61] Thompson SA, Copeland CR, Reich DH, et al. Mechanical coupling between myofibroblasts and cardiomyocytes slows electric conduction in fibrotic cell monolayers. *Circulation* 2011; 123: 2083–93.

[62] Vasquez C, Mohandas P, Louie KL, et al. Enhanced fibroblast-myocyte interactions in response to cardiac injury. *Circ Res* 2010; 107: 1011–1020.

[63] Rosker C, Salvarani N, Schmutz S, et al. Abolishing myofibroblast arrhythmogeneicity by pharmacological ablation of α-smooth muscle actin

containing stress fibers. *Circ Res* 2011; 109: 1120–1131.

[64] Askar SF, Bingen BO, Swildens J, et al. Connexin43 silencing in myofibroblasts prevents arrhythmias in myocardial cultures: role of maximal diastolic potential. *Cardiovasc Res* 2012; 93: 434–44.

[65] Benamer N, Vasquez C, Mahoney VM, et al. Fibroblast KATP currents modulate myocyte electrophysiology in infarcted hearts. *Am J Physiol Heart Circ Physiol* 2013; 304: H1231-9.

[66] Grand T, Salvarani N, Jousset F, et al. Aggravation of cardiac myofibroblast arrhythmogeneicity by mechanical stress. *Cardiovasc Res* 2014; 104: 489–500.

[67] Rohr S. Myofibroblasts in diseased hearts: New players in cardiac arrhythmias? *Hear Rhythm* 2009; 6: 848–856.

[68] Zlochiver S, Muñoz V, Vikstrom KL, et al. Electrotonic Myofibroblast-to-Myocyte Coupling Increases Propensity to Reentrant Arrhythmias in Two-Dimensional Cardiac Monolayers. *Biophys J* 2008; 95: 4469–4480.

[69] Kohl P, Camelliti P, Burton FL, et al. Electrical coupling of fibroblasts and myocytes: Relevance for cardiac propagation. *J Electrocardiol* 2005; 38: 45–50.

[70] Kohl P, Gourdie RG. Fibroblast-myocyte electrotonic coupling: Does it occur in native cardiac tissue? *J Mol Cell Cardiol* 2014; 70: 37–46.

[71] Bers DM. Calcium cycling and signaling in cardiac myocytes. *Annu Rev Physiol* 2008; 70: 23–49.

[72] Pedrotty DM, Klinger RY, Kirkton RD, et al. Cardiac fibroblast paracrine factors alter impulse conduction and ion channel expression of neonatal rat cardiomyocytes. *Cardiovasc Res* 2009; 83: 688–697.

[73] LaFramboise W a, Scalise D, Stoodley P, et al. Cardiac fibroblasts influence cardiomyocyte phenotype in vitro. *Am J Physiol Cell Physiol* 2007; 292: C1799–C1808.

[74] Kaur K, Zarzoso M, Ponce-Balbuena D, et al. TGF-B1, Released by Myofibroblasts, Differentially Regulates Transcription and Function of Sodium and Potassium Channels in Adult Rat Ventricular Myocytes. *PLoS One* 2013; 8: 1–11.

[75] Katwa LC, Campbell SE, Tyagi SC, et al. Cultured myofibroblasts generate angiotensin peptides de novo. *J Mol Cell Cardiol* 1997; 29: 1375–1386.

[76] Rook MB, van Ginneken a C, de Jonge B, et al. Differences in gap junction channels between cardiac myocytes, fibroblasts, and heterologous pairs. *Am J Physiol* 1992; 263: C959–C977.

[77] Chilton L, Giles WR, Smith GL. Evidence of intercellular coupling between co-cultured adult rabbit ventricular myocytes and myofibroblasts. *J Physiol* 2007; 583: 225–236.

[78] McSpadden LC, Kirkton RD, Bursac N. Electrotonic loading of anisotropic cardiac

monolayers by unexcitable cells depends on connexin type and expression level. *Am J Physiol Cell Physiol* 2009; 297: C339-51.

[79] Zhang Y, Kanter EM, Yamada KA. Remodeling of cardiac fibroblasts following myocardial infarction results in increased gap junction intercellular communication. *Cardiovasc Pathol* 2010; 19: e233-40.

[80] Thompson S a., Blazeski A, Copeland CR, et al. Acute slowing of cardiac conduction in response to myofibroblast coupling to cardiomyocytes through N-cadherin. *J Mol Cell Cardiol* 2014; 68: 29–37.

[81] Saffitz JE, Laing JG, Yamada KA. Connexin Expression and Turnover: Implications for Cardiac Excitability. *Circ Res* 2000; 86: 723–728.

[82] Fahrenbach JP, Mejia-Alvarez R, Banach K. The relevance of non-excitable cells for cardiac pacemaker function. *J Physiol* 2007; 585: 565–78.

[83] Zhang Y, Wang H, Kovacs A, et al. Reduced expression of Cx43 attenuates ventricular remodeling after myocardial infarction via impaired TGF-β signaling. *Am J Physiol Hear Circ Physiol* 2009; 298: 477–487.

[84] Asazuma-Nakamura Y, Dai P, Harada Y, et al. Cx43 contributes to TGF-beta signaling to regulate differentiation of cardiac fibroblasts into myofibroblasts. *Exp Cell Res* 2009; 315: 1190–9.

[85] Pfeiffer ER, Wright AT, Edwards AG, et al. Caveolae in ventricular myocytes are required for stretch-dependent conduction slowing. *J Mol Cell Cardiol* 2014; 76: 265–274.

[86] Mills RW, Narayan SM, McCulloch AD. Mechanisms of conduction slowing during myocardial stretch by ventricular volume loading in the rabbit. *Am J Physiol Heart Circ Physiol* 2008; 295: H1270–H1278.

[87] Li J, Patel V V., Kostetskii I, et al. Cardiac-specific loss of N-cadherin leads to alteration in connexins with conduction slowing and arrhythmogenesis. *Circ Res* 2005; 97: 474–481.

[88] Small EM. The Actin – MRTF – SRF Gene Regulatory Axis and Myofibroblast Differentiation. *J Cardiovasc Trans Res* 2012; 5: 794–804.

[89] Rohr S. Arrhythmogenic implications of fibroblast-myocyte interactions. *Circ Arrhythmia Electrophysiol* 2012; 5: 442–452.

[90] Camelliti P, Devlin GP, Matthews KG, et al. Spatially and temporally distinct expression of fibroblast connexins after sheep ventricular infarction. *Cardiovasc Res* 2004; 62: 415–425.

[91] Hinz B, Pittet P, Chaponnier C, et al. Myofibroblast Development Is Characterized by Specific Cell-Cell Adherens Junctions. *Mol Biol Cell* 2004; 15: 4310–4320.

[92] Rangarajan S, Madden L, Bursac N. Use of flow, electrical, and mechanical stimulation to promote engineering of striated muscles. *Ann Biomed Eng* 2014;

42: 1391–405.

[93] Stoppel WL, Kaplan DL, Black LD. Electrical and mechanical stimulation of cardiac cells and tissue constructs. *Adv Drug Deliv Rev* 2016; 96: 135–155.

[94] Sathaye A, Bursac N, Sheehy S, et al. Electrical pacing counteracts intrinsic shortening of action potential duration of neonatal rat ventricular cells in culture. *J Mol Cell Cardiol* 2006; 41: 633–41.

[95] Xia Y, Buja LM, Scarpulla RC, et al. Electrical stimulation of neonatal cardiomyocytes results in the sequential activation of nuclear genes governing mitochondrial proliferation and differentiation. *Proc Natl Acad Sci U S A* 1997; 94: 11399–11404.

[96] McDonough PM, Glembotski CC. Induction of Atrial Natriuretic Factor and Myosin Light Chain-2 Gene Expression in Cultured Ventricular Myocytes by Electrical Stimulation of Contraction. *J Biol Chem* 1992; 267: 11665–11668.

[97] Holt E, Lunde PK, Sejersted OM, et al. Electrical stimulation of adult rat cardiomyocytes in culture improves contractile properties and is associated with altered calcium handling. *Basic Res Cardiol* 1997; 92: 289–298.

[98] Strait JB, Samarel a M. Isoenzyme-specific protein kinase C and c-Jun N-terminal kinase activation by electrically stimulated contraction of neonatal rat ventricular myocytes. *J Mol Cell Cardiol* 2000; 32: 1553–66.

[99] Radisic M, Park H, Shing H, et al. Functional assembly of engineered myocardium by electrical stimulation of cardiac myocytes cultured on scaffolds. *Proc Natl Acad Sci U S A* 2004; 101: 18129–34.

[100] Lasher R a, Pahnke AQ, Johnson JM, et al. Electrical stimulation directs engineered cardiac tissue to an age-matched native phenotype. *J Tissue Eng*; 3. Epub ahead of print January 2012. DOI: 10.1177/2041731412455354.

[101] Hirt MN, Boeddinghaus J, Mitchell A, et al. Functional improvement and maturation of rat and human engineered heart tissue by chronic electrical stimulation. *J Mol Cell Cardiol* 2014; 74C: 151–161.

[102] Nunes SS, Miklas JW, Liu J, et al. Biowire: a platform for maturation of human pluripotent stem cell-derived cardiomyocytes. *Nat Methods* 2013; 10: 781–7.

[103] Godier-Furnémont AFG, Tiburcy M, Wagner E, et al. Physiologic force-frequency response in engineered heart muscle by electromechanical stimulation. *Biomaterials* 2015; 60: 82–91.

[104] Ronaldson-Bouchard K, Ma SP, Yeager K, et al. Advanced maturation of human cardiac tissue grown from pluripotent stem cells. *Nature* 2018; 556: 239–243.

[105] Mengsteab PY, Uto K, Smith AST, et al. Biomaterials Spatiotemporal control of cardiac anisotropy using dynamic nanotopographic cues. *Biomaterials* 2016; 86: 1–10.

[106] Goldfracht I, Efraim Y, Shinnawi R, et al. Acta Biomaterialia Engineered heart tissue models from hiPSC-derived cardiomyocytes and cardiac ECM for disease modeling and drug testing applications. *Acta Biomater* 2019; 92: 145–159.

[107] Gentillon C, Li D, Duan M, et al. Journal of Molecular and Cellular Cardiology Targeting HIF-1 α in combination with PPAR α activation and postnatal factors promotes the metabolic maturation of human induced pluripotent stem cell-derived cardiomyocytes. *J Mol Cell Cardiol* 2019; 132: 120–135.

[108] Bejleri D, Davis ME. Decellularized Extracellular Matrix Materials for Cardiac Repair and Regeneration. *Adv Healthc Mater* 2019; 8: 1–29.

[109] Valiente-Alandi I, Schafer AE, Blaxall BC. Extracellular matrix-mediated cellular communication in the heart. *J Mol Cell Cardiol* 2016; 91: 228–237.

[110] Fan D, Creemers EE, Kassiri Z. Matrix as an interstitial transport system. *Circ Res* 2014; 114: 889–902.

[111] Ott HC, Matthiesen TS, Goh S-K, et al. Perfusion-decellularized matrix: using nature's platform to engineer a bioartificial heart. *Nat Med* 2008; 14: 213–21.

[112] Tapias LF, Ott HC. Decellularized scaffolds as a platform for bioengineered organs. *Curr Opin Organ Transplant* 2014; 19: 145–152.

[113] Akhyari P, Aubin H, Gwanmesia P, et al. The quest for an optimized protocol for whole-heart decellularization: a comparison of three popular and a novel decellularization technique and their diverse effects on crucial extracellular matrix qualities. *Tissue Eng Part C Methods* 2011; 17: 915–926.

[114] Williams C, Quinn KP, Georgakoudi I, et al. Young developmental age cardiac extracellular matrix promotes the expansion of neonatal cardiomyocytes in vitro. *Acta Biomater* 2014; 10: 194–204.

[115] Yasui H, Lee J-K, Yoshida A, et al. Excitation propagation in three-dimensional engineered hearts using decellularized extracellular matrix. *Biomaterials* 2014; 35: 7839–50.

[116] Wainwright JM, Czajka CA, Patel UB, et al. Preparation of cardiac extracellular matrix from an intact porcine heart. *Tissue Eng Part C Methods* 2010; 16: 525–32.

[117] Lu T-Y, Lin B, Kim J, et al. Repopulation of decellularized mouse heart with human induced pluripotent stem cell-derived cardiovascular progenitor cells. *Nat Commun* 2013; 4: 2307.

[118] van Putten S, Shafieyan Y, Hinz B. Mechanical control of cardiac myofibroblasts. *J Mol Cell Cardiol* 2015; 93: 133–142.

[119] Saucerman JJ, Tan PM, Buchholz KS, et al. Mechanical regulation of gene expression in cardiac myocytes and fibroblasts. *Nat Rev Cardiol*. Epub ahead of print 2019. DOI: 10.1038/s41569-019-0155-8.

[120] Herum KM, Lunde IG, Mcculloch AD, et al. The Soft- and Hard-Heartedness of

Cardiac Fibroblasts : Mechanotransduction Signaling Pathways in Fibrosis of the Heart. *J Clin Med*; 6. Epub ahead of print 2017. DOI: 10.3390/jcm6050053.

[121] Li L, Zhao Q, Kong W. Extracellular matrix remodeling and cardiac fibrosis. *Matrix Biol* 2018; 490–506.

[122] Frangogiannis NG. The extracellular matrix in myocardial injury, repair, and remodeling. *J Clin Invest* 2017; 127: 1600–1612.

[123] Tallquist MD, Molkentin JD. Redefining the identity of cardiac fibroblasts. *Nat Rev Cardiol* 2017; 14: 484–491.

[124] Kohl P, Camelliti P. Fibroblast-myocyte connections in the heart. *Hear Rhythm* 2012; 9: 461–464.

[125] Askar SF, Ramkisoensing AA, Schalij MJ, et al. Antiproliferative treatment of myofibroblasts prevents arrhythmias in vitro by limiting myofibroblast-induced depolarization. *Cardiovasc Res* 2011; 90: 295–304.

[126] Yu J, Boyle PM, Klimas A, et al. OptoGap : an optogenetics-enabled assay for quantification of cell-cell coupling in multicellular cardiac tissue. *bioRxiv*; 171397.

[127] Du DTM, Hellen N, Kane C, et al. Action Potential Morphology of Human Induced Pluripotent Stem Cell-Derived Cardiomyocytes Does Not Predict Cardiac Chamber Specificity and Is Dependent on Cell Density. *Biophysj* 2015; 108: 1–4.

[128] Klimas A, Ambrosi CM, Yu J, et al. OptoDyCE as an automated system for high-throughput all-optical dynamic cardiac electrophysiology. *Nat Commun* 2016; 7: 11542.

[129] Lim ZY, Maskara B, Aguel F, et al. Spiral wave attachment to millimeter-sized obstacles. *Circulation* 2006; 114: 2113–21.

[130] Fu J, Wang Y, Yang MT, et al. Mechanical regulation of cell function with geometrically modulated elastomeric substrates. *Nat Methods*; 7. Epub ahead of print 2011. DOI: 10.1038/nmeth.1487.

[131] Korhonen T, Hänninen SL, Tavi P. Model of excitation-contraction coupling of rat neonatal ventricular myocytes. *Biophys J* 2009; 96: 1189–1209.

[132] Williams JC, Xu J, Lu Z, et al. Computational Optogenetics: Empirically-Derived Voltage- and Light-Sensitive Channelrhodopsin-2 Model. *PLoS Comput Biol* 2013; 9: 17–19.

[133] Jousset F, Maguy A, Rohr S, et al. Myofibroblasts electrotonically coupled to cardiomyocytes alter conduction: Insights at the cellular level from a detailed in silico tissue structure model. *Front Physiol* 2016; 7: 1–23.

[134] Ongstad E, Kohl P. Fibroblast–myocyte coupling in the heart: Potential relevance for therapeutic interventions. *J Mol Cell Cardiol* 2016; 91: 238–246.

[135] Severi S, Corsi C, Rocchetti M, et al. Mechanisms of b -Adrenergic Modulation of I Ks in the Guinea-Pig Ventricle : Insights from Experimental and Model-Based

Analysis. *Biophysj* 2009; 96: 3862–3872.

[136] Schindelin J, Arganda-carreras I, Frise E, et al. Fiji : an open-source platform for biological-image analysis. *Nat Methods* 2012; 9: 676–682.

[137] Matiukas A, Mitrea BG, Qin M, et al. Near-infrared voltage-sensitive fluorescent dyes optimized for optical mapping in blood-perfused myocardium. *Hear Rhythm* 2007; 4: 1441–1451.

[138] ThermoFisher Scientific. Fluoresence SpectraViewer, https://www.thermofisher.com/us/en/home/life-science/cell-analysis/labeling-chemistry/fluorescence-spectraviewer.html.

[139] Fluhler E, Burnham VG, Loew LM. Spectra, Membrane Binding, and Potentiometric Reponses of New Charge Shift Probes. *Biochemistry* 1985; 24: 5749–5755.

[140] Guo W, Kamiya K, Toyama J. Differential effects of chronic membrane depolarization on the K+ channel activities in cultured rat ventricular cells. *Cardiovasc Res* 1997; 33: 139–146.

[141] Kizana E, Cingolani E, Marbán E. Non-cell-autonomous effects of vector-expressed regulatory RNAs in mammalian heart cells. *Gene Ther* 2009; 16: 1163–1168.

[142] Feld Y, Melamed-frank M, Kehat I, et al. Electrophysiological Modulation of Cardiomyocytic Tissue by Transfected Fibroblasts Expressing Potassium Channels. *Circulation* 2002; 105: 522–529.

[143] Yankelson L, Feld Y, Bressler-Stramer T, et al. Cell therapy for modification of the myocardial electrophysiological substrate. *Circulation* 2008; 117: 720–31.

[144] Leibiger C, Kosyakova N, Mkrtchyan H, et al. First Molecular Cytogenetic High Resolution Characterization of the NIH 3T3 Cell Line by Murine Multicolor Banding. *J Histochem Cytochem* 2013; 61: 306–312.

[145] Quinn TA, Camelliti P, Rog-Zielinska EA, et al. Electrotonic coupling of excitable and nonexcitable cells in the heart revealed by optogenetics. *Proc Natl Acad Sci U S A* 2016; 113: 14852–14857.

[146] Wilm B, Muñoz-chapuli R. The Role of WT1 in Embryonic Development and Normal. In: *The Wilms' Tumor (WT1) Gene*. New York, NY: Humana Press, 2016, pp. 23–39.

[147] Jacquemet V, Henriquez CS. Loading effect of fibroblast-myocyte coupling on resting potential, impulse propagation, and repolarization: insights from a microstructure model. *AJP Hear Circ Physiol* 2008; 294: H2040–H2052.

[148] McDowell KS, Arevalo HJ, Maleckar MM, et al. Susceptibility to arrhythmia in the infarcted heart depends on myofibroblast density. *Biophys J* 2011; 101: 1307–1315.

[149] Sridhar S, Vandersickel N, Panfilov A V. Effect of myocyte-fibroblast coupling on the onset of pathological dynamics in a model of ventricular tissue. *Sci Rep* 2017; 7: 1–12.

[150] Majumder R, Engels MC, de Vries AAF, et al. Islands of spatially discordant APD alternans underlie arrhythmogenesis by promoting electrotonic dyssynchrony in models of fibrotic rat ventricular myocardium. *Sci Rep* 2016; 6: 24334.

[151] Kostecki G, Shi Y, Reich D, et al. Optogenetic Currents in Myofibroblasts Produce Acute Changes in Electrophysiology of Cocultured Cardiomyocytes. *Biophys J* 2019; 116: 31a.

[152] Pinto AR, Ilinykh A, Ivey MJ, et al. Revisiting cardiac cellular composition. *Circ Res* 2016; 118: 400–409.

[153] Kohl P, Kamkin A, Kiseleva I, et al. Mechanosensitive fibroblasts in the sino-atrial node region of rat heart: interaction with cardiomyocytes and possible role. *Exp Physiol* 1994; 79: 943–956.

[154] Kofron CM, Kim TY, King ME, et al. G_q -activated fibroblasts induce cardiomyocyte action potential prolongation and automaticity in a three-dimensional microtissue environment. *Am J Physiol Circ Physiol* 2017; 313: H810–H827.

[155] Doble BW, Kardami E. Basic fibroblast growth factor stimulates connexin-43 expression and intercellular communication of cardiac fibroblasts. *Mol Cell Biochem* 1995; 143: 81–87.

[156] Tan JL, Tien J, Pirone DM, et al. Cells lying on a bed of microneedles : An approach to isolate mechanical force. *Proc Natl Acad Sci* 2002; 100: 1484–89.

[157] Rohr S. Cardiac Fibroblasts in Cell Culture Systems - Myofibroblasts All Along? *J Cardiovasc Pharmacol* 2011; 57: 389–399.

[158] Dawson K, Wu CT, Qi XY, et al. Congestive Heart Failure Effects on Atrial Fibroblast Phenotype: Differences between Freshly-Isolated and Cultured Cells. *PLoS One*; 7. Epub ahead of print 2012. DOI: 10.1371/journal.pone.0052032.

[159] Serini G, Bochaton-Piallat ML, Ropraz P, et al. The fibronectin domain ED-A is crucial for myofibroblastic phenotype induction by transforming growth factor-β1. *J Cell Biol* 1998; 142: 873–881.

[160] Daniels A, Van Bilsen M, Goldschmeding R, et al. Connective tissue growth factor and cardiac fibrosis. *Acta Physiol* 2009; 195: 321–338.

[161] Lighthouse JK, Small EM. Transcriptional control of cardiac fibroblast plasticity. *J Mol Cell Cardiol* 2016; 91: 52–60.

[162] Tillmanns J, Hoffmann D, Habbaba Y, et al. Fibroblast activation protein alpha expression identifies activated fibroblasts after myocardial infarction. *J Mol Cell Cardiol* 2015; 87: 194–203.

[163] Kizana E, Ginn SL, Smyth CM, et al. Fibroblasts modulate cardiomyocyte excitability: Implications for cardiac gene therapy. *Gene Ther* 2006; 13: 1611–1615.

[164] Roell W, Klein AM, Breitbach M, et al. Overexpression of Cx43 in cells of the myocardial scar: Correction of post-infarct arrhythmias through heterotypic cell-cell coupling. *Sci Rep* 2018; 8: 1–14.

[165] Díaz-Araya G, Vivar R, Humeres C, et al. Cardiac fibroblasts as sentinel cells in cardiac tissue: Receptors, signaling pathways and cellular functions. *Pharmacol Res* 2015; 101: 30–40.

[166] D'Souza KM, Biwer LA, Madhavpeddi L, et al. Persistent Change in Cardiac Fibroblast Physiology Following Transient ACE Inhibition. *Am J Physiol - Hear Circ Physiol* 2015; ajpheart.00615.2015.

[167] Porter KE, Turner N a. Statins and myocardial remodelling: cell and molecular pathways. *Expert Rev Mol Med* 2011; 13: e22.

[168] Merrill DR, Bikson M, Jefferys JGR. Electrical stimulation of excitable tissue : design of efficacious and safe protocols. *J Neurosci Methods* 2005; 141: 171–198.

[169] Abilez OJ. Optogenetic LED array for perturbing cardiac electrophysiology. *Proc Annu Int Conf IEEE Eng Med Biol Soc EMBS* 2013; 1619–1622.

[170] Clements IP, Millard DC, Nicolini AM, et al. Optogenetic stimulation of multiwell MEA plates for neural and cardiac applications. *Proc SPIE* 2016; 9690: 96902C.

[171] Dwenger M, Kowalski WJ, Ye F, et al. Chronic optical pacing conditioning of h-iPSC engineered cardiac tissues. *J Tissue Eng* 2019; 10: 1–15.

[172] Ambrosi CM, Boyle PM, Chen K, et al. Optogenetics-enabled assessment of viral gene and cell therapy for restoration of cardiac excitability. *Sci Rep* 2015; 5: 17350.

[173] Pfeiffer ER, Tangney JR. Biomechanics of Cardiac Electromechanical Coupling and Mechanoelectric Feedback. *J Biomech Eng* 2014; 136: 1–11.

[174] Hirt MN, Sörensen N a, Bartholdt LM, et al. Increased afterload induces pathological cardiac hypertrophy: a new in vitro model. *Basic Res Cardiol* 2012; 107: 307.

[175] Godier-Furnémont AFG, Tiburcy M, Wagner E, et al. Physiologic force-frequency response in engineered heart muscle by electromechanical stimulation. *Biomaterials* 2015; 60: 82–91.

[176] Aiba T, Hesketh GG, Barth AS, et al. Electrophysiological consequences of dyssynchronous heart failure and its restoration by resynchronization therapy. *Circulation* 2009; 119: 1220–1230.

[177] Feng Z, Matsumoto T, Nomura Y, et al. TECHNOLOGICAL DEVELOPMENTS IN

JAPAN. *IEEE Eng Med Biol Mag* 2005; 24: 73–79.

[178] Pavesi A, Adriani G, Rasponi M, et al. Controlled electromechanical cell stimulation on-a-chip. *Nat Publ Gr* 2015; 1–12.

[179] Lu L, Mende M, Yang X, et al. Design and validation of a bioreactor for simulating the cardiac niche: a system incorporating cyclic stretch, electrical stimulation, and constant perfusion. *Tissue Eng Part A* 2013; 19: 403–14.

[180] Visone R, Talò G, Occhetta P, et al. A microscale biomimetic platform for generation and electro-mechanical stimulation of 3D cardiac microtissues. *APL Bioeng*; 2. Epub ahead of print 2018. DOI: 10.1063/1.5037968.

[181] Morgan KY, Black LD. Mimicking isovolumic contraction with combined electromechanical stimulation improves the development of engineered cardiac constructs. *Tissue Eng Part A* 2014; 20: 1654–67.

[182] Yamamoto K, Dang QN, Maeda Y, et al. Regulation of cardiomyocyte mechanotransduction by the cardiac cycle. *Circulation* 2001; 103: 1459–1464.

[183] Morgan KY, Black LD. Mimicking Isovolumic Contraction with Combined Electromechanical Stimulation Improves the Development of Engineered Cardiac Constructs. *Tissue Eng Part A* 2014; 20: 1654–1667.

[184] Chen MQ, Xie X, Wilson KD, et al. Current-Controlled Electrical Point-Source Stimulation of Embryonic Stem Cells. *Cell Mol Bioeng* 2009; 2: 625–635.

[185] Zaglia T, Pianca N, Borile G, et al. Optogenetic determination of the myocardial requirements for extrasystoles by cell type-specific targeting of ChannelRhodopsin-2. *Proc Natl Acad Sci* 2015; 112: E4495–E4504.

[186] Nussinovitch U, Gepstein L. Optogenetics for in vivo cardiac pacing and resynchronization therapies. *Nat Biotechnol* 2015; 33: 750–754.

[187] Kostecki G, Pandey S, Zhu R, et al. Engineering an Optogenetic System for Point-Pacing Cardiomyocytes in Culture. *Biophys J* 2019; 116: 99a.

[188] Hirt MN, Hansen A, Eschenhagen T. Cardiac tissue engineering: state of the art. *Circ Res* 2014; 114: 354–67.

[189] Eschenhagen T, Eder A, Vollert I, et al. Physiological aspects of cardiac tissue engineering. *Am J Physiol Heart Circ Physiol* 2012; 303: H133-43.

[190] Eitan Y, Sarig U, Dahan N, et al. Acellular cardiac extracellular matrix as a scaffold for tissue engineering: in vitro cell support, remodeling, and biocompatibility. *Tissue Eng Part C Methods* 2010; 16: 671–683.

[191] Oberwallner B, Brodarac A, Choi Y-H, et al. Preparation of cardiac extracellular matrix scaffolds by decellularization of human myocardium. *J Biomed Mater Res Part A* 2013; 102: 3263–3272.

[192] Plissiti ME, Louka E, Nikou C. Splitting of overlapping nuclei guided by robust combinations of concavity points. *Proc SPIE* 2014; 9034: 903431.

[193] Fitzgibbon A, Pilu M, Fisher RB. Direct least square fitting of ellipses. *IEEE Trans Pattern Anal Mach Intell* 1999; 21: 476–480.

[194] Bray M-AP, Adams WJ, Geisse N a, et al. Nuclear morphology and deformation in engineered cardiac myocytes and tissues. *Biomaterials* 2010; 31: 5143–50.

[195] Moreno JD, Zhu ZI, Yang P-C, et al. A computational model to predict the effects of class I anti-arrhythmic drugs on ventricular rhythms. *Sci Transl Med* 2011; 3: 98ra83.

[196] Eberly D. Distance from a Point to an Ellipse, an Ellipsoid, or a Hyperellipsoid, www.geometrictools.com/Documentation/DistancePointEllipseEllipsoid.pdf (2013).

[197] Bland JM, Altman DG. Transformations, means, and confidence intervals. *BMJ* 1996; 312: 1079.

[198] Wang B, Borazjani A, Tahai M, et al. Fabrication of cardiac patch with decellularized porcine myocardial scaffold and bone marrow mononuclear cells. *J Biomed Mater Res A* 2010; 94: 1100–10.

[199] Sarig U, Au-Yeung GCT, Wang Y, et al. Thick acellular heart extracellular matrix with inherent vasculature: a potential platform for myocardial tissue regeneration. *Tissue Eng Part A* 2012; 18: 2125–2137.

[200] Crapo PM, Gilbert TW, Badylak SF. An overview of tissue and whole organ decellularization processes. *Biomaterials* 2011; 32: 3233–43.

[201] Godier-Furnémont AFG, Martens TP, Koeckert MS, et al. Composite scaffold provides a cell delivery platform for cardiovascular repair. *Proc Natl Acad Sci U S A* 2011; 108: 7974–7979.

[202] Bowers SLK, Banerjee I, Baudino TA. The extracellular matrix: at the center of it all. *J Mol Cell Cardiol* 2010; 48: 474–82.

[203] Prestwich GD. Simplifying the extracellular matrix for 3-D cell culture and tissue engineering: a pragmatic approach. *J Cell Biochem* 2007; 101: 1370–83.

[204] Shi M, Zhu J, Wang R, et al. Latent TGF-β structure and activation. *Nature* 2011; 474: 343–349.

[205] McCain ML, Parker KK. Mechanotransduction: the role of mechanical stress, myocyte shape, and cytoskeletal architecture on cardiac function. *Pflugers Arch* 2011; 462: 89–104.

[206] LaNasa SM, Bryant SJ. Influence of ECM proteins and their analogs on cells cultured on 2-D hydrogels for cardiac muscle tissue engineering. *Acta Biomater* 2009; 5: 2929–38.

[207] Kim D-H, Lipke EA, Kim P, et al. Nanoscale cues regulate the structure and function of macroscopic cardiac tissue constructs. *Proc Natl Acad Sci U S A* 2010; 107: 565–70.

[208] Sekar RB, Kizana E, Smith RR, et al. Lentiviral vector-mediated expression of GFP or Kir2.1 alters the electrophysiology of neonatal rat ventricular myocytes without inducing cytotoxicity. *Am J Physiol Heart Circ Physiol* 2007; 293: H2757-70.

[209] Kuo P-L, Lee H, Bray M-A, et al. Myocyte shape regulates lateral registry of sarcomeres and contractility. *Am J Pathol* 2012; 181: 2030–7.

[210] Chung C-Y, Bien H, Entcheva E. The role of cardiac tissue alignment in modulating electrical function. *J Cardiovasc Electrophysiol* 2007; 18: 1323–9.

[211] Weiss JN, Karma A, Shiferaw Y, et al. From pulsus to pulseless: the saga of cardiac alternans. *Circ Res* 2006; 98: 1244–53.

[212] Spach MS, Heidlage JF, Barr RC, et al. Cell size and communication: role in structural and electrical development and remodeling of the heart. *Heart Rhythm* 2004; 1: 500–15.

[213] Spach MS, Dolber PC. Relating extracellular potentials and their derivatives to anisotropic propagation at a microscopic level in human cardiac muscle. Evidence for electrical uncoupling of side-to-side fiber connections with increasing age. *Circ Res* 1986; 58: 356–371.

[214] Bian W, Jackman CP, Bursac N. Controlling the structural and functional anisotropy of engineered cardiac tissues. *Biofabrication* 2014; 6: 024109.

[215] Bursac N, Parker KK, Iravanian S, et al. Cardiomyocyte cultures with controlled macroscopic anisotropy: a model for functional electrophysiological studies of cardiac muscle. *Circ Res* 2002; 91: e45–e54.

[216] Kleber A, Janse M, Fast V. Normal and abnormal conduction in the heart. In: *The Handbook of Physiology. The Cardiovascular System. The Heart.* 2002, pp. 455–530.

[217] Bursac N, Kirkton RD, McSpadden LC, et al. Characterizing functional stem cell-cardiomyocyte interactions. *Regen Med* 2010; 5: 87–105.

[218] Schouten VJA, ter Keurs HEDJ. The force-frequency relationship in rat myocardium. *Pflügers Arch* 1986; 407: 14–17.

[219] Lu HR, Rohrbacher J, Vlaminckx E, et al. Predicting drug-induced slowing of conduction and pro-arrhythmia: Identifying the ‘bad’ sodium current blockers. *Br J Pharmacol* 2010; 160: 60–76.

[220] Anderson KP, Walker R, Lux RL, et al. Conduction velocity depression and drug-induced ventricular tachyarrhythmias. Effects of lidocaine in the intact canine heart. *Circulation* 1990; 81: 1024–1038.

[221] Tung L, Zhang Y. Optical imaging of arrhythmias in tissue culture. *J Electrocardiol* 2006; 39: S2-6.

[222] Jongsma HJ, Wilders R. Gap junctions in cardiovascular disease. *Circ Res* 2000;

86: 1193–1197.

[223] Feng CH, Cheng YC, Chao PHG. The influence and interactions of substrate thickness, organization and dimensionality on cell morphology and migration. *Acta Biomater* 2013; 9: 5502–5510.

[224] Leong WS, Tay CY, Yu H, et al. Thickness sensing of hMSCs on collagen gel directs stem cell fate. *Biochem Biophys Res Commun* 2010; 401: 287–292.

[225] Herpel E, Singer S, Flechtenmacher C, et al. Extracellular matrix proteins and matrix metalloproteinases differ between various right and left ventricular sites in end-stage cardiomyopathies. *Virchows Arch* 2005; 446: 369–78.

[226] Sullivan KE, Quinn KP, Tang KM, et al. Extracellular matrix remodeling following myocardial infarction influences the therapeutic potential of mesenchymal stem cells. *Stem Cell Res Ther*; 5.

[227] Matsuura K, Masuda S, Shimizu T. Cell sheet-based cardiac tissue engineering. *Anat Rec (Hoboken)* 2014; 297: 65–72.

[228] Meyer T, Stuerz K, Guenther E, et al. Cardiac slices as a predictive tool for arrhythmogenic potential of drugs and chemicals. *Expert Opin Drug Metab Toxicol* 2010; 6: 1461–75.

[229] Blazeski A, Kostecki GM, Tung L. Engineered heart slices for electrophysiological and contractile studies. *Biomaterials* 2015; 55: 119–128.

Vita

Geran Kostecki was born July 16th, 1988 to Stanley and Jana in Saint Louis, Missouri. He graduated from Saint Louis University High School, followed by Washington University in St. Louis with a Bachelor of Science in Biomedical Engineering, where he worked under Dr. Vadim Fedorov, PhD in the lab of Dr. Igor Eimov, PhD, studying cardiac electrophysiology and writing software used to analyze optical voltage mapping data. In 2010, he enrolled in the Johns Hopkins University Biomedical Engineering PhD program, rotating in the labs of Dr. Natalia Trayanova, PhD, and Gordon Tomaselli, MD, before working in the lab of Dr. Leslie Tung, PhD. Supported by a predoctoral fellowship from the American Heart Association, Geran's research has contributed to eight peer-reviewed publications.